Integration and commissioning of LAPPDs in the ANNIE experiment
and
development and testing of SiPMs with active or passive light collectors

Dissertation

der Mathematisch-Naturwissenschaftlichen Fakultät
der Eberhard Karls Universität Tübingen
zur Erlangung des Grades eines
Doktors der Naturwissenschaften
(Dr. rer. nat.)

vorgelegt von
Marc Oliver Breisch
aus Nürtingen

Tübingen
2025

Gedruckt mit Genehmigung der Mathematisch-Naturwissenschaftlichen Fakultät der Eberhard Karls Universität Tübingen.

Tag der mündlichen Qualifikation:	29.09.2025
Dekan:	Prof. Dr. Thilo Stehle
1. Berichterstatter:	Prof. Dr. Tobias Lachenmaier
2. Berichterstatter:	Prof. Dr. Josef Jochum

Abstract

The Accelerator Neutrino Neutron Interaction Experiment (ANNIE) is a 26-ton gadolinium doped water Cherenkov detector situated on-axis of the Booster-Neutrino-Beam (BNB) at Fermilab. Its main goal is to measure the final state neutron multiplicity of neutrino-nucleus interactions to improve the systematic uncertainties of next-generation long baseline neutrino experiments. One of ANNIE's key features is the deployment of a new photosensor technology called Large Area Picosecond Photodetectors (LAPPD). These new state-of-the-art photosensors offer a picosecond time resolution as well as sub-centimetre spatial resolution.

In this work, the software environment, which includes data acquisition as well as slow control, for the LAPPDs was developed and tested - first in an on-site laboratory for characterisation measurements, a part of which has been analysed in this thesis, followed by the integration into the main ANNIE software environment and the successful deployment of three LAPPDs. It could be shown that all three LAPPDs were operating normally after deployment and events from neutrino interactions induced by the BNB could be identified. The successful operation of three LAPPDs simultaneously was achieved.

A second part of this thesis is the development and optimisation for Silicon Photomultipliers (SiPM). To improve the light collection of the sensors, they have been combined with either active or passive light collectors. A geometry for the light collectors was chosen based on Monte Carlo simulations, combining a conic bottom part to connect to the SiPM and a parabolic top part to increase internal total reflection. Calibration measurements resulted in a time resolution of the sensors between (152.7 ± 102.5) ps and (588.7 ± 28.86) ps. The determination of the characteristic parameters to describe the time profile of the light emission of different liquid samples, like water and scintillators, showed that the use of light collectors effectively increases the amount of detected photons in the region of interest for the light emission. It has also been shown that the addition of light collectors has almost no influence on the timing response of the sensor.

Zusammenfassung

Das Accelerator Neutrino Neutron Interaction Experiment (ANNIE) ist ein 26 t Gadolinium dotierter Wasser-Cherenkov-Detektor. Der Detektor befindet sich auf der Achse des Booster-Neutrino-Beam (BNB) am Fermilab. Sein Hauptziel ist die Messung der Neutronen-Multiplizität im Endzustand von Neutrino-Nukleus-Wechselwirkungen, um die systematischen Unsicherheiten zukünftiger Longbaseline-Neutrinoexperimente zu verringern. Eine der wichtigsten Eigenschaften von ANNIE ist der Einsatz einer neuen Photosensoren Technologie namens Large Area Picosecond Photodetector (LAPPD). Diese neuartigen Sensoren bieten eine Zeitauflösung im Pikosekundenbereich sowie eine Ortsauflösung im Subzentimeterbereich.

Im Rahmen dieser Arbeit wurde die Softwareumgebung für die LAPPDs entwickelt und getestet, welche sowohl die Datenerfassung (Data Acquisition) als auch die Steuerung (Slow Control) umfasst. Zunächst erfolgte dies in einem Labor vor Ort zur Durchführung von Charakterisierungsmessungen, wovon einige Messungen in dieser Arbeit analysiert wurden. Die Integration in die Hauptsoftwareumgebung von ANNIE und der erfolgreiche Einsatz von drei LAPPDs folgte. Es konnte gezeigt werden, dass nach dem Einbau alle drei LAPPDs funktionierten und Ereignisse aus Neutrino-Wechselwirkungen, induziert durch den BNB, identifiziert werden konnten. Der gleichzeitige erfolgreiche Betrieb von drei LAPPDs wurde somit erreicht.

Ein zweiter Bestandteil dieser Arbeit war die Entwicklung und Optimierung für Silizium-Photomultipliern (SiPM). Um die Lichtausbeute der Sensoren zu verbessern, wurden diese mit aktiven oder passiven Lichtkollektoren kombiniert. Monte Carlo Simulationen führten zu einer Geometrie für die Lichtkollektoren, bei der ein konischer unterer Teil zur Ankopplung an den SiPM mit einem parabolischen oberen Teil zur Erhöhung der internen Totalreflexion kombiniert wurde. Kalibriermessungen ergaben Zeitauflösung der Sensoren zwischen (152.7 ± 102.5) ps und (588.7 ± 28.86) ps. Die Bestimmung der charakteristischen Parameter zur Beschreibung des Zeitprofils der Lichtemission verschiedener Flüssigproben wie Wasser und Szintillatoren zeigte, dass der Einsatz von Lichtkollektoren die Anzahl detektierter Photonen in der „region of interest“ effektiv erhöht. Es konnte außerdem gezeigt werden, dass die Lichtkollektoren nahezu keinen Einfluss auf die Zeitauflösung des Sensors selbst haben.

Contents

1 | Motivation

"This is the start of something new. Time for a change."
- Dr Who, 9^{th} Doctor

Ever since the postulation of the neutrinos existence by Pauli in 1930 [1] the field of neutrino physics has grown into one of the largest fields in particle physics. From the first ever neutrino detection by Cowan and Reines [2] to the first ever detection of high energy astrophysical neutrinos by IceCube [3] the field has developed in numerous ways to improve the way neutrinos can be detected. Starting from the first experiment by Cowan and Reines in 1956 which used scintillation detectors, a combination of scintillators with photomultiplier tubes, to detect the neutrinos from a nuclear reactor, technologies to detect the signals produced by neutrino interactions have been an important aspect of neutrino physics. The development of these technologies includes the general development of photosensors and the strife to improve them be it in terms of detection efficiency or timing and spatial resolutions. But also different detection techniques are being advanced at the same time including the advancement of scintillators starting from basic solid-state scintillators, like crystals and plastics, to modern liquid scintillators made from multiple components.

The focus of this thesis is on the development, testing and deployment of photosensor technologies. First, the basic aspects of neutrinos, their sources and their high energy interactions will be introduced in chapter 2 followed by an introduction to photosensor technologies and scintillators in chapter 3. Chapter 4 will then introduce the Accelerator Neutrino Neutron Interaction Experiment (ANNIE), its design and its capability to house R&D technologies. One of these technologies are the state of the art Large Area Picosecond Photodetectors (LAPPD) which will be the focus of the first part of this thesis. Chapter 5 will introduce said photosensors as well as their way to deployment into the ANNIE detector. This includes the description of the full setup necessary as well as the characterisation measurements performed prior to deployment. The chapter will also introduce the software interfaces developed in the scope of this thesis and show their successful application and integration after the deployment of the first LAPPD. Lastly data from the time after deployment will be analysed to show that the LAPPD sees the interactions induced by the neutrino beam which will also be repeated for two additional LAPPDs that were deployed within the scope of this thesis.
Chapter 6 and 7 will focus on a newly developed detector design which will combine Silicon Photomultipliers (SiPM) with scintillators to increase the active photosensitive area and act as light collector. The sixth chapters will introduce said design, its components and a test bench setup as well as some characterisation measurements. The seventh chapter will show the results of test measurements with the goal of determining time profiles for different liquid samples like High-Purity-Low-Conductivity (HPLC) water, a liquid scintillator based on Linear Alkyl Benzene (LAB) and a newly developed, water based type named Water-based-Liquid-Scintillator (WbLS).

The thesis will then conclude with a summary of the results and an outlook for the future developments of this field. This includes the future of the LAPPD deployments but also a discussion on the viability of the newly developed detector design with ideas for future improvements.

2 Neutrino sources and interactions relevant to the ANNIE experiment

"The universe is big. It's vast and complicated and ridiculous. And sometimes, very rarely, impossible things just happen and we call them miracles."

- Dr Who, 11th Doctor

Neutrinos are part of the standard model of particle physics as electrically neutral fermions. Due to their non existing charge the only ways of interaction would either be gravitationally or via weak interaction. There are three flavours of neutrinos each corresponding to a charged lepton counterpart. As such there is an electron, a muon and a tau flavour. This chapter will introduce different neutrino sources as they are naturally produced in for example the sun or the earth's atmosphere but can also be produced artificially in accelerator complexes or as by-product of nuclear reactors. The accelerators in particular are relevant for this thesis as it is the primary source of neutrinos for the ANNIE experiment, explained further on. Lastly this chapter will neutrino interactions on a GeV scale as also relevant for the ANNIE experiment.

2.1 Natural and artificial neutrino sources

Neutrinos can be produced in several naturally occurring interactions as well as in man-made artificial sources. This chapter will introduce the most common sources for neutrinos as they are used for neutrino experiments. Figure 2.1 shows the expected and measured flux of (anti)neutrinos as a function of neutrino energy in a range between 10^{-6} eV up to 10^{18} eV. The plot shows the flux of most neutrino sources except accelerator neutrinos as they are dependent on the accelerator complex which allows the flux and energy range to be chosen within the limit upwards of MeV.

2.1.1 Natural sources

Cosmological neutrino background

At the low end of the neutrino energies, the flux is dominated by the cosmological neutrino background which ranges from μeV to several meV. It is a remnant of the neutrino freeze-out during the early universe and is assumed to be a uniform background with a temperature of 1.95 K [5], bearing similarities to the Cosmic Microwave Background (CMB). At this point it is still undetected.

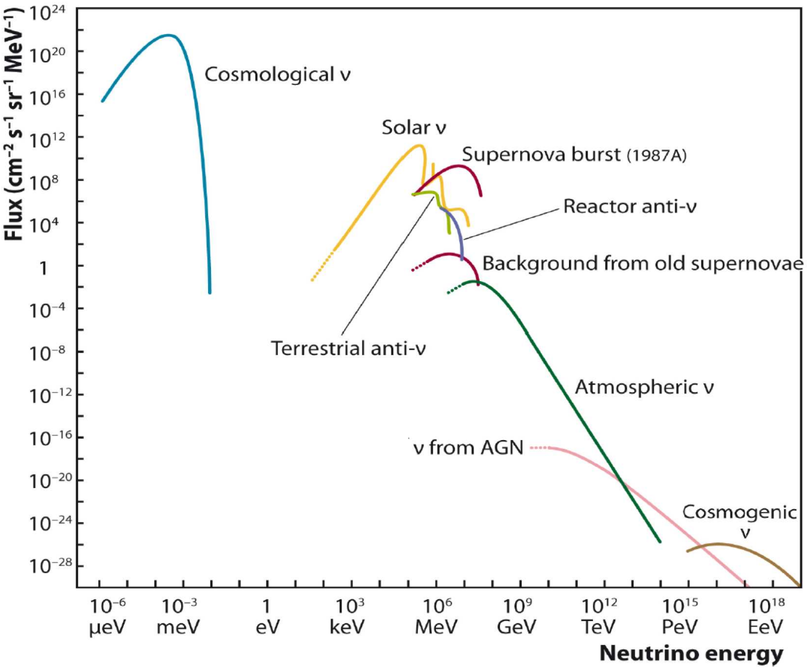

Figure 2.1: Predicted and measured (anti)neutrino flux as function of the neutrino energy. Both natural sources as well as artificial sources are shown in an energy range from a few keV up to EeV. In the low energy region the cosmological neutrino background is also shown [4].

Solar neutrinos

Solar neutrinos are produced during the proton fusion processes in stars. They are usually divided into different subspecies depending on the process of production, which would be the pp-chain, the pep-chain and the Beryllium-7 (^{7}Be) and Boron-8 (^{8}B) chains [6]:

$$p + p \rightarrow {}^2\mathrm{H} + \mathrm{e}^+ + \nu_e \quad , \tag{2.1}$$

$$p + e^- + p \rightarrow {}^2\mathrm{H} + \nu_e \quad , \tag{2.2}$$

$$^7\mathrm{Be} + e^- \rightarrow {}^7\mathrm{Li} + \nu_e \quad , \tag{2.3}$$

$$^8\mathrm{B} \rightarrow {}^8\mathrm{Be}^* + e^+ + \nu_e \quad , \tag{2.4}$$

as well as the CNO-chain [6]:

$$^{12}\mathrm{C} + p \rightarrow {}^{13}\mathrm{N} + \gamma, \tag{2.5}$$

$$^{13}\mathrm{N} \rightarrow {}^{13}\mathrm{C} + e^+ + \nu_e, \tag{2.6}$$

$$^{15}\mathrm{O} \rightarrow {}^{15}\mathrm{N} + e^+ + \nu_e, \tag{2.7}$$

$$^{17}\mathrm{F} \rightarrow {}^{17}\mathrm{O} + e^+ + \nu_e, \tag{2.8}$$

$$\tag{2.9}$$

The flavour of neutrinos produced in these reaction chains is purely electron neutrinos. Due to the large quantity of neutrinos produced in the centre of a star the sun is an excellent source of electron neutrinos. The neutrino energy varies strongly depending on the production process reaching up to several MeV.

Geo neutrinos

Geo neutrinos are neutrinos produced in the earth due to Potassium-40 (^{40}K), Thorium-232 (^{232}Th) and Uranium-238 (^{238}U) decays. Their maximum energy usually ranges around a few MeV and the produced neutrino flavour is electron antineutrino. Due to the detection threshold of 1.8 MeV for the Inverse Beta Decay (IBD) as detection reaction only the neutrinos produced in the Thorium and Uranium chains are be detectable by IBD [7].

Atmospheric Neutrinos

Atmospheric neutrinos are produced whenever cosmic rays interact with the earth's atmosphere and react to mesons like pions or kaons which then decay via [8]:

$$\pi^{\pm} \rightarrow \mu^{\pm} + \overset{(-)}{\nu}_{\mu}, \tag{2.10}$$

$$\mathrm{K}^{\pm} \rightarrow \mu^{\pm} + \overset{(-)}{\nu}_{\mu}. \tag{2.11}$$

The produced muons in turn decay into [8]:

$$\mu^{\pm} \rightarrow \mathrm{e}^{\pm} + \overset{(-)}{\nu}_{e} + \overset{(-)}{\nu}_{\mu}. \tag{2.12}$$

This results in an atmospheric neutrino flux combined of both electron and muon (anti)neutrinos with an energy of several MeV up to 100 TeV [9] depending on the energy of the cosmic rays starting the interactions. Although the atmospheric neutrino flux extends beyond 100 TeV, the flux for this energy range is dominated by the cosmogenic neutrino flux.

Supernova neutrinos

Supernova neutrinos are produced when massive stars at the end of their lifetime undergo a core-collapse. During the collapse about 99% of the gravitational binding energy is released in the form of neutrinos of all flavours in one large burst preceding the actual supernova matter burst [10]. A secondary aspect of supernova neutrinos is the so called Diffuse Supernova Neutrino Background (DSNB) which is assumed, yet undetected, to be a background of neutrinos originating from all supernova bursts throughout the age of the universe [11].

Cosmogenic neutrinos

At the far end of the neutrino energies the flux is dominated by cosmogenic neutrinos, which are produced as result of ultra-high energy protons interacting with photons from the CMB [12]. The neutrinos are thereby produced by either charged pion decay via

$$\pi^{\pm} \rightarrow \mu^{\pm} + \overset{(-)}{\nu}_{\mu} \tag{2.13}$$

followed by muon decays

$$\mu^{\pm} \rightarrow \mathrm{e}^{\pm} + \overset{(-)}{\nu}_{e} + \overset{(-)}{\nu}_{\mu}, \tag{2.14}$$

or beta decays of nuclei

$$p \rightarrow n + e^{+} + \nu_{e}, \tag{2.15}$$

$$n \rightarrow p + e^{-} + \bar{\nu}_{e}. \tag{2.16}$$

The cosmogenic neutrino flux is combined of both electron and muon (anti)neutrinos.
An additional cosmogenic source are the neutrinos of Active Galactic Nuclei (AGN), supermassive black holes at the centre of galaxies. Due to the large distance of AGNs the neutrino flux is low.

2.1.2 Artificial sources

Nuclear reactors

One of the most available and strongest artificial sources of neutrinos are nuclear reactors. During the fission process of the fuel isotopes, which are in most cases Uranium and Plutonium, neutron rich daughter isotopes decay via beta decays thus producing a flux of electron antineutrinos. The maximum energy ranges around a few MeV which makes the electron antineutrinos detectable via the IBD and a very good candidate for reactor neutrino experiments like for example Daya Bay [13] was.

Accelerators

Accelerator complexes designed for neutrino beams are a source of neutrinos that offer a vast array of advantages. The biggest advantage an accelerator beam has is the directional nature of the neutrino beam. Compared to the other neutrino sources the beam is directed to a small area in a defined direction. This makes it an ideal source for high flux measurements. A similar aspect is true for the energy range of the beam neutrinos. Due to the accelerator nature the energy is highly dependent on the production mechanism of the beam neutrinos and can thus be regulated as necessary. To produce the neutrino beam in general protons are accelerated to GeV energies which are then directed to a target. Collisions with the target will produce mesons like kaons and pions which in turn decay like

$$\mathrm{K}^{\pm}, \pi^{\pm} \rightarrow \mu^{\pm} + \overset{(-)}{\nu}_{\mu}, \tag{2.17}$$

with the muon decaying via

$$\mu^{\pm} \rightarrow \mathrm{e}^{\pm} + \overset{(-)}{\nu}_{e} + \overset{(-)}{\nu}_{\mu}. \tag{2.18}$$

By focusing the produced mesons in a magnetic field the orientation of the field allows for a selection between neutrinos or antineutrinos. This means that with accelerator complexes it is possible to to generate strong collimated neutrino beams with the additional benefit of selecting between neutrinos and antineutrinos.

2.2 High energy neutrino interactions

High energy neutrino interactions behave different to their low energy counterparts. In addition to quasi-elastic scattering that is dominant in the lower energy regions, neutrinos with energies upwards of a few hundred MeV can also interact via resonant interactions and deep inelastic scattering. Figure 2.2 shows the neutrino nucleon scattering cross section as a function of the neutrino energy. The cross section has three contributions of quasi-elastic scattering, resonant interactions and deep inelastic scattering. Below the plot, the energy ranges covered by different neutrino beam experiments are shown. All of the mentioned interaction types can occur in both charged current (CC) interactions as well as neutral current (NC) interactions but within the context of this thesis and since the leptons produced in CC interactions are the main driver for

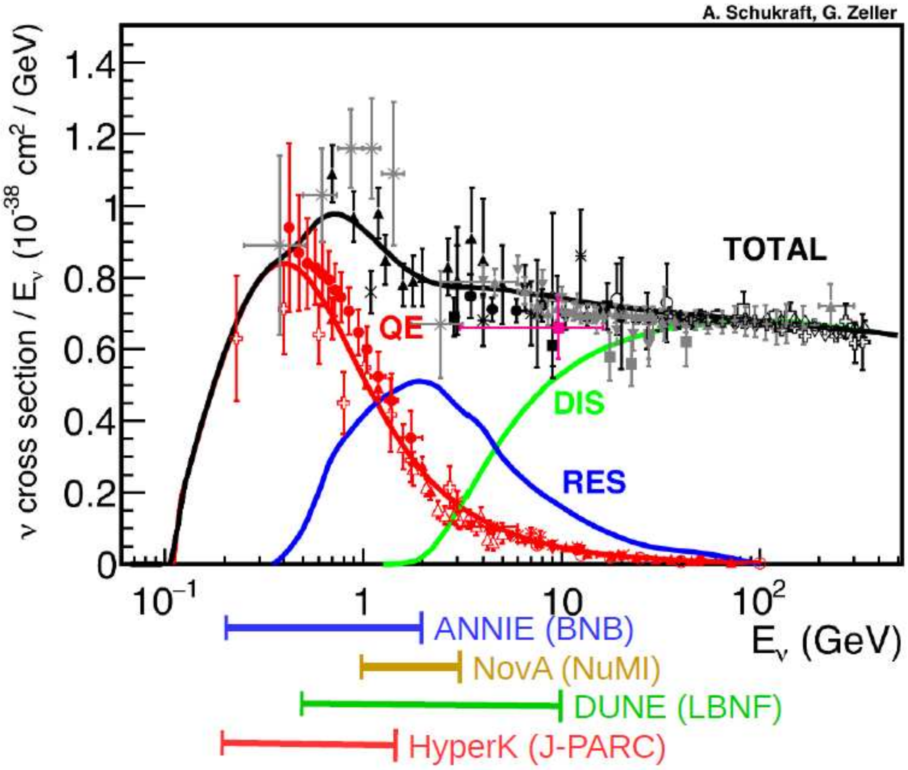

Figure 2.2: Neutrino nucleon scattering cross section as function of the neutrino energy. The total cross section is divided into quasi-elastic scattering (red), resonant interactions (blue) and deep inelastic scattering (green) [14]. Also shown are the expected neutrino energy ranges for different neutrino beam experiments: ANNIE (blue) [15], NOvA (yellow) [16], DUNE (green) [17], Hyper-K (red) [18].

the event classifications set by the ANNIE experiment the following explanations will focus on the CC interactions.

For the lower energies the main neutrino nucleus interaction channel is the charged current quasi elastic (CCQE) scattering where a neutron is converted into a proton by W-boson exchange and the emission of an accompanying charged lepton with

$$\nu_i + n \rightarrow p + l_i^- \quad . \tag{2.19}$$

For higher energies the interactions can also occur via charged current resonance (CC-RES) interactions where instead of a proton a baryon resonance particle is created. Usually a Δ^+ particle is produced which is unstable with a lifetime in the order of 10^{-24} s and decays into a $\pi^+(\pi^0)$ and a neutron (proton) [8]

$$\nu_i + n \rightarrow \Delta^+ + l_i^- \rightarrow \pi^+(\pi^0) + n(p) + l_i^- \quad . \tag{2.20}$$

Compared to the CCQE scattering the CC-RES interactions can produce a neutron-π^+ pair, changing the event topologies for experiments. For even higher energies the charged current deep inelastic scattering (CC-DIS) also become possible. Here a neutrino interacts with an individual nucleon quark to create hadronic cascades. All of these charged current interactions can be seen in figure 2.3 as Feynman diagrams.

All described neutrino nucleus interactions are called 1-particle 1-hole (1p-1h) interactions, as one nucleon is the interaction target, but it is also possible for 2-particle 2-hole (2p-2h) interactions to occur. In these cases the neutrino interaction happens on a correlated pair of nucleons which also changes the resulting particles for these interactions. This usually leads to issues in the reconstruction of events due to an underestimation of the energy.

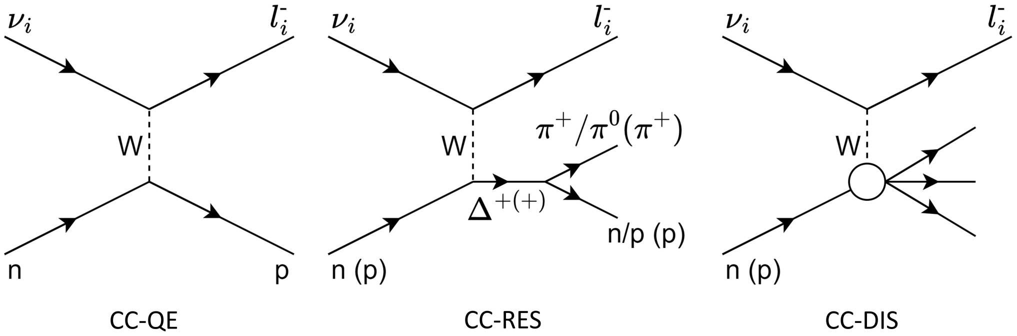

Figure 2.3: Feynman diagrams for charged current neutrino nucleon interactions via W exchange boson. The left hand side shows CCQE scattering where a neutrino interacts with a neutron to convert it into a proton and a charged lepton. The centre shows an example for a CC-RES interaction where instead of a proton a resonance $\Delta^{+(+)}$ particle is produced. This $\Delta^{+(+)}$ then decays into a $\pi^+/\pi^0(\pi^+)$ and a neutron/proton (proton). On the right hand side CC-DIS is shown where a neutrino directly interacts with a quark and produce a hadronic cascade. The circle represents an interaction inside the nucleon.

After the initial neutrino interaction the charged lepton produced will leave the nucleus while produced hadrons can further interact within the nucleus. These kind of interactions are called final state interaction (FSI). These interactions of a hadron with the nucleons can happen in different ways like elastic scattering, absorption or pion production. Due to these interactions produced particles can either be added onto the initial reaction results or be missing from them. As an example an additionally produced pion in a CCQE interaction will make the event topology look like a CC-RES interaction. The counter example to this would be a pion originating from a CC-RES interaction being absorbed and making the event topology look like a CCQE interaction. Figure 2.4 shows this in a simplified diagram. The left hand side shows the initial interaction type while the right hand side shows the event topology which is usually what an experiment will be able to detect. The resulting topologies are defined by their final state particles: For example, the charged lepton from the CC interactions with no additional pion is called CC-0π while the presence of an additional pion will be CC-1π. Final state nucleons which change the experimental event topology extend the nomenclature by the number of final state nucleons. Thus full event topologies are usually written as CC-Nπ-Mn with N being the number of additional pions and M the number of additional nucleons. In chapter 4.3 these interactions will be further described in the context of the ANNIE experiment.

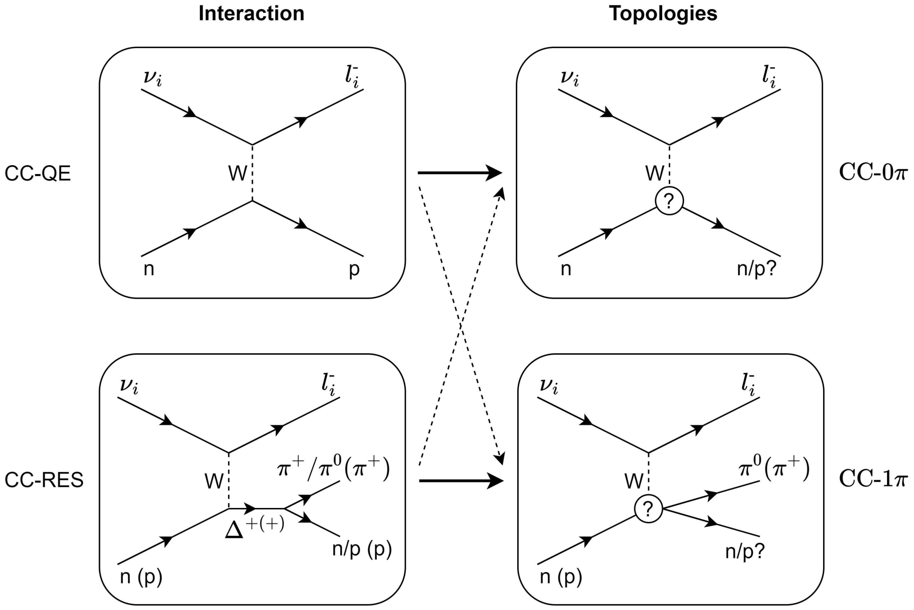

Figure 2.4: Simplified example for the difference between interaction type and event topology detectable by experiments. In this example the mix of CCQE and CC-RES interactions is shown. The solid arrows show the expected event topology while the dashed arrows show the mixed topologies. These mixed topologies can happen when for example a CCQE interaction also produces a pion in a FSI which makes it appear as a CC-RES interaction for experiments. Similarly, for the opposite direction where a pion produced in a CC-RES interaction is absorbed and the event topology looks like a CCQE interaction. Adapted from [19].

3 Introduction to scintillators and photosensor technologies

"Don't blink. Don't even blink. (...) Don't turn your back. Don't look away. And don't blink."
- Dr Who, 10th Doctor

This chapter will introduce and explain scintillators which act as detector media and photosensor technologies which will be further split into established detector technologies and technologies that have been a focus of development in recent years or are newly developed technologies. This chapter will first explain scintillators and their mechanisms as they are used in almost all neutrino experiments. Both liquid as well as solid organic scintillators will be explained and concrete examples will be shown as they are relevant for this thesis. Afterwards the relevant photosensor technologies for this thesis will be explained in detail.

3.1 Organic scintillators

Organic scintillators in general refer to all types of scintillators that are based on organic materials as basis which in most cases are benzene like structures. They are not detectors themselves but are used in combination with photosensors. The scintillator thereby usually takes on the role of detector medium in which the particle interactions take place. Through various mechanisms, that will be introduced in the following chapter, the interactions get transformed into light to which the photosensors are sensitive. More precisely energy deposited by charged particles excite an electron and the relaxation of the excited electron results in the emission of photons. The energy of the emitted photons is mostly dependent on the materials used in the scintillator composition. In some cases materials can also absorb photons of one wavelength and re-emit them with a higher wavelength due to internal transitions prior to re-emission. This will be explained in more detail at the end of this chapter where different examples of liquid and solid organic scintillators are introduced.

In a lot of cases the basis for organic scintillators, both liquid and solid, is a benzene ring which is a molecule consisting of six carbon atoms and six hydrogen atoms. To be in a stable state each carbon atom combines two p-orbitals and a s-orbital into three sp^2 orbitals, one of them at the C-H bond and two of them at the C-C bonds. These energy equivalent orbitals form what is called a σ-bond with the neighbouring carbon atoms. These bonds are what keeps the benzene ring stable. The more relevant part for the scintillation mechanism is the formation of π-bonds. These bonds are formed when the p-orbitals above and below the ring combine with their neighbouring orbitals. In these orbitals the electrons are de-localized and if a charged particle deposits energy these electrons will be excited as they are less strongly bound compared to the electrons in the σ-bonds.

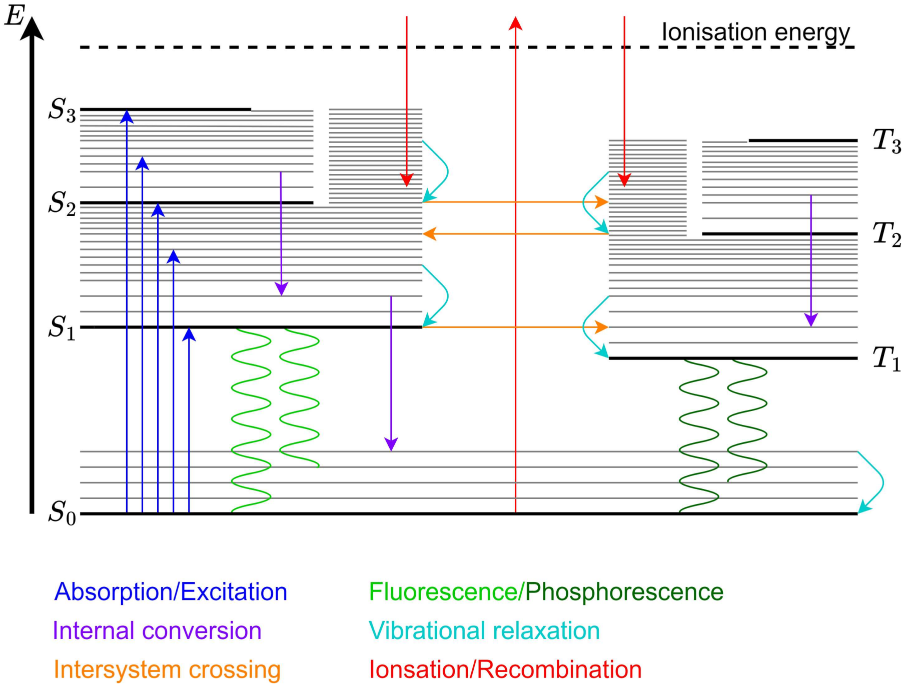

Figure 3.1: Jablonski diagram for the different singlet and triplet energy states of electrons. The black lines show the discrete electronic states (thick horizontal lines) and vibrational sub-states (thin horizontal lines) while the coloured arrows show the different types of transitions for excitation as upwards arrow and non-radiative de-excitations as downwards arrow. Radiative de-excitations are shown as waves and represent the emission of a photon. The colours for the transitions are labelled as indicated by the legend below the Jablonski diagram [20].

The relaxation processes that can occur after energy has been deposited can be seen in figure 3.1. It shows a Jablonski diagram which shows the different energy levels of the delocalized π-electrons within a benzene ring. The vertical axis indicates the energy of the different states above the ground state S_0 with the energy increasing upwards until the ionisation energy is reached. Discrete electronic states are S_i and T_i where S_i are singlet states, that have the same spin orientation as the ground state, and T_i are triplet states, which have an anti parallel spin compared to the ground state. Each of these discrete electronic states has multiple sub-states caused by molecular vibrations. This is represented by the thin vertical lines between the electronic states. If energy is now deposited by a charged particle the electrons within the molecule will be excited and elevated to a higher singlet state. The transition to a triplet state is forbidden due to the spin flip that would be required. This spin flip is forbidden under spin conservation rules and as such a population of triplet states from the ground state S_0 is not allowed [21]. Once excited the electrons can de-excite either radiatively or non-radiatively.

The ways to de-excite non-radiatively, i.e. without the emission of a photon, are internal conversion (IC), vibrational relaxation (VR) and inter-system crossing (ISC). In the case of IC an excited electron on a sub-state above an electronic state can transition to a lower electronic state or one of its sub-states without emitting a photon but rather due to the transfer of the energy to other molecules in the system via vibration and kinetic interactions. Compared to IC the transition caused via VR is a transfer of vibrational energy among the vibrational modes of the molecule itself and does not cause a transition between electronic states. ISC on the other hand is not a transition within a set of states but rather between them. It is the least likely of the three transitions to happen due to the forbidden nature of the spin flip but can still occur because of spin-orbit coupling [22]. It allows excited electrons to transfer between singlet and triplet states. All of these transitions can occur in both singlet and triplet states.

The radiative processes for the de-excitation of electrons are either fluorescence or phosphorescence for singlet de-excitation and triplet de-excitation respectively. These radiative transitions can mainly occur between the S_1/T_1 state and the ground state S_0 and is usually referred to as scintillation light. Electrons in higher excited states typically transitions non-radiatively to the S_1/T_1 state instead of transitioning directly to the ground state, due to their extremely short lifetimes around 10^{-13} s. Compared to these fast non-radiative processes, radiative transitions occur on much longer timescales. The transition from the S_1 state to the ground state S_0 is called fluorescence and is the faster of the two radiative processes, with a decay time of around 10^{-9} s to 10^{-8} s [23]. An important characteristic of these transitions is that the energy of the emitted photon is the same as the gap energy between the two states but always smaller than the energy difference of the original excitation, due to prior non-radiative processes. The spectrum of the emitted photons is not mono energetic as it would be expected from a fixed transition between S_1 and S_0 but rather a continuous spectrum. The reason for this is that the transition can go from the S_1 state to the ground state S_0 or one of its higher sub-states thus lowering the emitted energy of the photon.
Phosphorescence is the slower transitions and takes around 10^{-3} s to 10^{-1} s. The reason for the longer decay time is the forbidden nature of this transition as it requires a spin flip. The transition is still weakly allowed due to spin-orbit coupling but with a longer lifetime [23, 24]. One special process a triplet state can radiatively decay is via delayed florescence in which the excited electron gets additional energy from thermal excitations and then inter-system crosses to the singlet states from which it then decays like:

$$T_1 + \mathrm{E} \rightarrow S_1 \rightarrow S_0 + \gamma \quad . \tag{3.1}$$

To enhance the detection efficiency of scintillation light Wavelength Shifters (WLS) are often added to scintillators as an additional material in smaller concentrations. WLS function in the same way scintillators do with the notable difference being the mode of excitation as the source of the excitation is a photon emitted by the primary scintillator instead of charged particles. The photon is absorbed and excites an electron as described by the Jablonski diagram in figure 3.1. The energy of the absorbed photon needs to match the absorption spectrum of the WLS and has to be chosen as such. After re-emission of a photon the energy is lower than the energy of the absorbed photon which prevents it from being re-absorbed by the WLS. This is called Stokes shift. Depending on the experimental setup it may be necessary to chain multiple WLS together, where the emitted photon of one WLS is absorbed by a second WLS to further lower the energy. With this the wavelength of the emitted photons can be shifted from usually undetectable UV ranges towards the visible range where photosensors are most sensitive. An example of this is shown in figure 3.2 where a very common combination of WLS is shown. 2,5-Diphenyloxazole (PPO) and 1,4-Bis(2-methylstyryl)benzol (bis-MSB) were chosen and the emission spectrum of PPO matches the absorption spectrum of bis-MSB. Photons absorbed at $\sim 300\,\mathrm{nm}$ will be shifted to $\sim 420\,\mathrm{nm}$ which corresponds to the maximum detection efficiency of photosensors like the SiPM used in this thesis.

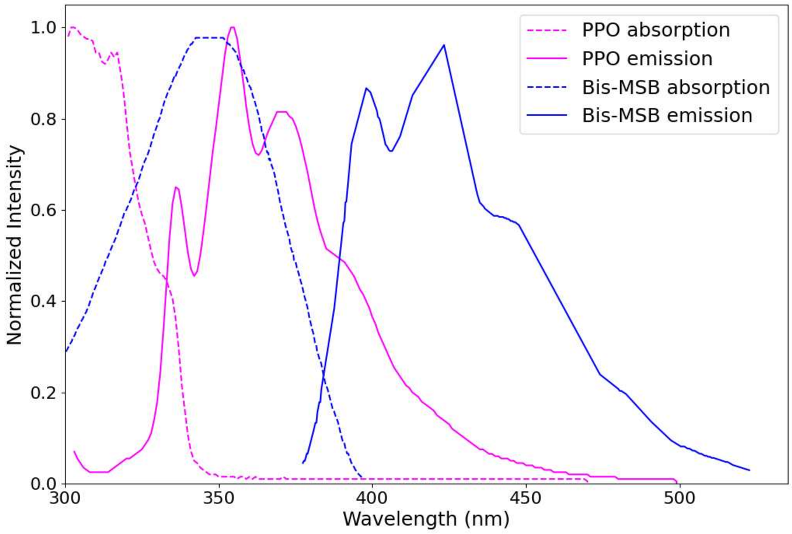

Figure 3.2: Absorption (dashed line) and emission (solid line) wavelength spectra of 2,5-Diphenyloxazole (PPO) in magenta and 1,4-Bis(2-methylstyryl)benzol (bis-MSB) in blue with their maximum normalized to 1 [25, 26].

The most common types of organic scintillators are plastics and liquids. Plastics usually are made from a base material like Polystyrol (PS) or Polymethylmethacrylat (PMMA) as they have an absorption range in the far UV to UV region [27, 28]. They are additionally doped with WLS materials like the above mentioned PPO and bis-MSB to move the originally low wavelength to a region, where photosensors are sensitive to, via successive absorption and re-emission by the WLS. It is not uncommon to use a combination of multiple WLS materials to achieve this similar to figure 3.2. For liquid scintillators the principle is the same as for the plastic scintillators where different types of WLS are added to a chosen solvent used as basis. A common choice for this is for example Linear Alkyl Benzene (LAB) in combination with PPO and bis-MSB. The principle of operation is the same for both liquid and solid scintillators whereas a base material absorbs the low wavelength photons and different combinations of WLS shift them to higher wavelengths to be in the sensitive range of photosensors.

A special case of liquid scintillator is the newly developed Water-based-Liquid-Scintillator which compared to previous liquid scintillators uses water as basis [30]. The use of water compared to other solvents as basis for scintillators has multiple advantages. For example the attenuation length of water ($\sim 100\,\mathrm{m}$ at $405\,\mathrm{nm}$ [31]) is a about three times larger than for example for LAB ($\sim 29.90\,\mathrm{m}$ at $430\,\mathrm{nm}$ [32]). This makes it easier to use in large scale experiments where the attenuation length of the medium is comparable to the size of the detector. An example for this is the Jiangmen Underground Neutrino Observatory (JUNO) where the attenuation length at $430\,\mathrm{nm}$ is $\sim 29.90\,\mathrm{m}$ with an inner detector diameter of $35.4\,\mathrm{m}$ [33]. Next to the high transparency of WbLS the production of Cherenkov radiation on a water basis is a significant advantage. As WbLS generally have a lower scintillation light yield the ratio between produced Cherenkov radiation and scintillation light improves, making it easier to separate the two production mechanisms. Since most organic scintillators or WLS are hydrophobic solving them in water is not trivial. This is done by building so called micelles, essentially small droplets, of hydrophobic organic material enclosed by surfactant molecules that are hydrophilic.

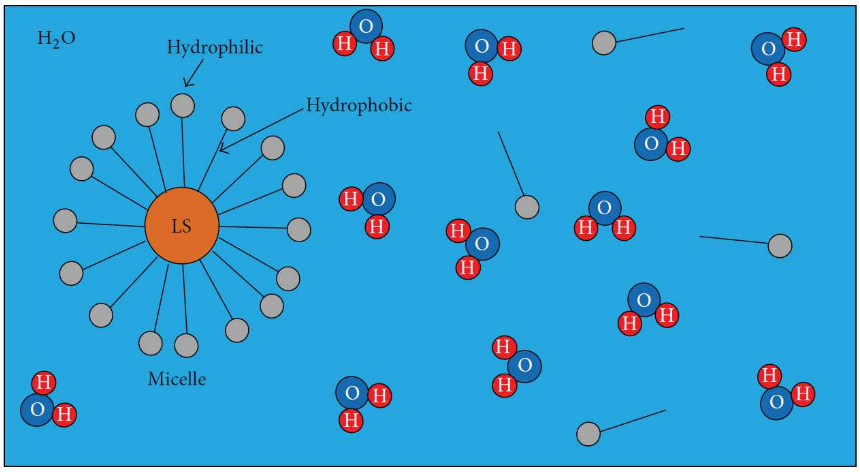

Figure 3.3: Water-based-Liquid-Scintillator micelle structure. Shown are the hydrophobic and hydrophilic parts of the micelles encompassing the liquid scintillator [29].

Figure 3.3 shows the basic principle behind the micelle structure [29, 30].
In this thesis multiple types of the described scintillators will be used. This will include an LAB based liquid scintillator with WLS and a WbLS, but also plastic scintillators made from PS and WLS.

3.2 Established photosensor technologies

This part of the chapter will focus on well established photosensor technologies which have been around for several tens of years and contributed significantly to either neutrino physics in general or paved the way for future technologies.

3.2.1 Photodiodes and avalanche photodiodes

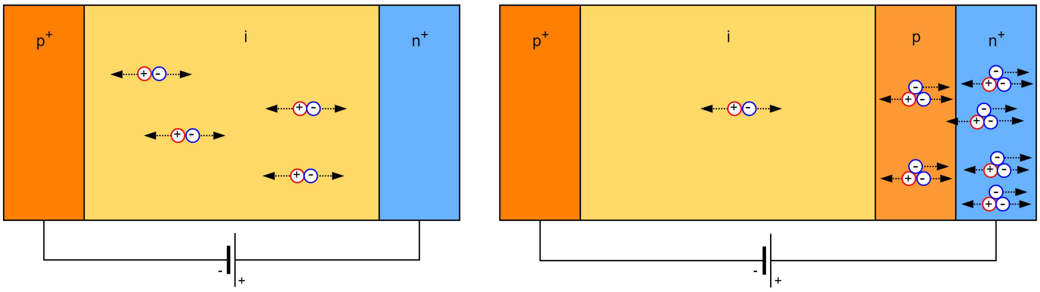

Figure 3.4: Schematic of a PIN-Photodiode on the left hand side and an avalanche photodiode on the right hand side. The conventional PD consists of a p-doped side (negative bias), an n-doped side (positive bias) and an intrinsic region in-between. The APD is set up in the same way normal photodiodes are, but with a less p-doped area between the intrinsic and the n-doped area. The generated electron-hole-pairs are represented by a red/blue circle with the corresponding charge [20].

A Photodiode (PD) in general is a semiconductor that is both p- and n-doped. The normal PDs have a PIN structure which is build of an intrinsic region that is sandwiched between a p-doped and an n-doped region with negative and positive voltages applied respectively. This can be seen on the left hand side in figure 3.4. If photons pass through the intrinsic region and deposit energy, electron-hole pairs will be created depending on the amount and energy of the photons. Due to the electric field created by the p-n junction in a photodiode, charge carriers are separated and move towards the oppositely charged sides. If enough charge carriers are created a current is generated and can be detected as signal. The downside of this is that a normal PD has no internal gain and a signal can only be detected if a significant amount of photons deposit energy in the material.
To account for this an extended version of normal PDs exists called Avalanche Photodiode (APD). The main difference to a normal PD is an additional lower p-doped region between the intrinsic area and the n-doped area. This can be seen on the right hand side of figure 3.4. Additionally, a higher voltage is applied at the respective sides, usually around a few hundred volts. The charge production mechanism is the same as for PDs where a photon with high enough energy deposits it in the intrinsic area and an electron-hole pair is created. Due to the higher voltage applied the kinetic energy gained by the charge carriers can exceed the threshold necessary to create additional charge carriers through collisions with bound electrons. This continues throughout the entire path the electron travels, colliding with more and more bound electrons releasing them and creating an avalanche effect allowing the detection of a smaller amount of photons. This internal gain of an APD is usually around a few hundreds and a significant amount of photons is still necessary, albeit less than for a normal PD, to detect a signal.

3.2.2 Photomultiplier tubes

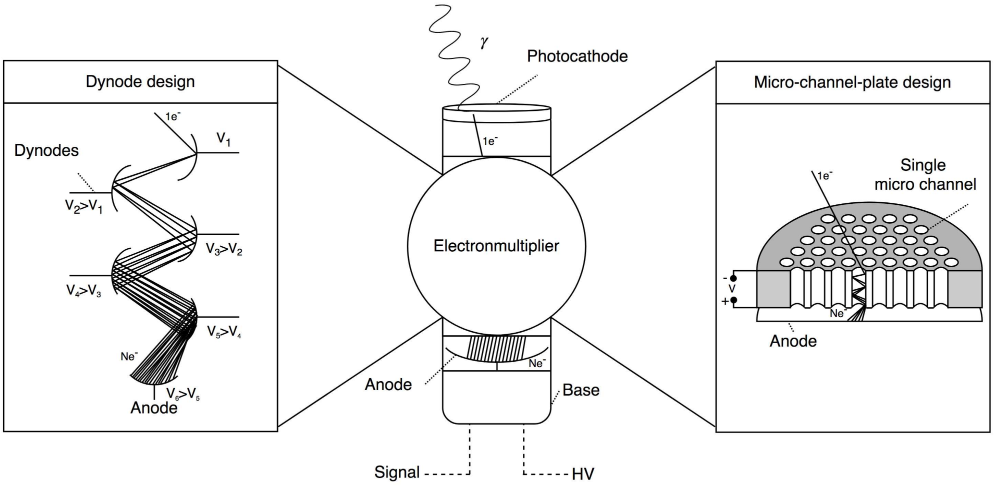

Figure 3.5: Schematic depiction of a PMT and its working principle. The centre shows the general setup with a photocathode on top and an anode on the bottom. In between is a electron-multiplier that can either be dynode based (left hand side) or MCP based (right hand side). At the bottom, the anode collects the accumulated charge. The PMT is supplied and read out through a base that allows for HV and signal connections. [20]

Photomultiplier tubes (PMT) are one of the oldest photosensors to exist with them being almost 100 years old. They are some of the most used detectors in neutrino physics being used in almost all experiments. The basic principle of a PMT is the conversion of a photon into an electron using the photo-electric effect. To generate a measurable signal the produced primary electron needs to be multiplied to generate a charge cascade. Thus the general design of a PMT always consists of a photocathode to convert an incoming photon into an electron, an electron-multiplier which can have different designs but in the end generates a cascade of electrons and an anode which collects the produced electrons. This structure can be seen in figure 3.5 in the centre. The collected charge is measured as a voltage, which results from the current flowing from the anode. This entire setup is enclosed in an evacuated glass housing to reduce conductivity and prevent discharges.

There are two main types of PMTs, the dynode style PMT and the Micro-Channel-Plate (MCP) based PMT. While the overall design is the same in both cases the main difference between these two types is the way the electrons are multiplied.
The classic PMT has a dynode structure to generate the electron cascade, which can be seen in figure 3.5 on the left hand side. The primary electron is accelerated in an electric field generated by the dynodes. Once the primary electron hits the first dynode, secondary electrons are released due to collisions of the first electron with the dynode. To accelerate electrons to the next dynodes, a consecutively higher voltage is applied to the dynodes. The principle is repeated for each dynode until the avalanche reaches the anode, where it is measured as a voltage pulse.
The MCP-based PMTs are a newer version of the classical PMT that replaces the dynodes with a micro-channel-plate. These plates usually are a few millimetres thick and feature a large number of micrometer wide holes which in most cases are angled to prevent electrons from moving straight through. This can be seen in figure 3.5 on the right hand side for an example with straight holes. The working principle is similar to dynode PMTs. By applying a voltage at the top and a higher voltage at the bottom of the MCP the thus created electric field first accelerates the primary electron until it hits one of the holes. Inside, electrons then continue the acceleration due to the electric field and scatter on the walls and produce additional electrons which are then collected as a cascade at an anode behind the MCP.

This multiplication of electrons is a parameter called gain and is one of the most important characteristics for a PMT. Since the multiplication is dependent on the acceleration of the electrons the gain is a voltage dependent parameter and it is defined as the ratio of the initial charge Q_i and the collected charge Q_c:

$$G = \frac{Q_c}{Q_i} \tag{3.2}$$

As voltage dependant parameter the gain usually has to be weighted against the Dark-Count-Rate (DCR) of a photosensor which refers to the rate at which the sensor generates signals in the absence of any incident light. These signals can arise from photo-electron emission due to various factors such as thermal fluctuations and electronic noise within the sensor itself.
Although the process of multiplication is in general the same, the two types of PMT offer different advantages and disadvantages. The main difference being an effect on the timing characteristics. Due to the size and structure of MCP-based PMTs, especially larger ones, the chance of the primary electron missing the MCP is non-negligible and has to be either accepted as loss or the electrons have to be looped around with an additional electric field. This in turn creates a large effect on the timing resolution of the PMT which is usually defined as the transit-time-spread (TTS).

The TTS is a parameter that is defined as the variation in the time it takes an electron generated by an incident photon to transit through the photosensor and produce an output signal [34]. Depending on the detector type the variations have different origins. For evacuated detectors with electron multipliers the reasons are for example:

- Different initial velocities and emission angles of the photo-electron.
- Different transit times from different points on the photocathode.
- A time spread in the electron multiplier.

As such the design of the electron multiplier has a large influence on the timing of the detector. This effect also affects the rise/fall time of the electric signal. The rise and fall time are parameters that describe the time profile of the current produced by a single photon. The rise time is defined as the time it takes the voltage to rise from 10% to 90% of its amplitude while the fall time is the time it takes to fall from 90% of the amplitude to 10% [34]:

$$RT = t\,(90\%) - t\,(10\%) \quad , \tag{3.3}$$

$$FT = t\,(10\%) - t\,(90\%) \quad . \tag{3.4}$$

The last important parameters to introduce for PMTs are the quantum efficiency (QE) and the photo detection efficiency (PDE). The QE is the efficiency with which a photosensor converts incident photons into electrical signals. It differs for solid-state detectors, where it is the production chance of electron hole pairs in the material itself, and evacuated detectors which use a photocathode, where the it is the efficiency to release a electron from the cathode into the detector inside. It is described by

$$QE\,(\lambda,\vec{x},\alpha) = \frac{N_{pe}}{N_{ph}} \tag{3.5}$$

where $\vec{x}$ is the position, α the incident angle on the photocathode, λ the wavelength of the incident photon, N_{pe} is the amount of released photo-electrons and N_{ph} the amount of incident photons. The collection efficiency (CE) describes the ratio of the number of released photo-electrons N_{pe} at the photocathode and the number of electrons produced after the charge avalanches N_{det}:

$$CE\,(\vec{x},\alpha) = \frac{N_{det}}{N_{pe}} \tag{3.6}$$

where $\vec{x}$ is the initial position and α the incident angle of the primary photo-electron on the photocathode. As such the CE is a combination of geometrical properties and the properties of the focusing electrodes. Lastly the PDE is the combination of the both former effects [34]:

$$PDE\,(\lambda,\vec{x},\alpha) = QE\,(\lambda,\vec{x},\alpha) \cdot CE\,(\vec{x},\alpha) \quad . \tag{3.7}$$

Since the QE is a wavelength dependent characteristic the PDE is also wavelength dependent.

3.3 New photosensor technologies

This chapter will introduce newer detector technologies, namely SiPM and LAPPDs. It is important to note that newer in this case is not necessarily a reference to the actual age of a technology but sometimes rather a meter for the presence of certain technologies in actual neutrino experiments as some have been around for a long time but have not been standardized for experiments.

3.3.1 Silicon photomultiplier

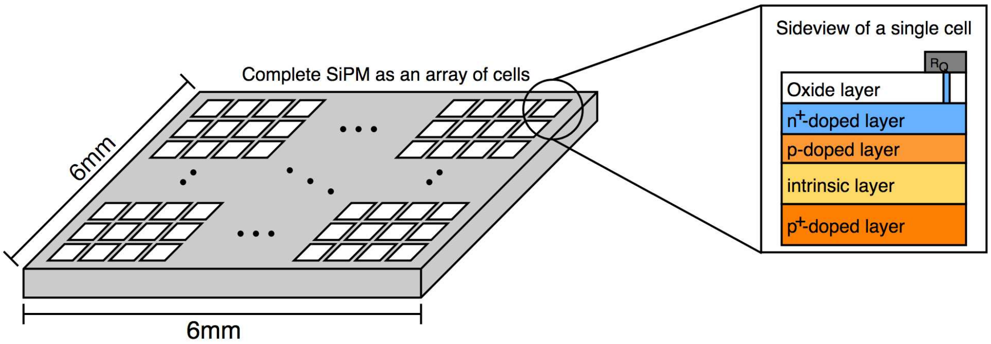

Figure 3.6: Schematic setup of a single 6x6 mm SiPM made from an array of APDs and quenching resistors. The left hand side shows the full array of cells in a square pattern. Each cell thereby consists of an APD and a quenching resistor R_Q which is shown on the right hand side for a single cell [20].

Silicon Photomultiplier are an applied technology based on avalanche photodiodes. They are built by creating micrometer sized APDs and placing them in an array as seen in figure 3.6. The difference in this case is that compared to normal APDs they are outfitted with an additional resistor called quenching resistor R_Q. With each cell being such a modified APD the mechanism for creating electric charges from photons is the same as described in chapter 3.2.1. The difference to APDs is that SiPM are operated in Geiger mode which means that they are operated at a bias voltage above their breakdown voltage. Being in this regime a single photon is enough to create a significantly large avalanche to be detected as a signal. The issue with this in normal operation would be an endless avalanche occurring once triggered. To prevent this and be responsive very quickly after an avalanche is triggered, quenching resistors were added to each cell. As the produced photocurrent increases, the quenching resistor which is in series with the APD of the cell, will lower the bias voltage applied to the diode weakening the electric field until the bias voltage is below the breakdown voltage thus stopping the avalanche. The other cells that are not affected by the avalanche will remain fully charged and ready to detect photons. This results in the characteristic signal of a SiPM which has a very short rise time (around a few hundred picoseconds) and a fairly long fall time (around a hundred nanoseconds) since the bias voltage needs time to recover. Important to note is that the recovery time for the cells is largely dependent on their size and as such a larger cell size results in a longer recovery time [35]. The overall bias voltage of a SiPM is a combination of the breakdown and an over-voltage which defines the gain of the sensor:

$$U_{\text{Bias}} = U_{\text{Breakdown}} + U_{\text{Over}} \quad . \tag{3.8}$$

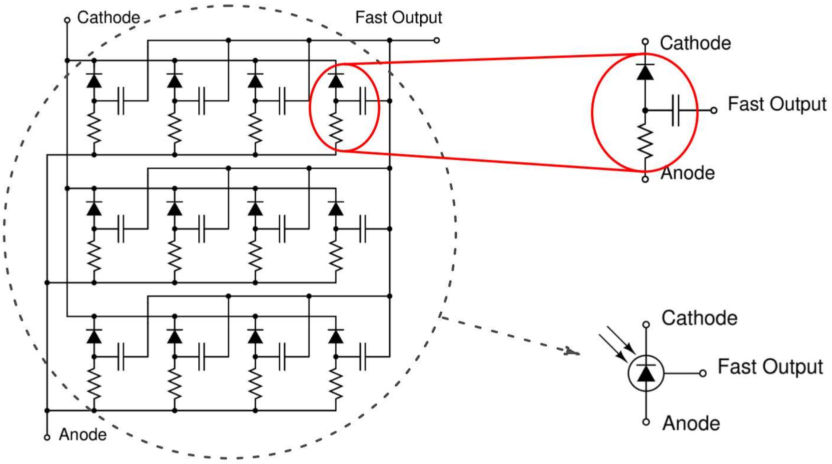

Figure 3.7: Simplified circuit schematic of a SiPM from the manufacturer OnSemi. Shown is the array cell structure as well as the implementation of a fast output [35].

In general SiPM have mostly the same set of parameters as PMTs (see chapter 3.2.2) and can as such be characterised in the same way. A difference for solid-state detectors is the QE, CE and PDE. The QE for solid state detectors describes the probability to generate electron-hole pairs in the material which is a wavelength dependent material property. The CE is a combination of geometrical properties and the Geiger efficiency which describes the probability that an electron-hole pair causes an avalanche. In turn the PDE is a combination of the QE and CE similar to the PDE of PMTs [35].

In the scope of this thesis one extra type of SiPM has to be explained. It is a special sensor developed by OnSemi [36] which adds an additional capacitively coupled output, called fast output, to each cell of a SiPM. Figure 3.7 shows a circuit diagram of this type of SiPM and circled in red is a single APD cell with the additional fast output. The fast output is the derivative of the internal fast switching of the cells and it is, similar to the cathode-anode output, the sum of all cells. An advantage of the fast output is a shorter pulse width compared to the characteristic SiPM pulse for which the shape is dominated by the long recharge tail [35]. Chapter 6.4.1 will go into further detail on this type of output and its timing characteristics.

3.3.2 Large Area Picosecond Photodetectors

The Large Area Picosecond Photodetectors are new, state of the art photosensors. With its novel design and impressive parameters the LAPPDs offers some of the currently best parameters available for photosensors of which some are listed in table 3.1.

In general an LAPPD is a MCP based detector which is fairly similar to the design of other MCP based detectors like the PMTs described in 3.2.2. The schematic is shown in figure 3.8 and from top to bottom an LAPPD consists of a semitransparent bi-alkali photocathode, which gives a uniform QE of $> 20\%$. Next is a chevron-pair of MCPs which means that they have the same design as described in figure 3.5 but the channels are oriented at an angle instead of going straight through. Between the two plates the angle of the channels is counter oriented. Firstly, this prevents the electrons produced by the photocathode going straight to the anodes and secondly it limits the spread of the electron avalanche to keep the spatial resolution in the

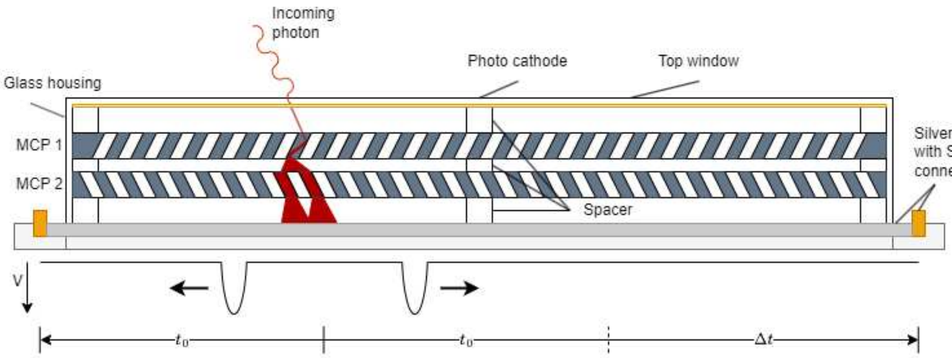

Figure 3.8: Schematic drawing of an LAPPD as well as an exemplary waveform. From top to bottom it consists of a bi-alkali photocathode, two layers of MCPs with counter oriented channels and 28 silver strip anodes which can be read out at both ends. The exemplary waveform shows the principle of determining the position along an anode strip. The time a signal needs to reach each end of the strip is t_0 on one end and $t_0 + \Delta t$ on the other.

Table 3.1: Exemplary list of LAPPD parameters [37].

Parameter	Value
Active surface [cm^2]	400
Gain	10^7
QE [%]	~ 25
DC rate [$\mathrm{kHz/cm}^2$]	4.2
Spatial resolution [mm]	~ 1
Time resolution [ps]	< 100

sub-centimetre regime. The bottom of the detector is made up of 28 silver anode strips which span the entire length of the LAPPD and have a width of 5.2 mm with a gap of 1.7 mm [38]. These strip lines are the reason for the very good spatial resolution as events can be more precisely reconstructed.

To reconstruct the position of events to this level of precision is one aim of LAPPD analysis. The way to get the position is different depending on if the position is reconstructed along or across strip lines. The first position that has to be reconstructed is along the strip lines as this allows for the application of cuts on the reconstruction across strip lines. The position along a strip line is extracted from the timing information gained by reading a strip line at both ends. Due to the potential difference in path lengths the signal has to travel, the position is determined by this difference in arrival time Δt. But this also means that the precision of this reconstruction is highly dependent on the method of digitization and the sampling rate of the digitizer. To get the position of the event along a strip line the following relation [39] is used

$$\Delta t = t_r - t_l \quad , \tag{3.9}$$

$$d_l = \frac{L}{2} - \frac{\Delta t v}{2} \quad , \tag{3.10}$$

$$d_r = L - d_l \quad , \tag{3.11}$$

where L is the total length of a strip line and v is the signal propagation speed in the silver strip lines which is around $0.6c$ and c is the speed of light in vacuum. d_l/d_r are the distances from the signal start position to the left or right side of the strip respectively and t_l/t_r are the signal propagation times. With this relation the position of the signal origin can be reconstructed along a strip line. This can also be seen in figure 3.8 at the bottom as an exemplary waveform. In general the strip with the highest amount of collected charge is used for this. Next the neighbouring strip lines are checked if they contain signals as well. Since the position on the initial strip line is already known, signals from neighbouring strip lines can be cut if the event position differs to much.

The position across strip lines can then be calculated from the centre of charge given by the amplitudes of the collected charges on the strip lines. To calculate the exact position of an event the reconstruction has to take across and along strip line reconstruction into account and calculate the event vertex weighted from all valid strip line reconstructions.

4 The Accelerator Neutrino Neutron Interaction Experiment

> *"Water is patient, Adelaide. Water just waits. Wears down the cliff tops, the mountains. The whole of the world. Water always wins."*
>
> - Dr Who, 10th Doctor

As chapter 2.2 introduced, high energy neutrino interactions, in both the CC as well as NC channel, play a role in understanding backgrounds due to final state neutrons/protons created in these interactions. Experiments like MicroBoone [40], for final state protons [41], or Super-Kamiokande [42], for final state neutrons [43] did already put some work into understanding the resulting backgrounds. For the latter it is as part of a later physics goal and not the primary one. The Accelerator Neutrino Neutron Interaction Experiment (ANNIE) was designed to, as primary physics goal, better understand the CC interactions of ν_μ and water and as such the following chapters will focus only on CC interactions. ANNIE is a Water-Cerenkov detector build at Fermi National Accelerator Laboratory (Fermilab) about 100 m downstream of the Booster-Neutrino-Beam (BNB). The aim is to measure the final-state neutron multiplicity induced by muon neutrino interactions as well as the muon neutrino cross-section in water with the goal to better understand the neutrino interactions [15]. Due to the close distance to the neutrino beam source ANNIE can acquire around 26000 CC muon neutrino events per year and ton of water [44] which corresponds to $2 \cdot 10^{20}$ proton-on-target (POT) from the BNB. The following chapters will first introduce the BNB, followed by the ANNIE detector design and its components. Last will be a brief explanation of the high energy neutrino physics in ANNIE and the interaction mechanisms in the water tank as well as the introduction of the data acquisition and analysis software framework used as it is an important part of this thesis.

4.1 The Booster Neutrino Beam

The Booster-Neutrino-Beam is part of the Fermilab accelerator complex shown in figure 4.1. It consist of a linear accelerator which accelerates protons to 400 MeV which then are injected into the Booster ring which further accelerates the protons to a peak energy of 8 GeV [46]. The protons are then guided to the Booster-Target-Hall where they hit a beryllium target mounted in a magnetic focusing horn. Once the protons hit the beryllium target they produce mesons, primarily kaons and pions, via:

$$p + {}^{9}\mathrm{Be} \rightarrow K^{\pm} \ \text{or} \ \pi^{\pm} + X \quad . \tag{4.1}$$

After the production of the mesons the magnetic focusing horn separates the mesons depending on their charge. The mesons with the unwanted charge is directed into the ground while the

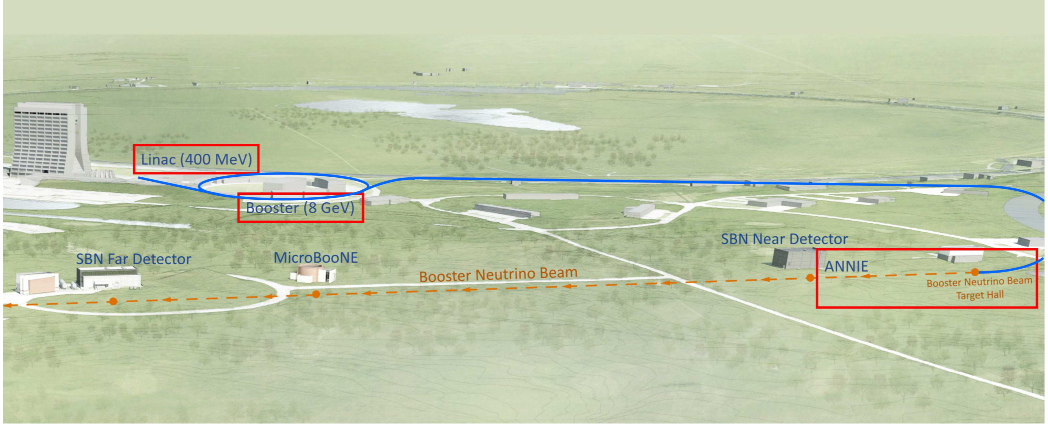

Figure 4.1: Schematic overview of the Fermilab accelerator complex. Shown are all components included in the different parts of the neutrino beam generations as well as the no longer in use Tevatron in the background. The important parts for the BNB, the Linac, the Booster ring and the actual BNB are marked in red. The proton path is shown in blue [45]

desired charge is collimated into a decay region, an air filled tube with a steel absorber at the end. In this decay region the mesons decay primarily via one of the following decays:

$$K^{\pm} \rightarrow \mu^{\pm} + \overset{(-)}{\nu}_{\mu}, \tag{4.2}$$

$$K^{\pm} \rightarrow \pi^{\pm} + \pi^{0}, \tag{4.3}$$

$$\pi^{\pm} \rightarrow \mu^{\pm} + \overset{(-)}{\nu}_{\mu}. \tag{4.4}$$

and produce either neutrinos or antineutrinos depending on the wanted mode. This results in a predicted peak muon neutrino purity of 93.6% in neutrino mode (see figure 4.2 and table 4.1 on the left hand side) and a predicted muon antineutrino purity of 83.72% in antineutrino mode (see figure 4.2 and table 4.1 on the right hand side). The BNB is intended to operate in neutrino mode and with a repetition rate of 5 Hz to 7 Hz [46]. To synchronize the neutrino beam with the experiments using the BNB, a synchronization signal called Tevatron Clock (TCKL) is sent to them. The TCKL contains several signals that can be used as a trigger for a neutrino beam spill. The two most important ones for the ANNIE experiment are "Booster Reset for MiniBooNe Beam Cycle" and "Booster Extraction Sync for a Beam Cycle" [47, 48] as they in coincidence function as a trigger for the detector systems indicating a neutrino beam spill.

Table 4.1: Peak neutrino flux prediction and fraction of total for muon (anti)neutrinos and electron (anti)neutrinos for the different run modes of the BNB [49]. The horn in neutrino mode is shown on the left hand side and the horn in antineutrino mode on the right hand side .

(a) BNB running in neutrino mode.

	Flux [$\nu/\mathrm{cm}^2/\mathrm{POT}$]	Fraction [%]
ν_μ	$5.19 \cdot 10^{-10}$	93.6
$\bar{\nu}_\mu$	$3.26 \cdot 10^{-11}$	5.86
ν_e	$2.87 \cdot 10^{-12}$	0.52
$\bar{\nu}_e$	$3.00 \cdot 10^{-13}$	0.05

(b) BNB running in antineutrino mode.

	Flux [$\nu/\mathrm{cm}^2/\mathrm{POT}$]	Fraction [%]
ν_μ	$5.42 \cdot 10^{-11}$	15.71
$\bar{\nu}_\mu$	$2.93 \cdot 10^{-10}$	83.73
ν_e	$6.71 \cdot 10^{-13}$	0.2
$\bar{\nu}_e$	$1.27 \cdot 10^{-12}$	0.4

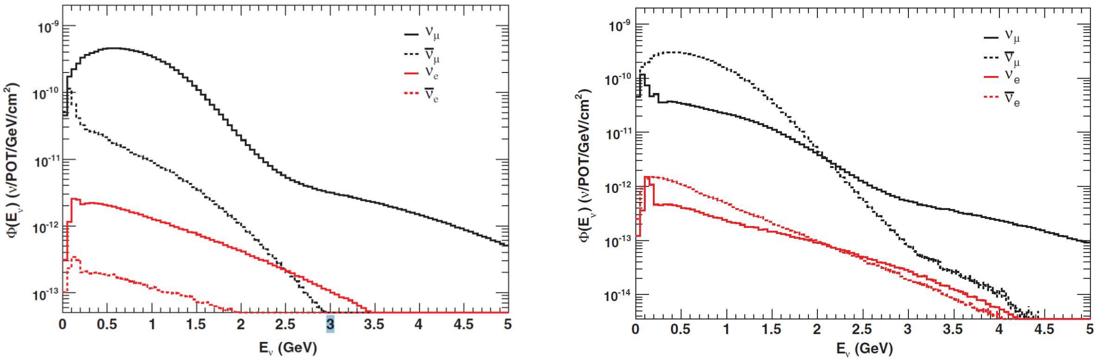

Figure 4.2: Neutrino flux prediction in dependence of neutrino energy for muon (anti)neutrinos and electron (anti)neutrinos for the BNB horn in neutrino mode on the left hand side and in antineutrino mode on the right hand side [49].

4.2 The ANNIE Detector

The ANNIE experiment aims to measure the final state neutron multiplicity using a muon neutrino beam and was thus designed to make full use of the geometric aspects of the beam direction. It consists of multiple subsystems to identify unwanted background as well as track producing particles. Since the detector has to be adapted to the neutrino beam coming from one direction its design is also non-symmetrical and directionally oriented. The full detector with all subsystems as well as the beam direction can be seen in figure 4.3. The full setup consists of three important detector subsystems: the Front Anti-Coincidence Counter (FACC), the tank detectors (PMT and LAPPD) and the Muon Range Detector (MRD). Additionally, a water filtration system for proper handling of the water in the tank is present and as an extension of ANNIEs Phase II an acrylic vessel filled with WbLS called Scintillator for ANNIE Neutrino Detection Improvement (SANDI) can also be inserted into the tank. In the following all the systems will be explained in more detail.

Front Anti-Coincidence Counter

The first subsystem the beam passes is the FACC, also called Front Muon Veto (FMV), which consists of two layers of stacked scintillator panels connected to PMTs for readout. It serves to veto activity that originates from the area in front of the detector hall [44]. Only interactions that have no FACC activity can be considered as possible neutrino interactions. The most likely source of vetoed events are muons that were produced by the neutrino beam in the dirt.

The water tank

The next system downstream is the main detector itself, which is a cylindrical steel tank 3 m in diameter, 4 m high and filled with high purity water. It is outfitted with 132 PMTs that are mounted on an octagonal steel structure inside the tank. To increase the low neutron capture cross-section of water (0.3 barn [50]) gadolinium was dissolved which increases the capture cross-section to 250 kbarn [51]. In total 0.2% $Gd_2(SO_4)_3$ were dissolved in the 26 tons of water [44]. There are two types of event structures that are interesting for further analysis. The first is the Cherenkov ring which is produced by the prompt muon of the CC neutrino interaction. Only interactions that produce clusters originating from this Cherenkov ring will be used further

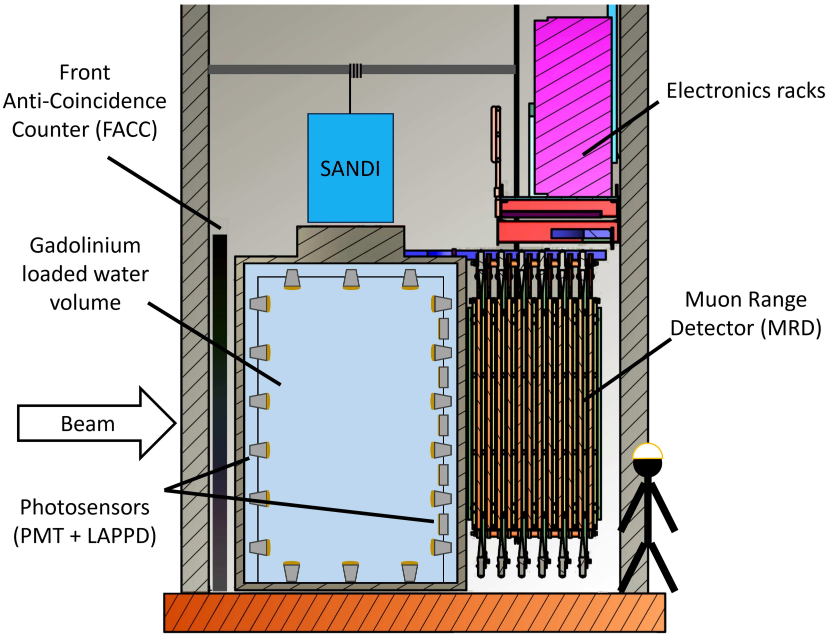

Figure 4.3: The ANNIE detector design schematic. The main features are from left to right: a Front Anti-Coincidence Counter, the main tank filled with Gadolinium loaded high purity water and photosensors and a Muon Range Detector. Above the main tank the Scintillator for ANNIE Neutrino Detection Improvement vessel is also shown [44].

on. The second is the delayed signal in form of the characteristic 8 MeV gamma cascade from potential final state neutrons captured by the gadolinium.
As a special feature the top of the tank can be opened in several places to allow for flexibility in installing additional systems including several R&D technologies. There are eight rectangular smaller hatches to slot in the LAPPDs between the PMT frame. During the scope of this thesis 3 LAPPDs were deployed. There are also five calibration ports for laser or radioactive source calibrations. Lastly there is a central 1 m wide circular hatch and its main use is to have general access to the tank as well as to deploy the later explained SANDI extension of ANNIE (see figure 4.4).

Muon Range Detector

The last of the detector systems is the MRD. It is a sandwich of 11 layers of alternating steel and scintillator layers with the scintillator plates being further divided into multiple panels connected to PMTs [44]. Its use is to detect muons with enough energy to leave the ANNIE tank which in the BNB energy range is most of them. A muon passing through the MRD loses energy along its path in the steel layers which are mainly there to make the muon lose as much energy as possible. The deposited energy in the scintillator layers allows for a reconstruction of the muon track in the form of its direction as well as the angle as it left the tank. This can also be used as a veto criteria since the length of the track in the MRD is correlated to its energy. Muons with an energy large enough to pass through and leave the MRD need to be discarded as a precise reconstruction of the muon energy is not possible since the energy is only partialy deposited and the energy the muon has left is unknown. Only events that allow for a full reconstruction of the muon energy, in this case muons that stop in the MRD, can be considered for further analysis.

Water filtration system

Since gadolinium is dissolved in the water the likelihood for materials to release particles into the water is non-negligible. To combat this a special water filtering loop has been installed. This is made up of a pump, a 5 μm filter for larger particles and dust, an UV lamp to prevent bacteria, a total-organic-carbon UV lamp for plastics, an anion resin for contaminants and lastly a 0.5 μm filter for smaller particles. After all of that the water is filled back to the tank [52]. There are also six deployed LEDs to monitor the water transparency on a regular basis. With this water filtration loop ANNIE has been able to keep the water transparency consistent over more than 5 years, even though there have been several (mock) deployments and changes to the tank systems which are sources for potential contaminations.

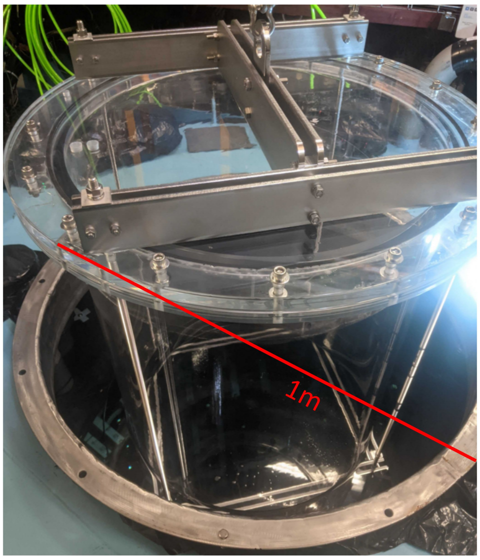

Figure 4.4: Picture of the SANDI vessel taken during a mock deployment. It is a 366 l acrylic cylinder with an inner height of 0.9 m and diameter of 0.72 m. The 1 m wide central hatch in the main ANNIE tank can also be seen [53].

Scintillator for ANNIE Neutrino Detection Improvement (SANDI)

One of the special deployments ANNIE did is the deployment of the SANDI vessel. It is a 366 l acrylic vessel with an inner height of 0.9 m and diameter of 0.72 m (see figure 4.4) [53]. It can be inserted into the main ANNIE tank via a hatch at the top-centre of the tank. The SANDI vessel is filled with WbLS which is explained in chapter 3.1. The production of scintillation and Cerenkov light will both take place and with the ultra-fast LAPPDs deployed in ANNIE a distinction of the two components in the time profile might be possible [54].

4.3 Measuring the final state neutron multiplicity

As lined out in the introduction of the chapter, the goal ANNIE aims to reach is the determination of the multiplicity of final state neutrons in water. Counting the final state neutrons will improve the understanding of the systematic uncertainties of neutrino energy reconstructions in oscillation experiments [44]. As the presence of neutrons is vital for the multiplicity measurements, a means to detect them has to be in place. In this case the gadolinium-doped water serves as

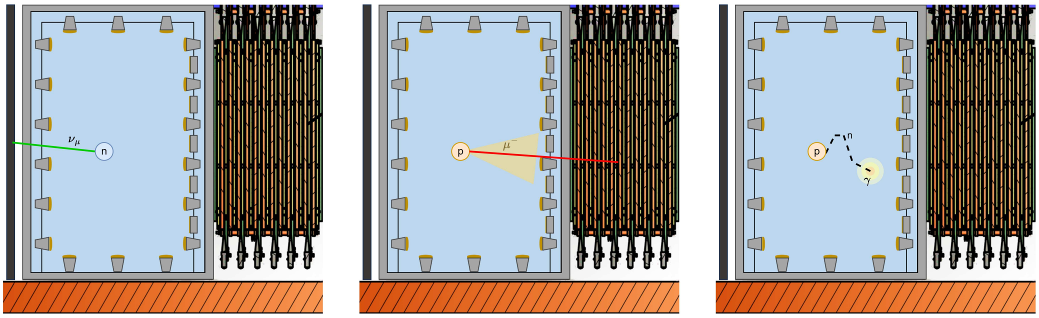

Figure 4.5: Schematic representation of an ANNIE CC event. Visible are the FMV, the ANNIE main tank and the MRD. From left to right an event progresses as the following: A ν_μ is interacting with a neutron of an oxygen molecule inside the water and a prompt muon is produced which in turn creates a Cherenkov ring on the PMTs. If additional neutrons are produced they will thermalize in the water until they are captured by a gadolinium nucleus and as a result an 8 MeV gamma cascade is emitted throughout the detector. The mean capture time of a neutron on gadolinium is around 30 μs and clearly distinguishable from the prompt Cherenkov radiation.

detector medium for the neutrons which instead of one 2.2 MeV gamma in the case of water, releases an 8 MeV gamma cascade. Since ANNIE uses a neutrino beam as its source the main channel for neutrino CC interactions in the water tank is on the oxygens' neutrons:

$$\nu_\mu + n \rightarrow p + \mu^- \ . \tag{4.5}$$

This in general implies that no neutrons will be produced by the main reaction channel making it a $\mathrm{CC}-0\pi-0\mathrm{n}$ interaction. The left hand side plot of figure 4.5 shows the neutrino interacting with a neutron. The centre plot in turn shows the primary result of the interaction, a prompt muon which creates a Cherenkov ring on the PMTs in beam direction. As the BNB delivers beam with a peak muon neutrino energy of 700 MeV, interactions are no longer only CCQE scattering but also CC-RES interactions are possible (see figure 2.2). In case of $\mathrm{CC}-0\pi-1\mathrm{n}$ or $\mathrm{CC}-1\pi-1\mathrm{n}$ event topologies where an additional final state neutron is produced, as described in chapter 2.2, the right hand side plot of figure 4.5 shows the interactions in the water tank. The final state neutron first thermalizes until it is captured by a gadolinium nucleus with a mean capture time of 30 μs [44] and the characteristic 8 MeV gamma cascade is released. Another way to get final state neutrons are the 2p-2h interactions described in chapter 2.2 where additional neutrons can be produced when a neutrino scatters on a correlated pair of nucleons. By looking at the reconstructed energy of events with a neutron count greater than zero, compared to the reconstructed energy of events without neutrons, ANNIE should be able to provide a good understanding of final state interactions [44].

4.4 Data acquisition and software in the ToolDAQ framework

The entirety of ANNIEs software is based on an independent C++ based framework developed by Benjamin Richards from the University of Warwick [55]. The idea is to have a framework that allows every person, regardless of degree or experience, to work in collaboration without requiring complicated introductions to pre-existing code or entire frameworks. This is done by introducing a Tool based structure in which programs that are usually done in one large

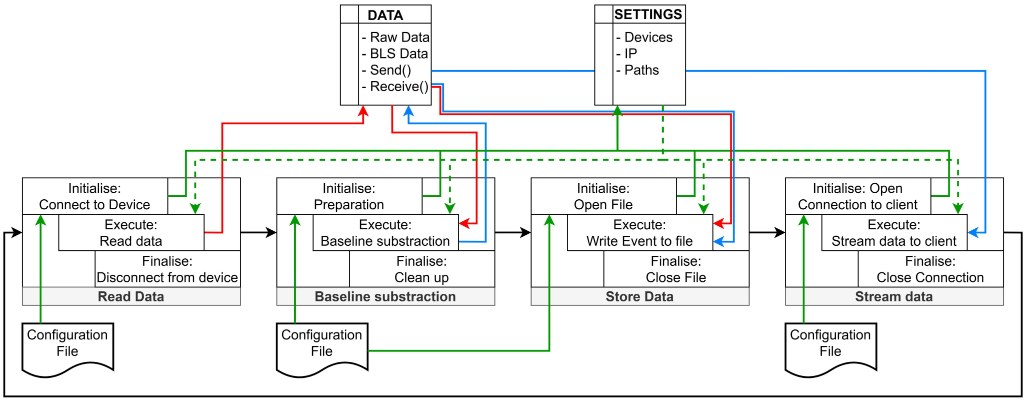

Figure 4.6: Structure of an example ToolChain based on the ToolDAQ framework. The example uses four Tools and two DataModels (DATA and SETTINGS) to display the overall functionality of the framework. The used Tools in this example are a Tool to read data from an arbitrary digitizer, a Tool to correct the baseline of the waveforms, a Tool to store the data on disk and a Tool to stream the data to a client. The green lines show the path of the settings, the red lines the path of the raw data and the blue lines the path of the baseline corrected data.

step/file are split into separate Tools that only do small portions of overall larger goals and adhere to defined inputs and outputs. This way future analysis/simulations/general code can use pre-exiting Tools instead of writing everything from scratch thus increasing efficiency and decreasing the potential for errors. The highly modular nature of the Tool system allows for a large degree of freedom which simplifies and streamlines all code sequences in general. This section will describe in more detail how ToolDAQ works, its general structure and how it is used in ANNIE. For this, it is easiest to consider an example as seen in figure 4.6. In the centre can be seen what is called a ToolChain and as the name suggests it is Tools that are strung together and run in a loop. This is the heart of ToolDAQs structure as the ToolChains can be arranged and executed in whatever order necessary. Additionally as all Tools are collected together several ToolChains can be based of similar Tools but executed in different ways.

In this example one iteration of the loop contains a Tool to read data from an arbitrary digitizer, a Tool to correct the data baseline, a Tool to save both raw and corrected data to disk and a Tool that in the end streams the corrected data to a client. The internal structure of a Tool is thereby always the same, first the "Initialise" part prepares for the "Execute" part by opening files, establishing connections, etc.. The "Execute" part is next and essentially the part that is repeated in the loop. Lastly, after all iterations of the loop are done or the execution is ended a "Finalise" part will close all connections or files and clean-up before ending the program altogether. What is important to know about this is that data from one Tool is a in itself closed class, meaning Tools have no access to the data of other Tools. To compensate for this and to make data easily accessible for all Tools and in general to supply Tools with outside information without hard coding them inside the Tool (as that would negate the usage of a multi purpose Tool structure) so called DataModels are introduced and can be seen in figure 4.6 above the row of Tools. DataModels are globally available classes that contain data structures needed for the intended purposes. In this example two DataModels are used, a data managing one that simply has an entry each for the raw data and corrected data, both as vectors, as well as two functions that are used for sending and receiving data. The second DataModel is a storage for necessary

settings that is used by all Tools for different purposes and it is usually populated during the "Initialise" part of the Tools. The information is sourced once at the start of the "Initialise" part from configuration files that can be either split so each Tool has its own file or in a way that Tools share the same file. This can be seen in the figure below the Tools row. Another use for the DataModels lies in the structured nature of ToolDAQ. As the whole framework is intended to be used collectively by multiple people DataModels make it easier to conform to a specific set of chosen data formats as they are defined globally in the DataModel.
To explain the sequence of events in the above example it starts with each Tool running their "Initialise" once, one after another, reading the data from the configuration file populating the corresponding DataModel and then using these configurations to prepare for their individual tasks. Next the "Execute" is run in sequence, one Tool after another, as often as set in the loop settings. First the data is read from an in this case arbitrary digitizer and the raw data is stored in the data managing DataModel, from where the second Tool grabs the data and does a baseline correction before storing it in the same DataModel as corrected data. Next the third Tool grabs both raw and corrected data as well as paths set for local storage to save the current event to file. Lastly the stream Tool grabs only the corrected data and streams it to a previously defined client using the "send" functionality already present in the DataModel. To receive this the client side only needs to grab the DataModel as well and use the "receive" functionality. With the event now stored on disk and streamed the next iteration begins and repeats until all events are done or the ToolChain is ended manually. Similar to the "Initialise" the "Finalise" runs once for each Tool and after cleaning up ends the overall execution of the framework.

ToolDAQ also has multiple third party software libraries integrated into its base functionality. The two most important ones are BOOST [56] and ZeroMQ (ZMQ) [57]. BOOST in itself is a collection of several C++ libraries that offer a large variety of functionalities. Derived from these libraries is a custom made data structure specific to ToolDAQ which ANNIE uses to store all of its data in. This data structure is called BoostStore and it is similar to a C++ map structure where data is always stored in key and value pairs. Other than its C++ map counterpart the BoostStore fixed the data type for the key to be a string but in return allows the value data type to be completely arbitrary. Any data type or even other BoostStores can be used as value. The latter is the data structure used for ANNIE as it uses nested BoostStores where the lower key BoostStores are subsystem specific and separated into PMTs, MRD, Trigger and LAPPD. If this data structure is saved to disk it will be in a binary format which also increases handling speed as well as reduce the required disk space. ZMQ on the other hand is a software library mostly used for the communication between applications. In the ANNIE experiment it is mainly used to send data between different instances of ToolDAQ like the main DAQ ToolChain running on one computer and the device specific ToolChains running on different computers. In the above example it is what will stream the data to the client and is part of the DataModels "send" and "receive" functionality.

Lastly this chapter will introduce the ToolChain running on the main ANNIE computers and will henceforth be called the main (ANNIE) DAQ [58]. The ToolChain can be seen in figure 4.7 and shows both the main ToolChain as well as the sub ToolChains running simultaneously for the different detector subsystems. The three subsystem ToolChains are for the MRD, the LAPPDs and the PMTs. Each of these ToolChains works in the same manner: Trigger informations are evaluated and if a subsystem meets their respective trigger condition the read out happens. In the case of the main DAQ this means that the Tool responsible communicates with its hardware counterpart respective to the subsystem. For the MRD it is LeCroy time-to-digital converters (TDC), for the LAPPDs the RPis that are connected to the PSEC4 chips and for the PMTs it is three separate Versa Module Eurocard (VME) machines outfitted with digitizers. In the LAPPD case the receiving Tool is using the same DataModel as the LAPPD-DAQ interface which will be described in chapter 5.3.2 Afterwards monitoring data is sent to the Monitoring systems and data is stored in output files.

The other Tools in the main ToolChain are mostly responsible for additional tasks like database connections, getting run settings, Slack communications, high voltage control and the main Monitoring update.

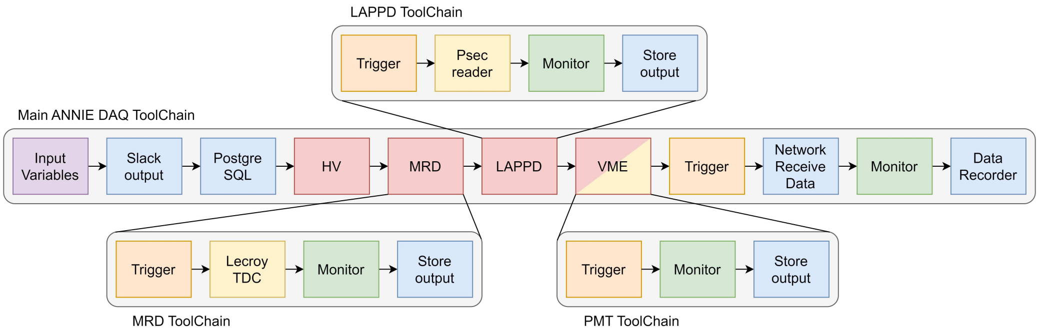

Figure 4.7: Structure of the main ANNIE DAQ ToolChain as well as the ToolChains running for each subsystem which are shown in red. Each of these Tools corresponds to a separate ToolChain it communicates with. For the MRD and the LAPPDs the hardware communication happens within these separate ToolChains as indicated by the yellow Tools. The PMTs (VMEs) on the other hand have the hardware communication on a different system altogether. The other Tools are split into trigger (orange), monitoring (green), outputs (blue) and inputs (violet) [58].

5 Deployment and commissioning of the LAPPDs in ANNIE

"I am and always will be the optimist. The hoper of far-flung hopes and the dreamer of improbable dreams."

- Dr Who, 11th Doctor

As introduced in chapter 4.2 the ANNIE water tank has a top cover with several slots to accommodate R&D technologies. One of the most important are the Large Area Picosecond Photodetectors as described in chapter 3.3.2. Since they are a new state of the art detector technology and have never been used in a large scale experiment a lot of preparation has to go into the deployment and commissioning of each of these novel detectors. The expected impact LAPPDs will have on ANNIE in particular can be seen in figure 5.1. The vertex and direction resolution for the ANNIE detector is shown in blue for the case of only PMTs and in red for the case of PMTs and five LAPPDs. An improvement of a factor of roughly 4 in vertex resolution and a factor of 2 in direction resolution can be seen for 68 % successfully reconstructed events. The addition of LAPPDs to the ANNIE tank could vastly improve its reconstruction capabilities since LAPPDs are generally their own independent 2D detector and even one alone can contribute heavily to the reconstruction of events [59]. As LAPPDs have never been used in a large scale experiment these deployments also serve as a test for the use of LAPPDs in future experiments.

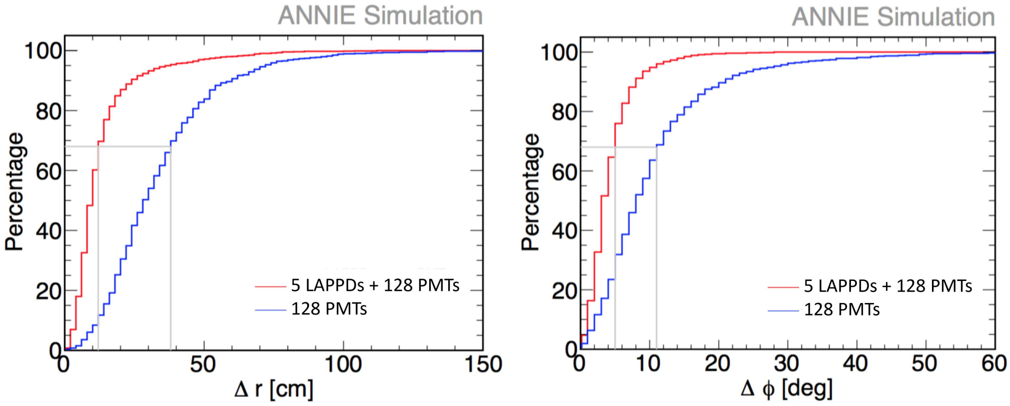

Figure 5.1: The left hand side shows the expected vertex resolution and the right hand side the expected direction resolution for reconstructed events in the ANNIE detector. In blue the case for only PMTs is shown, while the red line shows the case for PMTs and five LAPPDs [59].

This chapter will introduce all aspects necessary for the deployment of the first ever LAPPD as well as the subsequent LAPPDs. This includes the introduction of the deployment-ready LAPPD underwater package with its components and connections to the surface, as it offers a good overview of the entire system required to utilize an LAPPD. The chapter will then continue with the explanation of the characterisation procedures of the LAPPDs in a laboratory environment as preparation for the deployment and characterisation of the detector parameters. Afterwards, the software developed for interfacing with the Slow Control (SC) and Data Acquisition (DAQ) will be explained in detail. Lastly the deployment of the first LAPPD in March 2022, the first neutrino data and data taken with three LAPPDs, deployed February 2023, will be presented.

5.1 Underwater housing and surface connections

Due to the LAPPD being its own independent 2D, 56-channel detector it quickly becomes very complicated in terms of its interfaces and general operation. To introduce the full system an overview of the entire Underwater Housing (UWH) as well as the surface system is shown in figures 5.2 and 5.3 respectively. The underwater system can be further divided into the LAPPD, the ACquisition and Digitization with PseC4 (ACDC) boards mounted directly onto the LAPPD and the Low-Voltage-High-Voltage (LVHV) board responsible for all SC related tasks. The ACDC boards are mounted to the LAPPD to reduce the required number of signal carrying cables from the tank to the surface and to reduce noise. As such the digitization happens directly at the LAPPD level. To accommodate this the commercial SMA connectors are removed and replaced with a custom pick-up board that directly feeds into the two mounted ACDC boards. Each of those boards is equipped with five PSEC4 Application-Specific-Integrated-Circuit (ASIC) Analog-Digital-Converters (ADC), each having six channels for a total of 30 channels per ACDC board. Table 5.1 shows some of the featured characteristics of the PSEC4 chips. Additionally mounted between LAPPD and the ACDC boards is a custom designed Triggerboard (TB) which reads all channels of one side of the LAPPD and compares them via multiplicity-comparators. If the value of the multiplicity-comparators exceed a settable threshold it will produce a short square pulse which is fed into each ACDC using two leftover of the 60 available channels. These signals will function as self-trigger signals for the ACDC boards by feeding the signals via a Field-Programmable-Gate-Array (FPGA) into the PSEC4 ASICs, triggering a simultaneous readout of all PSEC4 chips. The digitized data is then transferred to the surface via two RJ45 cables. This will be further explained in the DAQ chapter 5.3.2.

Table 5.1: Excerpt of the parameters table for PSEC4 chips [60].

Parameters	Value
Channels	6
Sampling rate range [Gs/s]	4-15
Used sampling rate [Gs/s]	10
Samples/channel	256
Recording buffer time [ns]	25.6

The other board in figure 5.2 at the bottom is the Low-Voltage-High-Voltage board, responsible for supplying the LAPPD with high voltage (HV) and the ACDC boards, the TB and itself with three different low voltages (LV). The LVHV is also responsible for setting the thresholds on the TB as well as reading several environmental sensors. The communication to the LVHV is done via a Controller Area Network Bus (CanBus) interface running on a Raspberry Pi (RPi) which will be further discussed in the slow control chapter 5.3.1.

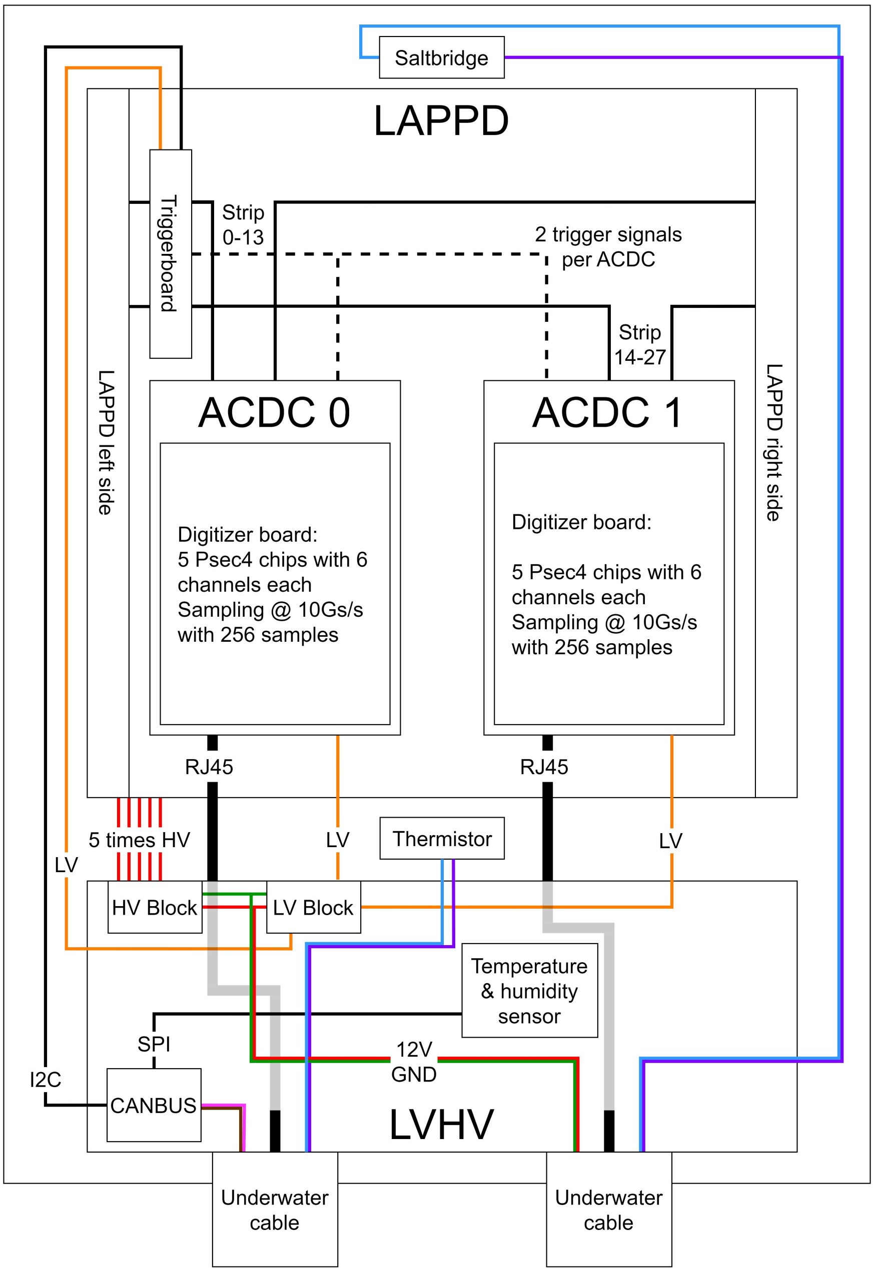

Figure 5.2: Schematic drawing of the LAPPD underwater housing with all its components and connections. The main components are the LAPPD with the attached Triggerboard as well as the two ACDC boards. The other main component is the LVHV board, which is responsible for power supply and sensor readout. The internal LVHV connections as well as its external connections to the other components are shown as well. The low voltage lines are shown in orange, the high voltage lines in red and the data lines in black. The connections going to the surface are a voltage-ground pair (red/green), the CanBus (pink/brown), the passive sensors (blue/purple) and two RJ45 cables for the LAPPD data. The shown schematic is upside down to its position once deployed but all components are placed in respect to their assembled positions.

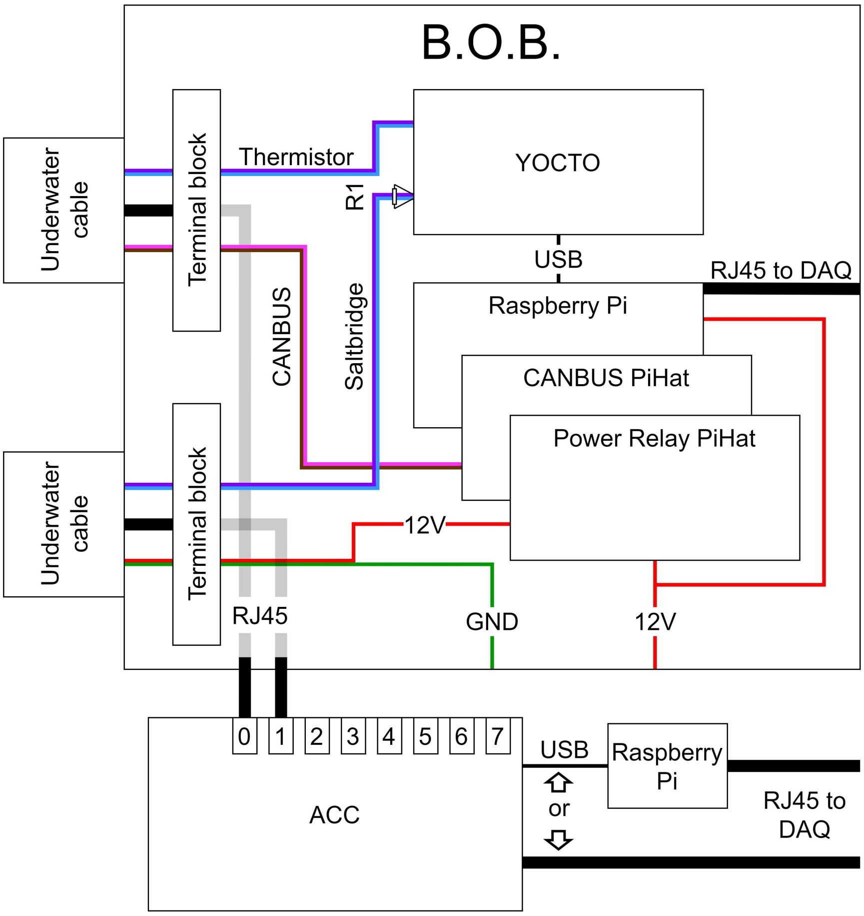

Figure 5.3: Schematic of surface electronic connections to the B.O.B.. The connections from/to the UWH are two RJ45 cables carrying the LAPPD data (black), a voltage-ground pair (red/green), the CanBus (pink/brown) and two twisted pairs for the passive sensors (blue/purple). The CanBus is connected to a RPi hat, the two twisted pairs for passive sensors are connected to the YOCTO device which in turn is connected to the SC-RPi via USB and the power twisted pair is connected to a relay on another RPi hat and then to an external power source. The two RJ45 cables are connected to the ACC which is connected to the main DAQ system either directly via Ethernet or via USB requiring an additional RPi as intermediate device.

This totals in four twisted pairs and two RJ45 cables that need to be connected underwater. The whole systems can be split into a DAQ system which uses the RJ45 cables and is responsible for configuring the ACDC boards and reading the data recorded by them and a SC system which uses the twisted pairs (One pair for CanBus, two pairs for passive sensors and one pair for voltage/ground) to read out the environmental sensors and supply bias voltage which then is split into HV and LV. The SC systems environmental sensors and controllable components can be seen in table 5.2 and are further discussed in chapter 5.3.1. Once the signals reach the surface the two underwater cables connect to a NIM-module sized unit called Break-Out-Box (B.O.B.) which feeds the incoming signals to their respective devices. The two RJ45 cables (data) are fed to the ANNIE Central Card (ACC), a custom developed card responsible for collecting data from up to 8 ACDC boards. The ACC in turn can be either connected directly to the main

DAQ system via Ethernet or to a RPi via USB as intermediate step. This RPi will be called DAQ-RPi from now on. The other connections are routed to a different RPi, henceforth called SC-RPi, equipped with two RPi hats. The CanBus is connected to one RPi hat, the two twisted pairs for passive sensors are connected to a separate device called Yoctopuce Maxi Thermistor (YOCTO) [61] which in turn connects to the SC-RPi via USB and lastly the power twisted pair connects to a relay on the other RPi hat and then to an external power source.

Table 5.2: Environmental sensors used in the UWH with their respective communication line and position in the housing.

Sensor	Unit	Communication line	Position
Temperature	°C	CanBus together with humidity	Central on LVHV
Humidity	%	CanBus together with temperature	Central on LVHV
Thermistor	Ω	Twisted pair 1 as resistance	Between LVHV and LAPPD
Saltbridge	Ω	Twisted pair 2 as resistance	Bottom of UWH
HV	V	CanBus as read and write	On LVHV
LV	V	CanBus, three voltages combined	On LVHV
Threshold TB 0	V	CanBus as read and write	Between LAPPD and ACDC
Threshold TB 1	V	CanBus as read and write	Between LAPPD and ACDC

5.2 LAPPD characterisation measurements

Any LAPPD needs to be thoroughly characterised and understood before it can be deployed or even assembled into its UWH. Therefore a dedicated test setup has been build in a laboratory on-site by collaborators from Iowa State University and University of California Davis (UC Davis). This setup includes a darkbox, a picosecond-laser and a small scale DAQ system derived from the full LAPPD DAQ interface (see chapter 5.3.2) developed as part of this thesis. The characterisation of the LAPPD includes several objectives including for example:

- QE uniformity over the LAPPD photocathode,
- gain vs bias determination,
- scans along and across anode strips,
- checking for correct timing characteristics,
- working condition of all components as well as environmental sensors.

As an example some of the characterisation data for LAPPD64, taken by the same collaborators on-site, has been analysed as part of this thesis and the results are shown in figures 5.4 to 5.7. Some steps are necessary to make the data usable for the characterisation analyses, but these steps will be introduced later in chapter 5.4.2.

Starting with figure 5.4 the first measurement is to determine the bias voltage used to run the LAPPD which will then be used for all further characterisations and deployment. The voltage is applied as one top to bottom voltage which is split on the LVHV and then internally distributed. This voltage is scanned from 2275 V to 2350 V in 25 V steps and at each voltage setting 75000 laser triggered events at the same position are taken. The four charge distributions are each shown with the single photoelectron (s.pe.) peak and Gaussian fits to determine the gain, which was determined from the charge histogram of the integrated waveforms with

$$\begin{aligned} Q &= \frac{1}{R}\int_0^{25.6\,\mathrm{ns}} U(t)\,\mathrm{d}t \quad , \\ \text{Gain} &= \frac{Q_{spe} - Q_{pedestal}}{\mathrm{e}} \end{aligned} \tag{5.1}$$

where R is the termination of $50\,\Omega$ and e the electron charge. The charge difference for the non-zero pedestal position is taken to account as well. What can be taken from table 5.3 is that as expected all determined gains move to higher values for higher bias voltages. To get a gain as high as possible it is decided that the final bias voltage used for deployment will be 2350 V which corresponds to a gain of $(1.110 \pm 0.144)\,10^7$, the error being a 1σ fit error. Compared to the expected gain of $1.26 \cdot 10^7$ at 2500 V [38] this is within an acceptable range of difference.

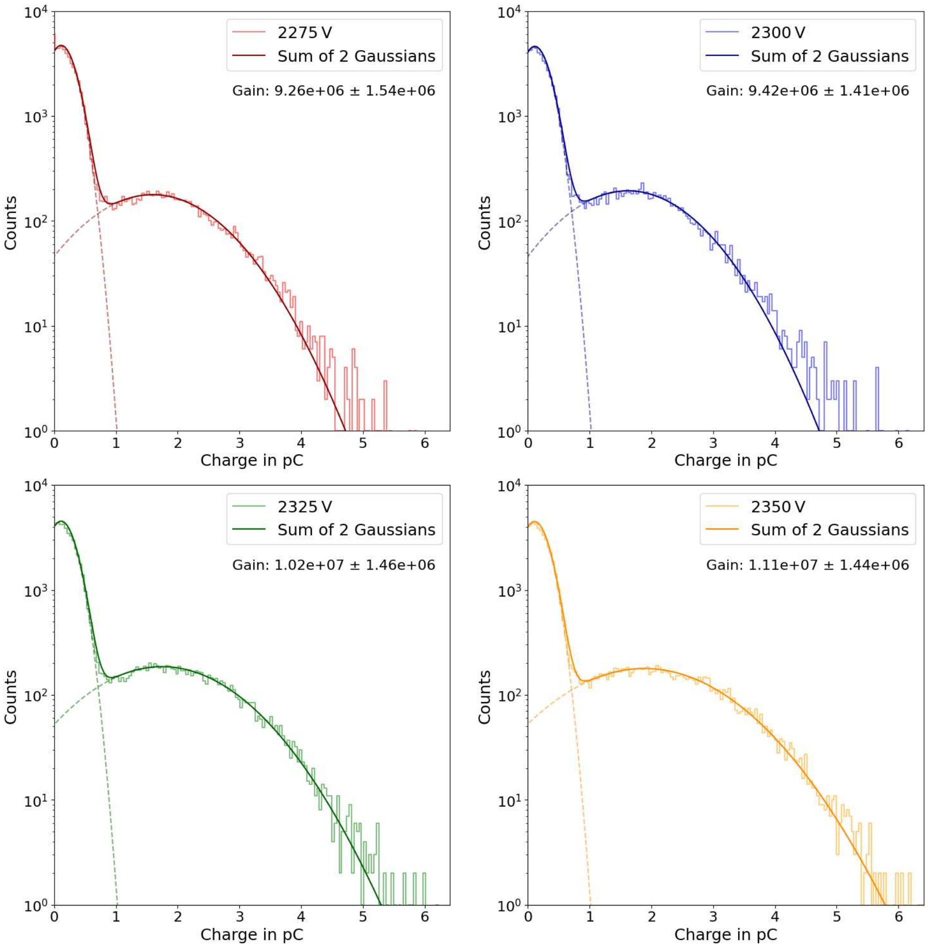

Figure 5.4: Characterisation data for LAPPD64: Gain vs Bias voltage for a scan over four voltages. The data was taken at an on-site laboratory at FermiLab. Shown are the charge distributions together with a double Gaussian fit for pedestal and s.pe. peak to determine the gain.

The plot in figure 5.5 shows the transit-time distribution and the accompanying Gaussian fits. This dataset was taken by determining the time from laser output to signal recording. The important part for this is that the laser has a short enough pulse width (in this case 45 ps [62]) to not smear the TTS. Since in this case the TTS was determined for s.pe. levels a significantly

Table 5.3: Results of the gain vs bias voltage scan for LAPPD64. The errors shown are the 1σ fit errors.

Bias Voltage [V]	Gain [10^7]	Gain Error [10^7]
2275	0.926	0.154
2300	0.942	0.141
2325	1.021	0.146
2350	1.110	0.144

high statistics has to be accumulated which in this set is around 250000 events of which around 10% contain a valid s.pe. pulse. What immediately becomes obvious is that instead of the normal expected single Gaussian distribution, two peaks are present with a distance of roughly 300 ps which is not explainable by any outside causes like reflections or similar unaccounted distances. The cause in this case is a small discontinuity coming from the wrap around point of the circular buffer structure of the capacitors used in the ADC [63]. If the expected position of the pulses given by the delay due to signal paths and firmware delays is exactly around this wrap around point the pulse can jump around the discontinuity causing this double peak structure. This is a good example of the necessity for these kind of characterisations as they can show issues that can occur in later analyses. Now accounting for this and the relative position of laser trigger and pulse position in time the second of the peaks is representative for the actual TTS. The result of this is a total time resolution corresponding to the sigma of the Gaussian fit of (97.35 ± 0.09) ps. Unfolding the laser pulse width from the total time resolution via

$$\sigma_{LAPPD} = \sqrt{\sigma^2_{total} - \sigma^2_{Laser}} \tag{5.2}$$

results in an LAPPD time resolution of (86.33 ± 0.11) ps.

Figures 5.6 and 5.7 are also laser characterisation data but this time focusing on the spatial aspects and the ability of the LAPPD to distinguish events at different positions. Figure 5.6 on the left hand side shows a 2D view of an LAPPD surface. The x and y axes correspond to the real position on the LAPPD while the z axis shows the normalized integrated charge of all events. The shadowed bars are the strip lines. In this case the laser was aimed at the centre of the sixth strip line from the bottom and to the right hand side in x direction. The reconstruction of a single position works as explained in chapter 3.3.2 and is done for each event with at least one s.pe. pulse on any of the strip lines. The resulting reconstructed charge distribution can be seen centred on the sixth strip line in y direction and and to the right hand side in x direction. The reconstructed position of the laser is shown as a plus symbol (green) while the cross (magenta) shows the original position of the laser. The reconstructed position is determined as

$$x = (159.4 \pm 2.62)\ \text{mm},\ y = (38.54 \pm 0.8)\ \text{mm} \tag{5.3}$$

for the x,y position and compared to the original position of

$$x = 158.2\,\text{mm},\ y = 38.8\,\text{mm} \tag{5.4}$$

is within the margin of error. The right hand side shows the corresponding histograms of the reconstructed x and y coordinates. The x coordinates show a Gaussian like distribution which is mostly dominated by the spread of the laser output and the resulting spread of the charge cloud on the strip line. The y coordinates on the other hand show distinct peaks at the position of the sixth strip line with a small spread around it.

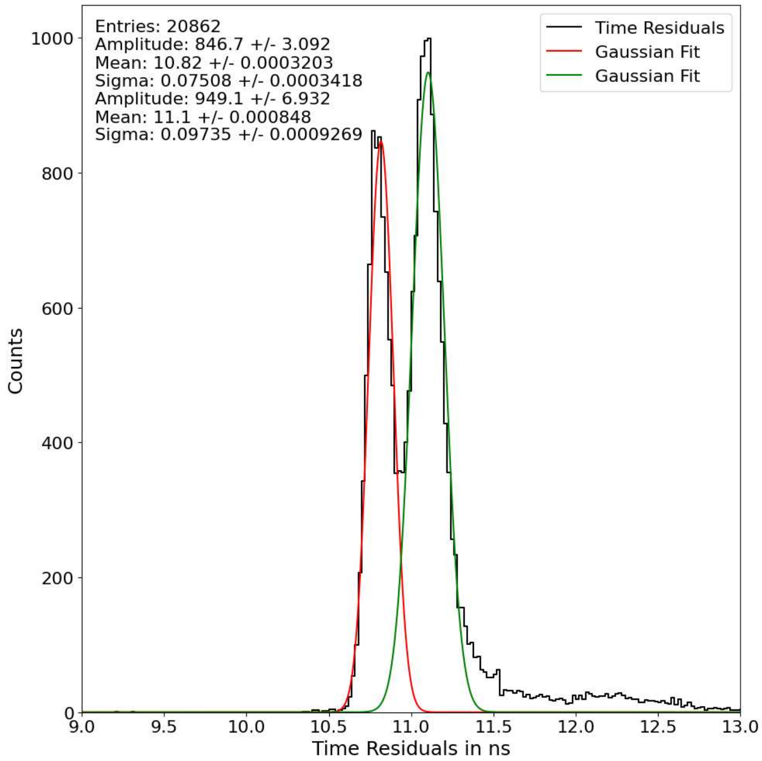

Figure 5.5: Characterisation data for LAPPD64: TTS distribution for data taken at an on-site laboratory at FermiLab. A two peak like structure can be seen in which the first peak is an artifact due to the wrap around point of the circular buffer structure used in the ADC. The second peak is the actual TTS of the LAPPD.

Figure 5.7 on the other hand shows the laser aimed between the eighth and ninth strip line from the bottom. The resulting charge distribution can be seen spread over multiple strip lines. The reconstructed position of the laser is

$$x = (168.6 \pm 1.91)\ \text{mm},\ y = (56.54 \pm 0.55)\ \text{mm} \tag{5.5}$$

compared to the original position of

$$x = 168.9\,\text{mm},\ y = 57.8\,\text{mm} \quad . \tag{5.6}$$

What can be seen is that even though the statistics for this run was low compared to the on-strip run the error of the x,y position reconstruction is smaller than the one for high statistic run. Since in this case the reconstruction of the x,y coordinate can use the weighted average over multiple strip lines the error gets smaller. The right hand side shows a histogram of the hit distributions for x and y coordinates similar to before. In this case however the y coordinates show three distinct peaks at the positions of the eighth and ninth strip line as well as a peak in between them. This shows that in cases where the photon hits above an area between two strip lines only one strip line may carry all of the resulting charge, resulting in a position reconstruction on only this strip line while for others the charge is distributed in multiple strip lines. With these characterisations and a good understanding of the LAPPD the assembly into the UWH can be done and the deployment can begin.

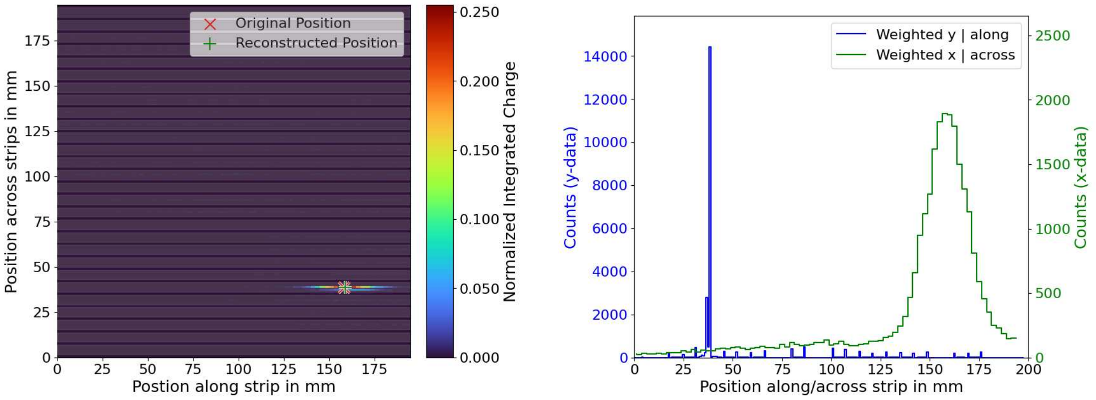

Figure 5.6: A 2D histogram where the x and y dimensions correspond to the real position on the LAPPD and the z axis shows the normalized integrated charge deposited by a sum of events. Also shown are the original laser position (magenta cross) as well as the reconstructed position (green plus) as per the methods described in chapter 3.3.2. The shadowed bars indicate the position of the strip lines. The left hand side shows a data set with high statistics at s.pe. level with the laser pointed at the centre of the sixth strip line in y direction and on the right hand side in x direction. The right hand side shows the histograms of the hit distributions for x and y coordinates.

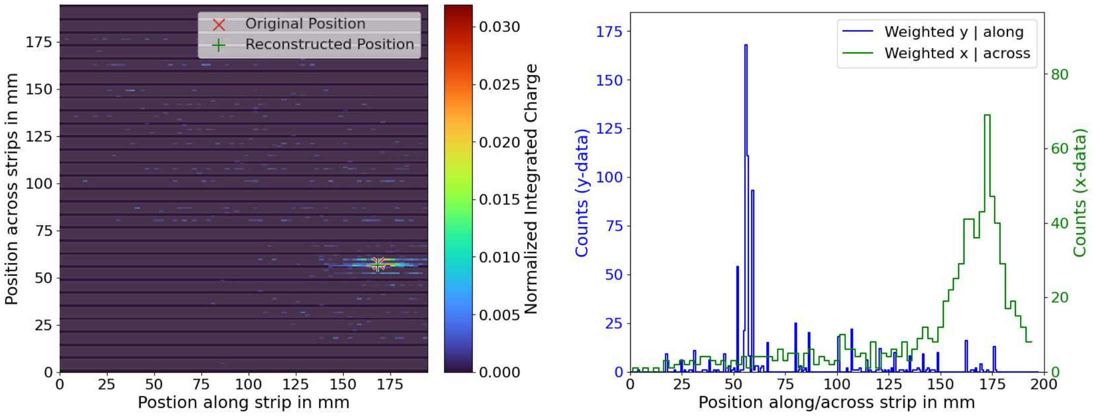

Figure 5.7: A 2D histogram where the x and y dimensions correspond to the real position on the LAPPD and the z axis shows the normalized integrated charge deposited by a sum of events. Also shown are the original laser position (magenta cross) as well as the reconstructed position (green plus) as per the methods described in chapter 3.3.2. The shadowed bars indicate the position of the strip lines. The left hand side shows a data set with low statistics at s.pe. level with the laser pointed between the eighth and ninth strip line in y direction and on the right hand side in x direction. The right hand side shows the histograms of the hit distributions for x and y coordinates.

5.3 Software Interfaces between the LAPPD and the main systems

In the scope of this thesis, two software interfaces have been developed to integrate the LAPPDs into the main ANNIE software environment. The first is the interface with the Slow Control, which generally includes all systems that operate on a non-LAPPD event, non-time sensitive level. Examples for these kinds of systems are voltage controls, sensor read-back (including environmental sensors as well as supplied voltages) and emergency systems required to shut down the LAPPD in case of a critical event. In the case of an underwater deployment like in ANNIE the necessity for such a system in case of flooding is very high. The second interface is the Data Acquisition interface which is responsible for the data readout and the configuration of the LAPPD or rather its attached ACDC boards. The following sections will introduce the hardware and software side of both interfaces in more detail as well as show requirements and produced results.

5.3.1 Slow Control

The Slow Control is meant to interface with all systems that operate on a non-LAPPD event, non-time sensitive level. The available sensors and controllable devices have already been introduced in table 5.2 in chapter 5.1 and can be split into four subsystem: The high voltage/low voltage control which is responsible for supplying all systems with their necessary bias voltages and the LAPPD with a variable HV, the active environmental sensors (like temperature and humidity), the passive environmental sensors (like the saltbridge and the thermistor) and the TB which is responsible for setting the threshold of the LAPPDs self-trigger. The following paragraphs will describe the hardware and software side of the SC systems in more detail:

Hardware Setup

The hardware setup of the SC system can be seen in the schematic diagram in figure 5.2 and 5.3 and the several sensors and accessible components are listed in table 5.2. The central instance for the SC is the SC-RPi which runs a modified version of ToolDAQ (see chapter 4.4) responsible for setting, reading and transferring all SC data between the LAPPD/UWH and the main ANNIE systems. The SC-RPi is equipped with two extension hats, one for the CanBus communication interface and one as a relay for the main voltage line, and a YOCTO device connected via USB. The YOCTO device is a USB interface for thermistors which measures the resistance of a given device that can be calculated into a respective temperature. All SC devices can from here on be categorized as active or passive devices, depending on their connection to the SC-RPi. Devices connected to the YOCTO hub are passive as they do not require power underwater. Instead they are solely controlled by the YOCTO hub and used for resistive measurements. With this the passive sensors can work at all times, even if the UWH is completely shut off. The first passive sensor is the thermistor which if read out by the YOCTO hub as a resistance can be calculated to a respective temperature via a formula determined by on-site measurements of collaborators from UC Davis

$$T\,[^{\circ}\mathrm{C}] = -\frac{\ln\left(\frac{R[\mathrm{k}\Omega]}{29.4}\right)}{0.0437} \quad . \tag{5.7}$$

This thermistor is positioned at the upper edge of the LAPPD below the LVHV board. As such the temperature given by the thermistor is the closest one to the actual temperature of the LAPPD. The second passive sensor is the saltbridge which sits at the very bottom of the UWH and is used to detect water leaks into the housing. The saltbridge in general is a simple salt filled tube with contacts at each end which allows for a resistance measurement. Since the resistance of such a tube would be above the limit of the YOCTO hub a resistor ($\sim 600\,\mathrm{k}\Omega$) is put in parallel to the saltbridge input. If water touches the salt in the saltbridge tube the resistance drops from a few hundred $\mathrm{k}\Omega$ to only a few ten $\mathrm{k}\Omega$ and a leak can be clearly detected and emergency measures can be taken.

Active sensors are those that require power via the relays on the RPi hat and are located in the UWH. The interface to communicate with the sensors is a CanBus connection between the RPi CanBus hat and the LVHV board located in the UWH. The relays function as overall power transfer to everything located in the water tank and as such also functions as a measure of emergency power cuts. The LVHV board is the central SC board and all active sensors and bias voltages to data lines (although in this case passively) are routed through this board. The available sensor via the CanBus line is the temperature and humidity sensor which is positioned as a single sensor central on the LVHV board and is placed close to the hottest spot in the entire UWH. The temperature and humidity sensor communicates with the LVHV board via Serial Peripheral Interface (SPI) lines and returns a single value in one CanBus message. This returned value can then be used to calculate the temperature and humidity as described in the data sheet [64]:

$$T\,[^\circ\mathrm{C}] = \frac{\text{value}}{2^{14}-2}\cdot 165 - 40 \quad , \quad H\,[\%] = \frac{\text{value}}{2^{14}-2} * 100 \quad . \tag{5.8}$$

The other components that are accessed via the CanBus interface are the TB thresholds and their read back via an Inter-Integrated Circuit (I2C) line. The threshold is thereby set and read back respectively via [65]

$$\text{threshold}_{\text{set}} = \frac{\text{setting}\,[\mathrm{V}]\cdot 4096}{2.048\,\mathrm{V}} \quad , \quad \text{threshold}_{\text{read}}\,[\mathrm{V}] = \frac{\text{value}\cdot 2.048\,\mathrm{V}}{4095} \quad . \tag{5.9}$$

The last components that are accessed via the CanBus interface are the HV and LV voltages which are set via dedicated HV and LV-blocks mounted on the LVHV board. The HV is set via a Digital-Analog-Converter (DAC) for which the desired voltage needs to be transformed to a compatible 12-bit format. It is then sent to the DAC with [65]

$$\text{dac}_{\text{setting}} = \frac{2^{12}\cdot \text{dac}_{\text{input}}\,[\mathrm{V}]}{2.048\,\mathrm{V}} \quad , \tag{5.10}$$

and read back via an ADC with [65]

$$\mathrm{HV}\,[\mathrm{V}] = \text{adc}\cdot 0.00518\,\mathrm{V}\cdot 1000 \quad . \tag{5.11}$$

For the LV a setting of the values is not available as they need to be at a fixed value for the connected components to function correctly. The read-back in this case is done by the LV-block and all values are collected by the LVHV board and sent in a single CanBus message to the SC-RPi. The three voltages can be extracted by taking bits 0:15, 16:31 and 32:47 of the CanBus message and transforming them to voltage values via the same ADC as before with [65]

$$\begin{aligned} \mathrm{LV}_1\,[\mathrm{V}] &= \text{adc}\,[0{:}15]\cdot 0.00518\,\mathrm{V} \quad , \\ \mathrm{LV}_2\,[\mathrm{V}] &= \text{adc}\,[16{:}31]\cdot 0.00518\,\mathrm{V} \quad , \\ \mathrm{LV}_3\,[\mathrm{V}] &= \text{adc}\,[32{:}48]\cdot 0.00518\,\mathrm{V} \quad . \end{aligned} \tag{5.12}$$

This concludes the hardware setup of the SC system and the way the data can be accessed. The following section will introduce the software side of the SC interface.

Software

The software developed for the SC interface is meant to work as an independent system that can run without the necessity of the main ANNIE systems to be active. For this the software is running on the SC-RPi specifically meant for the SC and each LAPPD has its own device making each LAPPD-SC its own environment. The software is based on ANNIEs C++ based framework ToolDAQ (see chapter 4.4 for framework details) although it was modified to accommodate the CanBus and YOCTO interfaces. The YOCTO already comes with its own software libraries and can be integrated directly making the communication easy. The CanBus interface on the other hand is more complicated. Although a software library exits for CanBus communications it is not natively capable of sending hexadecimal values like the YOCTOs USB communications can since the data to be sent needs to be transformed into a CanBus message frame first. CanBus in general is a communication protocol which is based on a message system where each message can contain up to 8 bytes of data. The messages are then sent to a specific address and can be read by any device that is connected to the CanBus network. It also requires a specific message ID for each data package sent thus making it possible to distinguish and prioritize incoming and outgoing messages. In this case the message ID is used by both the LVHV board as well as the SC-RPi to distinguish between different SC components as well as if either read or write is requested or used. The full structure of a CanBus frame is shown in appendix A. The parsing of identifier and data, the correct transformation into a CanBus message frame as well as the connection to the CanBus network is taken care of by the SCs software CanBus interface. Another aspect of the CanBus communication is the response time of the LVHV board as once the SC software requests data or waits for feedback after sending a setting, the CanBus interface needs to be paused long enough to allow the LVHV board to be able to collect the necessary information and build a CanBus frame to send. If the SC software does not wait long enough the LVHV board will not be able to respond and the communication will fail or worse messages will be cut into pieces. This is especially important for the HV ramping as it is done via the CanBus interface and the LVHV board needs to be able to reach the required voltage and read it back before the SC software can continue with the next voltage step. A cut message could interrupt or mis-set the voltage settings.

A schematic flowchart of the overall software structure can be seen in figure 5.8. As indicated in the figure the whole SC software can be divided into 4 parts: "Receive", "Set", "Poll" and "Stream". As ToolDAQ is the basis for this software the "Reveive", "Set" and "Stream" parts are directly adapted into ToolDAQs characteristic Tools. The "Poll" part on the other hand is split into each of the individually addressable components which then are adapted into their individual Tools. As Tools are meant to be as simple as possible the "Receive" Tool (green) is only responsible for receiving settings from an outside source (in this case a script running on the same SC-RPi) or local files and handing it over to the related DataModel. As this is only executed once per ToolChain loop the necessity for a further division is not given. Similar is true for the "Set" Tool (red) as it is only accessed if new settings are received and if executed it also runs only once for each "Receive". What also should be mentioned for the "Set" Tool is that depending on the change in the settings a specific sequence of operation needs to be followed. As they differ from each other a combined "Set" Tool is easier in both execution as well as error handling. Lastly the "Stream" Tool (orange) is analogue to the "Receive" Tool only responsible for sending the collected data, and for the sake of completeness the settings, to the main ANNIE monitoring systems. As such it sends one collective set of data and no further division is necessary.

The "Poll" Tools (blue) on the other hand are responsible for the communication with the connected components and as such it benefits to keep the overall ToolDAQ structure in mind and keep the Tools as simple as possible. In this case a split into different devices not only keeps

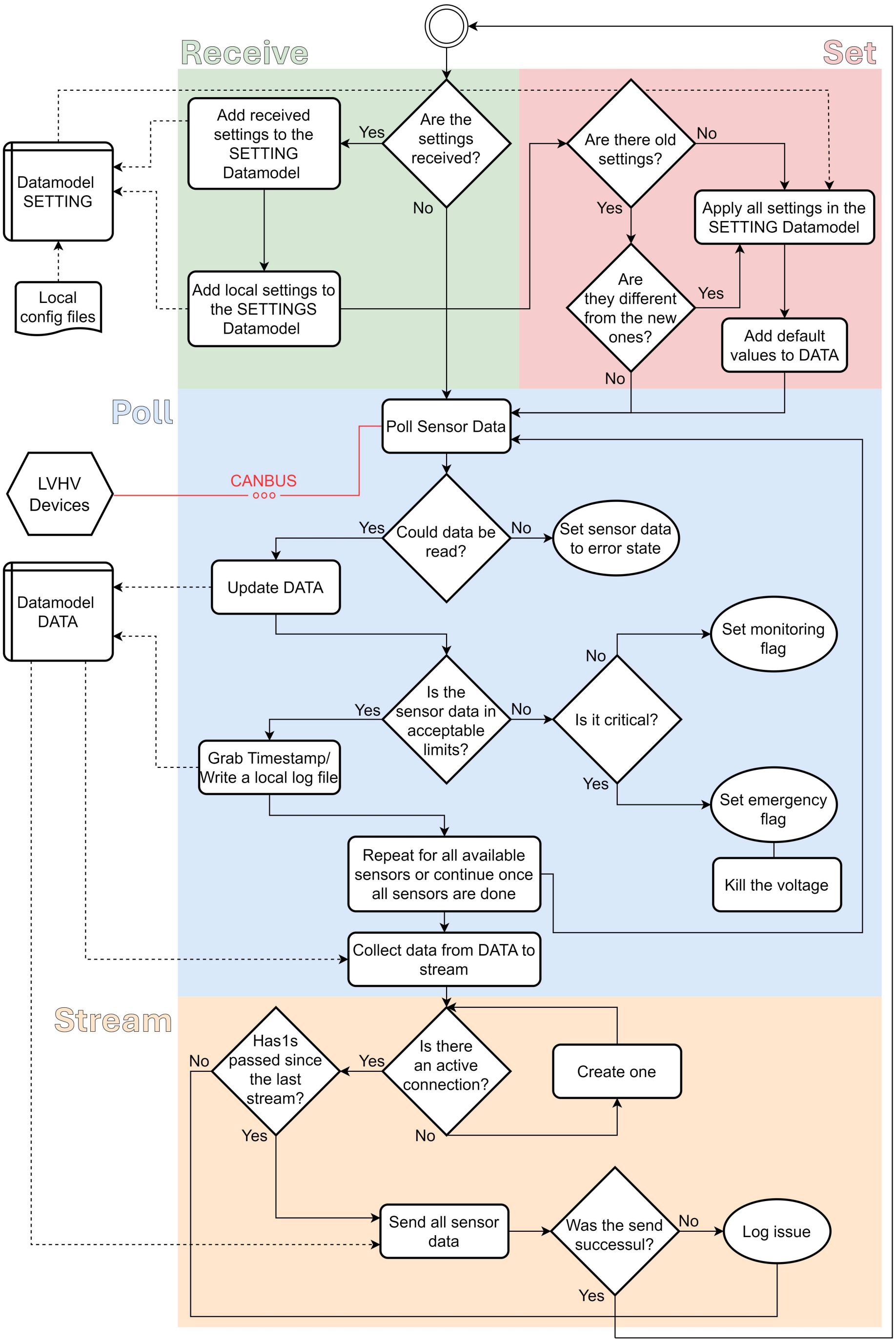

Figure 5.8: Flowchart of the general execution scheme used for the SC software. The overall structure is divided into four parts: "Receive" (green), "Set" (red), "Poll" (blue) and "Stream" (yellow).

the Tools very simple and focused on one type of communication but it also allows for a very easy integration of new components into the SC software. Whenever a new sensor is needed and needs to be integrated it can simply be added to the ToolChain as a new entry. A "Poll" Tool in general is the most complex out of the SC Tools. Internally it can be split into two parts: First polling which reads the data from the current component and updates the corresponding entry in the DataModel or sets it as an error state variable if the component could not be polled. The second part is a check against limits, decided for each component, as to what is good, monitor worthy or bad. If the state is determined as good the operations are continued normally. For a monitor worthy state the operations are also continued normally but a flag is sent through the monitoring systems to alert shifting personnel to monitor the relevant value for further degradation or improvement. If the state is determined as bad the system will automatically cut of the power to the surface or ramp down the HV depending on which component is failing. This course of action is especially necessary for the saltbridge as it acts as leak sensor as well as the thermistor as it is the only temperature sensor that is close to the LAPPD.

One potential issue that is connected to this emergency procedures is the possibility of a false positive. This is especially relevant for the humidity sensor as the humidity inside the UWH is strongly related to the temperature inside the housing and since the sensor is placed close to the hottest spot in the UWH the humidity sensor values increases significantly if the LAPPD is not running. A potential scenario could be the software set emergency limit preventing the power to be turned back on after an extended period without power when the temperature falls and the humidity goes above a certain level. To counter this the humidity sensor is the only sensor with a temperature dependent limit for emergencies. Figure 5.9 on the left hand side shows

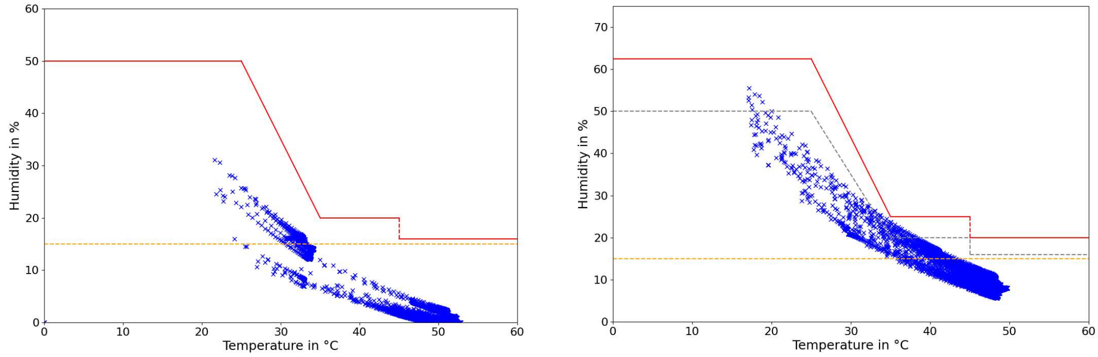

Figure 5.9: Diagram of the humidity vs the temperature for the sensor on the LVHV for LAPPD40 during different time periods. The left hand side shows sensor data taken over a period of 5 months right after the deployment and the right hand side shows sensor data taken over a period of 9.5 months starting roughly 8 months after the deployment. The orange lines show the lower warning limit and the red lines indicate the respective emergency limit for the humidity sensor to trigger an emergency shutdown. The emergency limit from the left hand side plot is also shown in the right hand side plot as grey dashed line.

the humidity against temperature plot for the respective sensor mounted on the LVHV. The data was accumulated over the first 5 months after the deployment of LAPPD40 to determine suitable long term limits. The dashed orange line is the lower level limit with a fixed value of 15 % humidity which sets a monitoring worthy flag. The solid red line is the higher level limit which would indicate an emergency. The way it was chosen is due to experiences with the sensor over the first few days as well as the data. The limit in general can be separated into

four parts which from left to right are: A constant very high limit which is mostly covering temperatures below 25 °C and is used for situations where the whole UWH had enough time to cool down significantly. An example for this would be a longer shutdown period without power which would cause the temperature to go down and thus increase the humidity. To account for a potentially very high humidity present only during the startup phase until the heating starts the limit is set very high but still below potentially dangerous levels. The second part is a linear curve that limits the humidity for temperatures between 25 °C and 35 °C down to 20 %. The third part is a step with a constant value before the forth part which limits the humidity for temperatures higher then 45 °C to a value very close to the warning limit as the humidity is quickly going towards 0 %. The step between 35 °C and 45 °C has been added due to the experiences during the deployment and the days after. In cases where the LAPPD is restarted after period of running the humidity may spike without the temperature adjusting fast enough. To account for this and prevent a shutdown of the system due to a false positive the limit has been set to a constant and higher value than the linear curve would have given.
Figure 5.9 on the right hand side shows the same type of data as before but taken for LAPPD40 about 8 months later and for roughly twice the time period. The orange line is still the same as before and the red line now shows an updated limit that was used to run the LAPPD during this period. Additionally the grey dashed line shows the previously chosen limit from figure 5.9 on the left hand side. As immediately obvious the limits no longer can constrain the humidity as necessary as the limit had to be updated to continue running. A reason for this is that over the long period of time the LAPPD has been deployed the entire UWH slowly had an increase in the overall base humidity level. This is especially visible for the lower temperatures mostly dominated by shutdown periods increasing the humidity but also for the higher temperatures where the humidity is now significantly higher than before, when it used to drop to roughly 0 %. What can be taken from this plot is also that the limit might have to be adjusted again as the linear curve is no longer matching the data as well as before. This is especially visible for the temperatures around 35 °C where the humidity almost reaches the limit.

Slow control data

After deployment and commissioning of the LAPPD-SC system as well as the implementation of limits for emergencies as discussed in the software sub-chapter the monitoring was able to quickly acquire a large set of environmental sensor data. Since the SC is integrated into the ANNIE main monitoring systems the data is first passed to the online monitoring systems that always shows the currently read values as well as a time evolution of the parameters. After passing through the main monitoring systems the data is then stored in ".root" files for further offline analysis. Afterwards the data can be analysed for unexpected behaviour otherwise missed or to get a summarizing overview plot of the sensors alone or in correlation with other sensors. Such examples can be seen in the plots of figure 5.10 for LAPPD63. The left hand side plot shows the temperature and humidity of the combined sensor and the right hand side shows the temperature of the temperature and humidity sensor as well as the temperature from the converted thermistor values over a period of 7 months. Below the main plot are the states of both LV and HV as they are the main drivers for the temperature inside the UWH and also represent the overall power state for the underwater systems. The blue values represent the HV while the red values represent the LV. Both can take the values of $\pm 1, 0$ as described in table 5.4. With this the sensor values can always be read respective to the active components in the UWH. Both plots show a large amount of spikes throughout the time period where the sensor values change drastically but these spikes can always be assigned to a corresponding switch in either the HV and/or LV state, indicating that the system was turned off for a short period of time. An exception to this single spike type is the block like behaviour towards the end of the

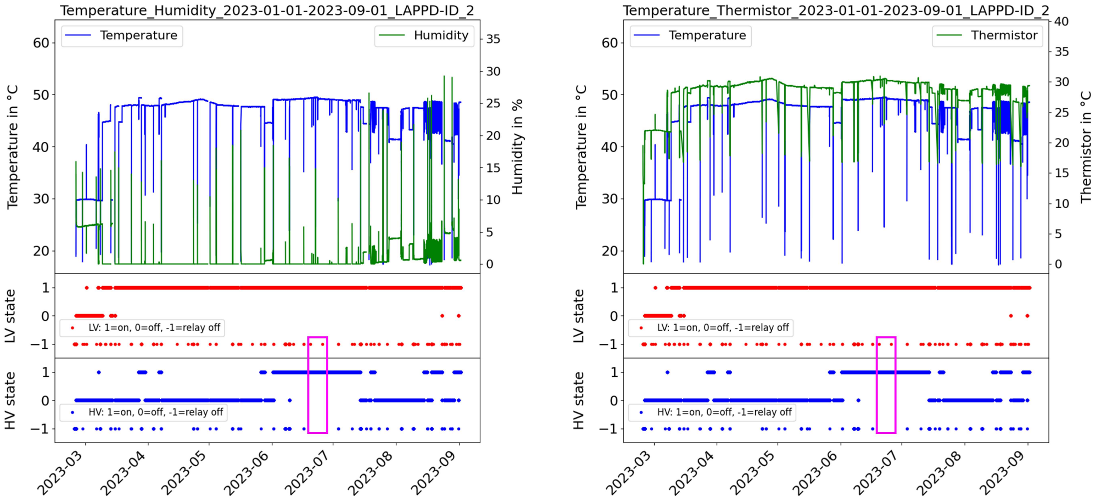

Figure 5.10: LAPPD63-SC offline analysis plots taken over a period of 7 months. The left hand side plot shows the time evolution of the temperature and humidity of the combined sensor. The right hand side plot shows the time evolution of the temperature of the temperature and humidity sensor as well as the temperature from the converted thermistor values. The upper plots show the sensor data while the lower plots show the state of the HV and LV components as described in table 5.4. Marked is also an unexpected discrepancy in the LV and HV states.

time period. In this case the system was turned on and off in quick succession, not allowing the values to adjust before returning to normal, as also indicated by the more frequent -1 states of the HV/LV. Without these shutdown periods both the temperature as well as the humidity stay relatively stable.

Table 5.4: Description of the power states used in the SC monitoring.

State value	Description
-1	Power disabled by RPi relay on the surface. Full UWH without power.
0	Power from RPi to the LVHV, but HV/LV disabled.
1	Power from RPi to the LVHV and HV/LV active. (For the HV this only describes the state of the HV block not the applied voltage.)

Another use for these kinds of plots is to check for weird behaviour. In this case the LV state shows a -1 state around July 2023 while the HV does not (as marked in the plot). This is a clear indicator that the power has been cut before the read of the LV state which could then report its off state. The HV Tool, which executes before the LV Tool, is in this case still reporting an active state and a mix of power states is reported. This and similar behaviour is expected to happen as it is only an issue of the execution sequence of the software, but has to be considered while looking for unexpected behaviour in the SC data.

The right hand side plot in figure 5.10 shows the thermistor values converted to a temperature as well as the temperature of the temperature and humidity sensor again. The thermistor has an overall lower temperature than the temperature of the temperature and humidity sensor but behaves the same otherwise. This is due to the fact that the thermistor is located between the LVHV and LAPPD and is thus below the LVHV, the main source of heat due to the LV module.

Since the LAPPD is located below the thermistor and any heat produced by the ACDC boards mounted on the LAPPD will move upwards past the thermistor, the temperature read by the thermistor can be read as the upper limit of what the LAPPDs temperature is. With an average thermistor temperature of around 25 °C the LAPPD is in a good range for operation and far off of a dangerous level of heat.

5.3.2 Data acquisition

The second software interface developed as part of this thesis is the Data Acquisition for the digitization of the LAPPD signals. It is responsible for handling all DAQ related devices which includes the data acquisition itself but also the configuration of the related hardware. The following paragraphs will describe this hardware and the software of the DAQ systems in more detail as well as show requirements for the readout speed and potential upgrades to the interface.

Hardware Setup

The hardware of the DAQ system is made up of four components: The LAPPD itself, the ACDC boards, the ACC and the DAQ-RPi running the DAQ software. While the Triggerboard is physically part of the DAQ system it is controlled as part of the SC system and as such is included with the SC components. Figures 5.2 and 5.3 show the components in the deployment ready UWH. The ACDC boards are directly mounted onto the LAPPD via an analogue pickup board and are responsible for the digitization of the LAPPD signals as close to the detector as possible. Each ACDC is capable of digitizing 30 connected channels (of which 28 are for the LAPPD, one for the trigger signal and one is not used) and is connected to the surface via a RJ45 cable which is routed through the LVHV board to the underwater cables. On the surface the cables connect to the ACC which acts as a hub for up to 8 ACDC boards and collects their data as well as distributes all relevant configurations to the ACDC boards. The ACC is also responsible for distributing a disciplined incoming 125 MHz clock signal to all connected ACDC boards as an equally disciplined 40 MHz clock signal. This 40 MHz clock signal is then multiplied by the ACDC boards FPGA into a 320 MHz clock used for timestamping events. Two additional signals that are distributed as a multiplexed signal are a Pulse per Second (PPS) signal and a beam trigger in this context called Beamgate. The former is a GPS disciplined signal that is periodically sent through the ACC to all ACDC boards. Counter intuitive the PPS signal is not necessarily set to 1 s but can also be set to integer multiples of 1 s. The latter of the multiplexed signals is the Beamgate signal which is an external signal sent by the BNB about 7.5 μs before a neutrino beam spill (see chapter 4.1) and can thus be used as part of the trigger condition. To reduce unnecessary data being taken the overall mode of operation is to only enable the ACDC boards for data taking if the Beamgate is high. If it is not the ACDC boards will continuously produce PPS frames (16 words, 16 bit each) which are triggered by the disciplined PPS signal and contain timing information about said signal as timestamps in form of the 320 MHz clock count. To not flood the system with these PPS frames the PPS is multiplied to 10 s. If the Beamgate goes high the ACDC boards switch modes and prevent PPS frames from being produced and instead allow the digitization of LAPPD data. If the Triggerboard detects a summed charge exceeding the threshold set by the SC the self-trigger of the PSEC4 ASICs starts the digitization. The data is then put into a data frame (7795 words, 16 bit each) by the ACDC board and sent to the ACCs Universal Asynchronous Receiver Transmitter (UART) buffer for the respective ACDC connection. Once the UART buffers are filled with data the ACDC boards are locked from digitising new data until the respective buffers are cleared.

To transfer the available data, independent of its type, the ACC is connected to the DAQ-RPi via an USB connection. The DAQ-RPi is running the actual DAQ software and is acting as an intermediate device between the ACC and the main ANNIE DAQ.

Software

The software developed for the DAQ system is designed to read data from the ACC via an USB interface and transfer the data to the main ANNIE DAQ via Ethernet. Additionally it is responsible for configuring the ACC and in turn the ACDC boards. The software is based on the same framework, ToolDAQ (see chapter 4.4), which in this case acts not as an independent system, as the SC does, but requires the external communication with a database and the main DAQ to function. A schematic flowchart for the DAQ software can be seen in figure 5.11.
The ToolChain in this case has been split into six Tools: "PGStarter" (purple) which connects to the database containing all settings used for the LAPPD to function properly and as they are available in a database they are used globally for all LAPPDs. The next Tool "RunControl" (green) is responsible for setting the software into either a "Run Start" or "Run End" mode and grab the corresponding settings made available by the database. The other four Tools are fundamentally similar to the ones used by the SC software: "Reveive" (grey) which in this case applies the settings from the database to the corresponding DataModel, "SetupBoards" (red) which sends the settings to the ACC and in turn the ACDC boards and in case of a "RunControl" change re-applies the settings. It is also responsible for resetting the system in case of erroneous behaviour without the need of external input. The "DataRead" (blue) Tool as the name suggests is responsible for the actual data read from the ACC and has to follow a very specific sequence to acquire data. This sequence will be described in a later paragraph while discussing the requirements for the data readout speed. The "Stream" Tool (orange) is the last Tool in the ToolChain and is responsible for sending the data to the main ANNIE DAQ with the additional caveat of not immediately sending the data but rather buffering the data in a queue and sending it only if the main DAQ is ready to accept new data. This is especially important as the main DAQ will also receive data from the other subsystems and data might be lost otherwise. What is important to note is that not only the available data frame will be sent but a set of header data will be sent as well. Everything that will be sent is stored in a "PsecData" DataModel which then will be the object sent. In this case the DataModel was designed to also include all necessary communication procedures which allows it to be used by the sending as well as the receiving side without the need to write a new procedure for the receiving end on the main DAQ. A version number on both ends makes sure that no mismatch can happen. Everything sent in such a "PsecData" DataModel can be seen in table 5.5.

5.3.3 Data frames

As introduced in the previous paragraphs, there are two kinds of frames available for the LAPPD readout, a data frame produced during a Beamgate high period (this includes the metadata) and a PPS frame produced during a Beamgate low period. The total length of a data frame is 7795 words, 16 bit each, of which 7680 words are produced by collecting the digitised data from all 30 channels on an ACDC board. Of the remaining words, 70 words are metadata and 45 words are identifier words to mark the beginning/end of the data frame, PSEC4 chip data, etc.. The 70 words of the metadata are combined from internal metadata from the respective PSEC4 chips themselves as well as a set of global metadata. This includes for example the event timestamp generated by the 320 MHz clock which is stored as a 64 bit clock counter. As single words can only contain 16 bit the timestamp is split into four parts and distributed over four words. The full structure of the data frame can be seen in table B.1 in appendix B. As for the metadata the

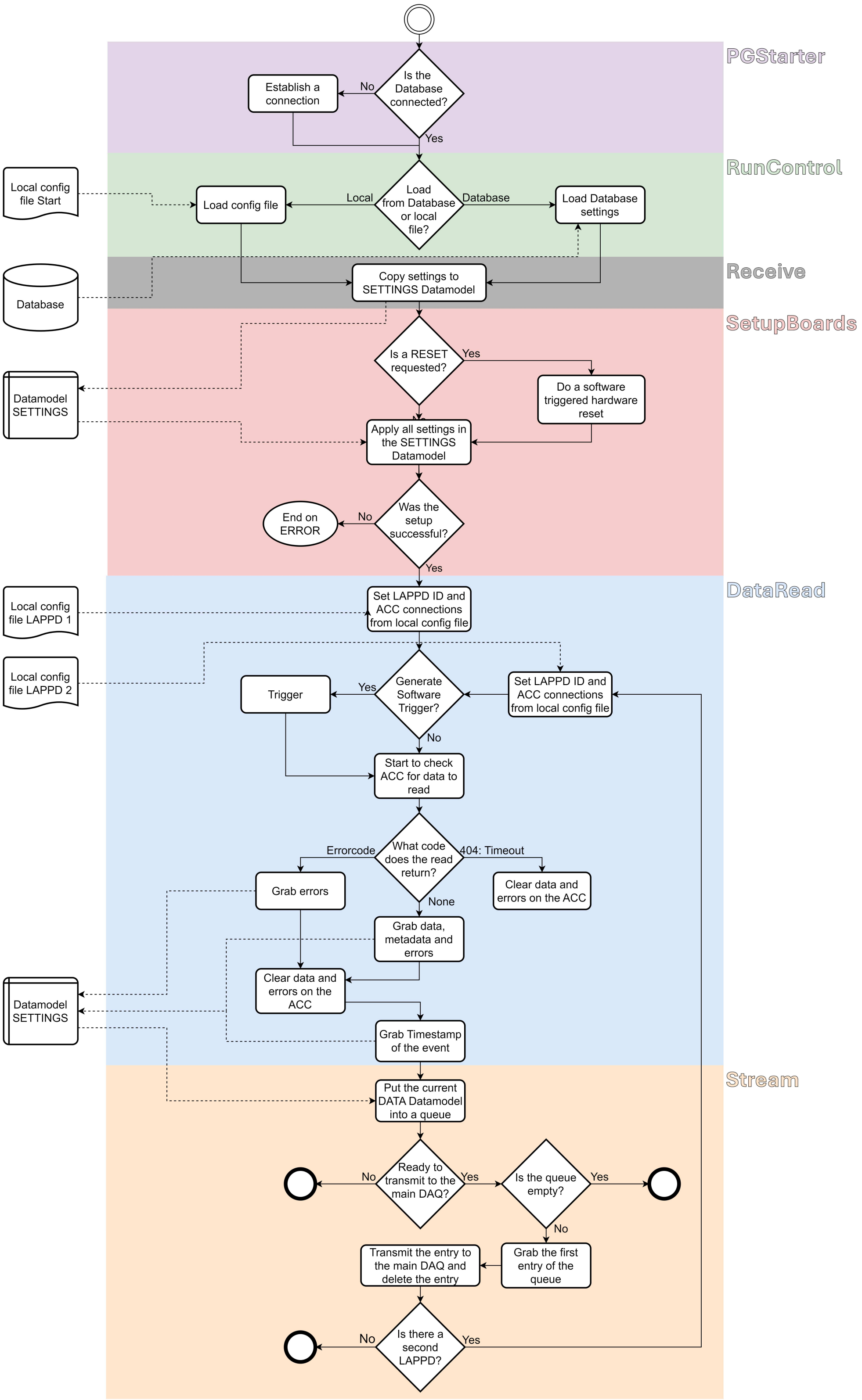

Figure 5.11: Flowchart of the general execution scheme used for the DAQ software. The overall structure is divided into six parts: "PGStarter" (violet), "RunControl" (green), "Receive" (grey), "SetupBoards" (red), "DataRead" (blue) and "Stream" (orange).

Table 5.5: PsecData object structure as used for the LAPPD data stream.

Variable name	Type	Description
VersionNumber	unsigned int	Current version number
LAPPD_ID	unsigned int	LAPPD identifier
UNIX Timestamp	string	Timestamp in CST and ms since epoch
BoardIndex	vector<int>	Entries specify the read ACDC boards and their physical connection to the ACC
AccInfoFrame	vector<unsigned short>	Contains the ACC info frame
RawWaveform	vector<unsigned short>	Contains up to 2 data frames (see B.1) Metadata is included in this vector
errorcodes	vector<unsigned int>	Error codes produced for this read cycle
FailedReadCounter	int	Accumulated failed reads

structure can be seen in tables B.3-B.5 and for it to be in this format the metadata has to be first parsed to extract the relevant information.

The PPS frame on the other hand is a 16 word long frame with each word being 16 bit as well. The frame is produced by the ACDC board in continuos time intervals set by the software as an integer multiple of 1 s. The frame is then filled with the current timestamp of the 320 MHz clock, again split into four parts to accommodate the 64 bit of the timestamp. Additionally a continuos counter and a serial number for successful PPS frames are added as well to allow for serial reconstruction of the PPS frames and check for missing frames. The full structure of the PPS frame can be seen in table B.2. The PPS frame becomes important when taking into account that every LAPPD is its own system that functions independently from the outside world. Up to four LAPPDs can be easily synchronized within one ACC due to the shared clock signal. Synchronizing LAPPDs on different ACCs and other subsystems with each other is more difficult. To successfully synchronize them the GPS disciplined PPS signal which is present on all systems can be used.

5.3.4 Data readout speed requirements

Determining the necessary requirements for the readout speed and accompanying data rate is crucial for the LAPPD DAQ system and ANNIE in general. The overall goal is to be faster with a full LAPPD readout than the repetition rate of the BNB which is around 5 to 7 Hz [46]. The main limiting factors of the data readout are the dead time of the PSEC4 ASICs, the transfer time from ACDC board to ACC, the transfer time from ACC to RPi and lastly the overall runtime of the software. The dead time for each of the five PSEC4 ASIC is around 30 μs [63] and comparably small to the other factors. The transfer time from ACDC to ACC is by far the largest contribution due to its maximum transfer speed of around 6 Mbit/s which in turn results in a dead time of 22 ms for one data frame. Since the firmware has been adapted to be synchronous additional ACDC boards connected to the same ACC only add minimal overhead to the overall dead time. The transfer time from ACC to the RPi is fixed by the USBs 48 Mbit/s transfer speed limit and adds around 2.5 ms to the dead time. This results in a dead time of:

$$\text{Dead time}\,[\text{ms}] = 5\cdot 0.03\,\text{ms} + 22\,\text{ms} + 2.5\,\text{ms} + \text{Overhead} \approx 26\,\text{ms} \quad . \tag{5.13}$$

From this we can calculate the maximum LAPPD event recording rate to be around 30 Hz for one ACDC which is far above the necessary data rate of 5 to 7 Hz. Scaled to one LAPPD which has 2 ACDC boards the data rate should only marginally decrease as the only affected parameter is the transfer from ACC to RPi. In reality the data rate is more impacted than originally expected due to the transfer from ACDC board to ACC not starting at the same time which adds additional dead time. Another reason is the way the software acquires the data and the additional time the software needs to handle more ACDCs. Since the software is written in ToolDAQ the readout of additional ACDCs can be easily added by simply duplicating the "DataRead" and "Stream" Tool to run twice in series. This of course also increases the runtime of the software. As mentioned during the software section the acquisition of data from the ACC is done in a very specific sequence. This sequence is nested within the "DataRead" Tool which is executed once for each LAPPD separately. The sequence starts by allowing the ACDC board to transfer its data to the ACC which usually only has to be done once at the start of the data taking as it might have been disabled during setup. The next step is to check the buffers on the ACC for the amount of data words. A combination of the correct amount of words (in this case 16 or 7795) and a "transfer done" bit being high adds the corresponding ACDC board to the list of ready to be read ACDC boards. This is done in series for all related ACDC boards and once the ACDC boards belonging to the currently handled LAPPD are in the list the data readout will start. The other ACDC boards will be ignored until the next LAPPD is handled. This check is done in a loop until either a readout is ready to start or until 500 ms have passed. In the latter scenario the software will exit the "DataRead" Tool with a timeout and continue with the next LAPPD. This is done to keep the ToolChain responsive and prevent it from being locked in a loop for too long. But the downside of this is that events that happen close to the end of the 500 ms will be skipped until the next loop adding additional dead time. Since an LAPPD always has two ACDC boards to read the data for both will be appended into one large data frame which will be sent. A successful read then clears the buffers, opening them up for the new data. With these reasons in mind it is decided to not use more than two LAPPDs per ACC to keep the LAPPD event recording rate above the necessary 5 to 7 Hz. In test runs a rate of around $25-30$ Hz for two ACDC boards could be reached.

5.3.5 Change from USB to Ethernet interface

In the scope of this thesis a software interface capable of utilizing an Ethernet interface to communicate with the ACC has been developed and tested in a laboratory environment. Once adapted for use in the main ANNIE DAQ it is ready for deployment. This change is meant to further improve upon the LAPPD DAQ system by switching from the USB interface which handles the communication between the ACC and the RPi to an Ethernet interface. Since the ACC is technically capable of using Ethernet and is simply missing a corresponding software and firmware a switch would be possible. Overall this would have multiple advantages with the first and most obvious being the transfer rate being much faster (up to 1 GBit/s [66]) than for the USB interface. This would make the time required to transfer data from the ACC, which has to be done in series for multiple ACDCs, negligible. Another advantage would be the increased stability of the system as the USB interface can become rather unstable over time and once the connection is lost it cannot be recovered without a restart of the ACC which requires on-site presence. A switch to an Ethernet interface would circumvent this behaviour. The most important improvement of the system would be the ability to get rid of the DAQ-RPi as an intermediate step between the ACC and the main ANNIE DAQ. The ACC would then be able to directly connect to the main DAQ via Ethernet and the software could be directly integrated into the main systems to stream the data along. As RPis are generally unstable depending on their age this change will also get rid of an additional issue. With the software running directly on the main DAQ the data could be directly integrated into the main data stream and be processed in the same way as the data from the other subsystems allowing for a more direct comparison of the data as it would not be first queued on the RPi.

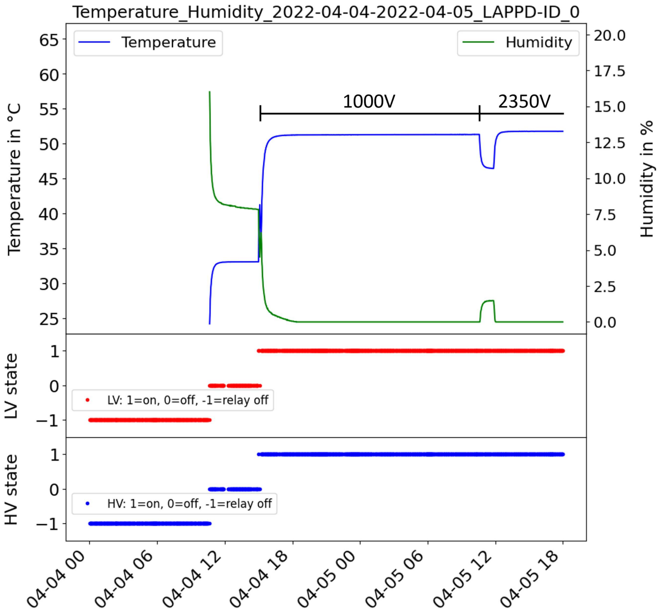

Figure 5.12: Environmental data taken during the deployment of LAPPD40. The data shows the temperature (blue, top) and humidity (green) in the UWH as well as the states of the HV (blue, bottom) and LV (red). The adaptation to the operational conditions can be seen as time progresses. The actual start of the system is around 12 pm where both temperature and humidity are starting.

5.4 Deployment and beam data of the first LAPPD

At the end of March 2022 the first deployment of an LAPPD, called LAPPD40, took place after thorough characterisation and preparation as described in chapter 5.2. The deployment was done by a team of collaborators on-site (from Fermilab, UC Davis and Iowa State). The software interfaces developed for this thesis, introduced in chapter 5.3, were remotely deployed at the same time. Afterwards SC monitoring (see chapter 5.3.1) started immediately and beam data taking with the all systems integrated and the developed DAQ interface (see chapter 5.3.2) started in May 2022. Running for about 2 months until the end of the beam year the first set of LAPPD data was recorded.

This chapter will first show the environmental conditions of LAPPD40 shortly after the deployment by analysing the SC data. Afterwards corrections necessary for the data to be usable will be explained, followed by a consistency check of the PPS signal. Lastly the data taken over the 2 month period will be analysed to see if LAPPD signals can be correlated with the neutrino beam.

5.4.1 Environmental data of the first deployment

The environmental data taken shortly after the deployment of LAPPD40 can be seen in figure 5.12. The data shows the temperature and humidity in the UWH as well as the states of the HV and LV after the deployment where the system was tested and started for the first time. Three phases can be seen: The first one being a period of roughly 12 hours in which the system was turned off. Temperature and humidity are not yet recorded and both HV and LV report the -1 state. In the second phase the system was turned on but left in a passive state where power makes it into the UWH but HV/LV are not yet enabled. What can be seen is that in this time frame the temperature and humidity are recorded. Due to the minimal heat being produced in this state the temperature rises to around 30 °C and the humidity drops from almost 60% to around 40%. The last phase starts at the point in time, around 12 pm on the 4th April, the system was turned on with both HV and LV enabled. The humidity quickly drops to 0% due to the heat produced by the LVHV board, which heats the UWH to above 50 °C. In the first test phase the HV was ramped up to 1000 V to see if the system stays stable. This condition was then kept for about 20 hours. Afterwards the HV was ramped to its operational voltage of 2350 V. The small dip around the time the operational voltage was applied is due to the HV being ramped down to zero first before ramping it up again. This slightly lowers the temperature due to the change in HV. This state is stable throughout the rest of the time period shown and is what is considered operational conditions. As figure 5.10 shows if considering only the times the system was active, both the temperature and humidity are stable over time.

5.4.2 Metadata corrections

With the LAPPD deployed and integrated into the data stream of ANNIE the data can be analysed to see if there is an excess of events correlated to the BNB. But in order to access the data it has to first be extracted from the raw data frame which contains both data and metadata. Once separated the Metadata has to be used to correct several characteristics present for the PSEC4 chips. The first and most important correction that needs to be done is the "pedestal subtraction". What this means is that each sample of each channel of every individual PSEC4 chip has an initial characteristic value that can be set as baseline. But due to manufacturing tolerances this value can significantly differ from what was originally set and in turn increases the noise of a waveform immensely. To counter this internal uncertainty a data set has to be taken under dark conditions. This dark data can then be used to create a pedestal correction file by taking the mean of the Gaussian distribution created for each ADC sample. Each sample is then subtracted with the corresponding sample of the pedestal correction file. Figure 5.13 shows the result of a correct and an incorrect pedestal subtraction. Since the pedestal differences are a hardware property, a pedestal correction file can only be used on the ACDC board that was responsible for acquiring the data to create the pedestal correction file. The data in the figure on the left hand side has been corrected with a correct assignment between pedestal correction file and ACDC board while the data on the right hand side has been corrected with a wrong assignment. The difference in the noise is quickly visible with the left hand side having an RMS of 8.16 ADC counts while the right hand side has an RMS of 80.5 ADC counts which corresponds to an RMS noise of roughly 2.5 mV and 25 mV respectively. Two additional aspects of this correction can also be seen in figure 5.13. The first being the obvious spike in the waveforms with the incorrect assignment which is completely absent in the waveforms with the correct assignment. Compared with the uncorrected waveforms which can be seen in appendix C in figure C.1 an incorrect assignment between ACDC board and pedestal correction file will reproduce and mirror features like the spike.

The second aspect is the presence of actual LAPPD pulses which can clearly be seen on the left hand side but are completely lost in the noise on the right hand side. Once the data is "pedestal subtracted" it is still necessary to do an overall baseline subtraction by determining the mean of the Gaussian distribution all samples of a waveform create. Since the "pedestal subtraction" only accounts for the internal hardware differences of the PSEC4 chips it is not necessarily a correction for the baseline of the waveform.

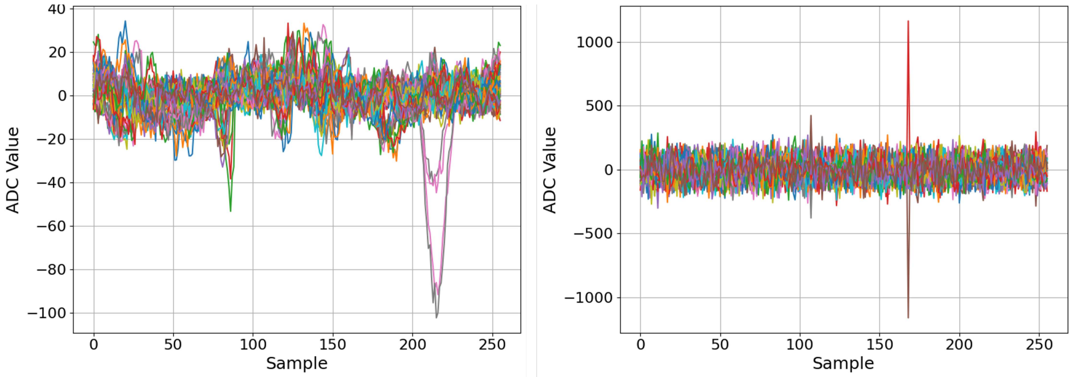

Figure 5.13: Comparison of a correct and an incorrect pedestal subtraction for all 56 channels. The left hand side shows the result of a correct assignment between pedestal correction file and ACDC board while the right hand side shows the result of an incorrect assignment. The difference in the noise is clearly visible with a magnitude difference. The plots show all 256 samples of the digitizer which at a sampling rate of 10 Gs/s correspond to 25.6 ns.

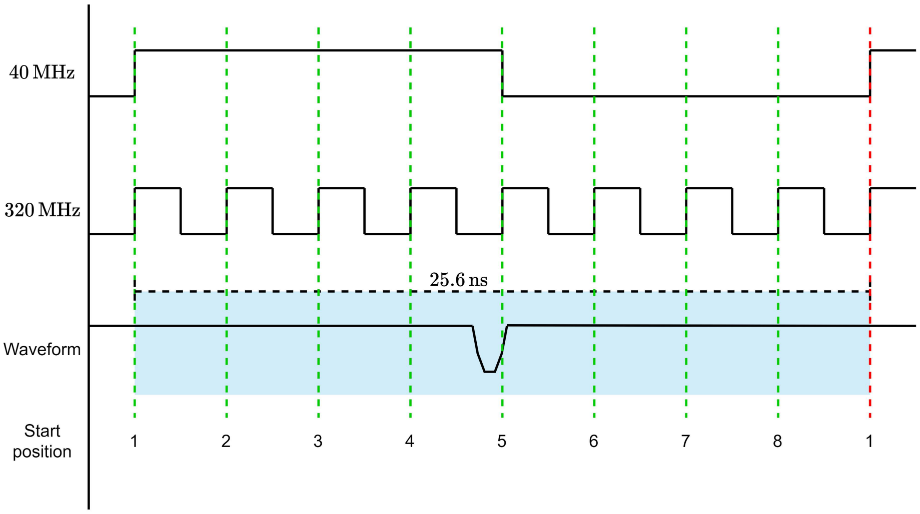

Figure 5.14: Clock diagram for the ACDC board: Shown are both a 40 MHz clock cycle and eight 320 MHz clock cycles. An example waveform and the eight possible starting positions (green) given by the 320 MHz clock can be seen as well.

Another correction that has to be done before the data can be properly used is to correct the order of the samples as they appear in the raw waveform. Since the PSEC4 chip uses a Switched Capacitor Array (SCA) that is timed by a Voltage Controlled Delay Line (VCDL) signal locked onto the 40 MHz clock signal, the start of the digitized waveform is not always in the same position. The correct start of the waveform is given by the capacitor which is currently in respect to the VCDL. Considering the 40 MHz clock input to the PSEC4 chip and the waveform which is timestamped by a multiplied clock with 320 MHz the start of the waveform can be in one of eight 320 MHz clock cycles that make up the 40 MHz clock. This can be seen in figure 5.14 where both the 40 MHz clock and the 320 MHz clock are shown together with an example waveform and the eight possible starting positions of the waveform. To find the correct starting

position of the waveform the metadata can be used. The metadata contains a 16 bit word of which the last 3 bits are pointing the the 320 MHz clock cycle the waveform starts in (see the starting positions in figure 5.14). This correction has to be done for every event and each ACDC board individually but is the same for all PSEC4 chips on the same ACDC board as they get the same clock signal. This procedure can be seen in figure 5.15, where the left hand side shows the waveforms before the correction and the right hand side shows the waveforms after the correction. An obvious difference is the alignment of the trigger signals which on the left hand side are not aligned properly and even cut off at the end. After the correction is done a small time difference between the trigger signals still remains due to internal delays within the ACC and ACDC boards. In most cases this will not affect the analysis of the LAPPD event data since a strip line is always read out by the same ACDC board and as such the time difference of the trigger signals has no influence. Only if strip lines on different ACDC boards will be put on an absolute timescale the difference needs to be corrected.
With these corrections the basic steps to make the data usable have been shown and the LAPPD beam data can be analysed.

Bi

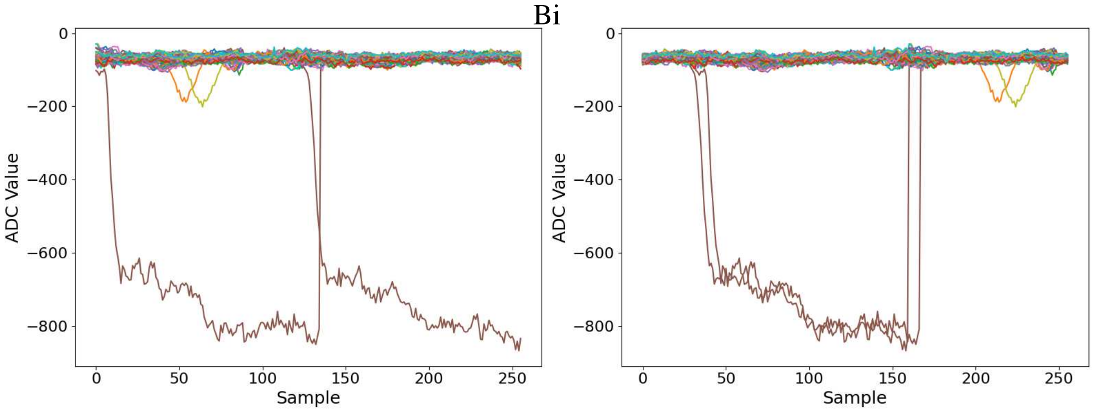

Figure 5.15: Comparison of waveforms before and after the timing bit correction, done for all waveforms and two trigger signals. The left hand side shows the waveforms before the correction and the right hand side shows the waveforms after the correction. The trigger signals (brown) as well as some pulses (green, orange) in the waveform can be seen.

5.4.3 PPS consistency test

In regards to integrating the LAPPDs with the other ANNIE subsystems the PPS is a crucial aspect which has to be discussed. As already mentioned an LAPPD is its own closed off system together with their ACDC boards and the ACC they are connected to. Except the PPS the only signal from the outside world is the clock distributed among the systems. While LAPPDs connected to the same ACC can be synchronized with each other, the synchronization with other ACCs or the other subsystems is more difficult. For this sake the PPS which is produced by the Central Trigger Card (CTC) is vital for the alignment with the other subsystems. As such it is important to check for the stability of this PPS signal. Figure 5.16 shows the timestamps of the PPS frames as recorded by the LAPPD DAQ system. The left hand side plot displays the time difference between consecutive PPS timestamps. The data shows a clear excess of events with a time difference of 10 s which corresponds to the PPS signal which is set to a 10 s interval. A particular behaviour where the PPS signal can appear at 20 s can be seen as well. This can happen if the PPS signal falls into a time frame where the Beamgate is high, for which the LAPPD data has the higher priority. The plot on the right hand side shows the difference from the 10 s bin with a finer binning of 1 μs which shows a distribution around $-52.3\,\mu$s with a standard deviation of 5.8 μs. This indicates that in addition to a general clock offset the clock seems to be drifting around its offset which has to be taken into account. Since the alignment with the other systems like the PMTs or the MRD does not need this level of precision, as it is aligned against other PPS signals, it is not relevant for the PPS consistency. Overall this is a clear indication that the system functions as it is intended. The PPS is very stable as indicated by primary 10 s bin on the left hand side plot.

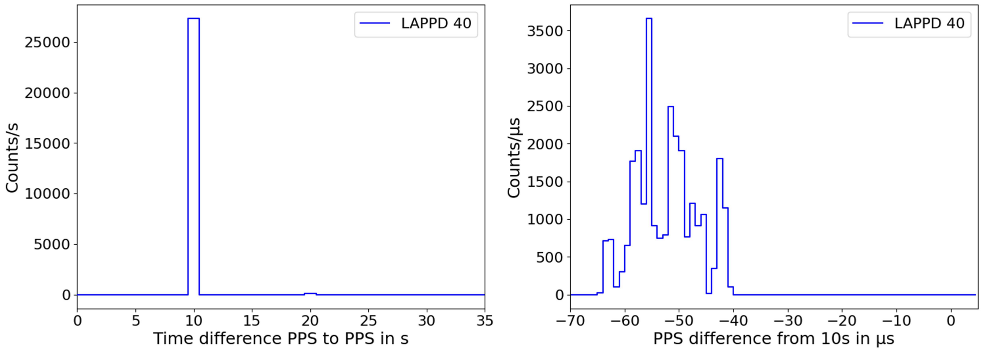

Figure 5.16: PPS consistency for LAPPD40 during its first two months of runtime. The left hand side shows the time difference between consecutive PPS timestamps for a PPS setting of 10 s. The right hand side shows a 1 μs binning of the difference from the 10 s bin. An offset of $-52.3\,\mu$s can be seen with a standard deviation of 5.8 μs.

5.4.4 First Neutrino beam data

The first neutrino data was taken by LAPPD40 in 2022 and has been used as a first proof that the BNB is visible in the data. For this two independent approaches were taken. The first only takes into account the event timestamps created by the 320 MHz clock signal without actually accessing the data while the second approach uses the waveforms of the LAPPD data. Figure 5.17 on the left hand side shows the former of the two approaches. The data shows the time difference between a timestamp generated by the signal sent from the BNB which sets the Beamgate to high and the event timestamp generated from the self trigger of the PSEC4 chips. Both values can be extracted from the Metadata as 64 bit values as found in appendix B. The values are given as clock cycles based off of the 320 MHz clock signal and are converted into nanoseconds first. By then taking the time difference between the two timestamps, from BNB trigger to LAPPD event, a clear excess of events between roughly 7.5 μs and 9 μs with a FWHM of 1.625 μs can be seen. This FWHM is exactly what is expected from a BNB neutrino spill [67] and it can thus be stated that the LAPPD sees the neutrino beam.

The second approach which can be seen in figure 5.17 on the right hand side uses the data taken by the LAPPD to determine the multiplicity over the LAPPD strip lines for each event. Therefore the amount of strip lines with pulses are counted and separated into "off-beam" and "on-beam" events. The "on-beam" events are those events that are within the 1.625 μs FWHM of the BNB spill while the "off-beam" events are those events that are outside of this window. To account for the over 10 times larger "off-beam" time compared to the "on-beam" time the event rate is normalized to 1 μs. The result shows a clear increase in rate for the "on-beam" events for both low and higher multiplicities. This is a clear indication for the LAPPD seeing more light during the BNB spill then outside of it which allows for the conclusion that the LAPPD sees the neutrino beam.

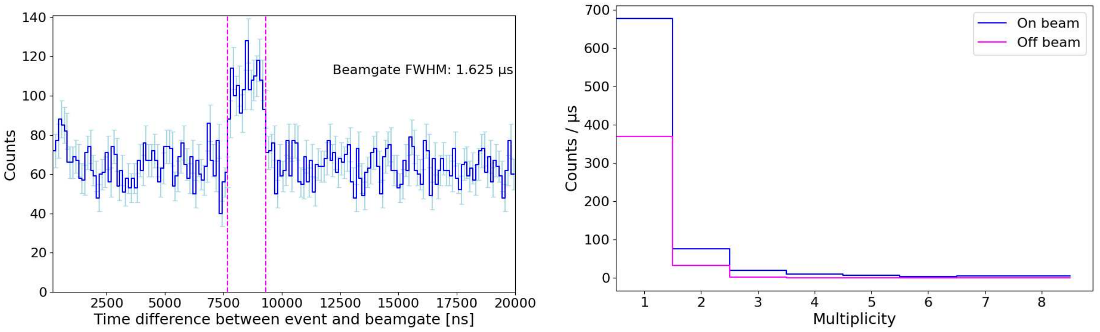

Figure 5.17: Neutrino beam data taken by LAPPD40 over its first two months of runtime. The left hand side shows the time difference between BNB trigger timestamp and LAPPD40 event timestamp. An excess of events per 125 ns between 7.5 μs and 9 μs with a FWHM of 1.625 μs is clearly visible which corresponds to a BNB spill. The right hand side shows the strip multiplicity normalized to 1 μs for "on-beam" data (blue) and "off-beam" data (magenta). A clear increase in rate for the "on-beam" data can be seen for both low and high multiplicities which is a clear indication for the LAPPD seeing neutrino beam induced events.

5.5 Beam data with three LAPPDs

From the end of February 2023 until the end of November 2023 two more LAPPDs, LAPPD63 and LAPPD64, were deployed in addition to LAPPD40. Afterwards all LAPPDs were removed for maintenance since the beam year was over and no more beam data could be taken. The deployment of the two new LAPPDs was done similar to LAPPD40 where a on-site team (from Fermilab, UC Davis and Iowa State) did the deployment while the software interface was done remotely. As part of this thesis the runtime during which three LAPPDs were deployed was analysed to show PPS consistency and the appearance of a beam structure similar to figure 5.17 on the left hand side for an LAPPD connected to a different ACC. Lastly some statistics for the three LAPPD runtime are shown.

Similar to chapter 5.4.3 the PPS consistency can be tested for all three LAPPDs. Therefore the time difference between consecutive PPS timestamps can be seen in figure 5.18 on the left hand side . The results show the same behaviour as before where most time differences are in the 10 s bin with only a small fraction being at 20 s. LAPPD40 and LAPPD63 behave mostly the same as they are connected to the same ACC and as such share the same clock and PPS signals. The slight difference that is left is due to internal delays where one ACDC board already switched Beamgate states while the other has not. LAPPD64 on the other hand is connected to a different ACC and as such behaves differently. The overall amount of PPS frames recorded differs significantly from LAPPD40/63 and time differences with 20 s or higher start appearing as well. This effect of different ACCs is also visible in figure 5.18 on the right hand side which again shows the difference from the 10 s bin with a finer binning of 1 μs. While LAPPD40/63 which are on the same ACC have the same offset of $-52.8\,\mu$s with a standard deviation of 1.95 μs, LAPPD64 has an offset of $-28.4\,\mu$s with a standard deviation of 2.1 μs. This means that

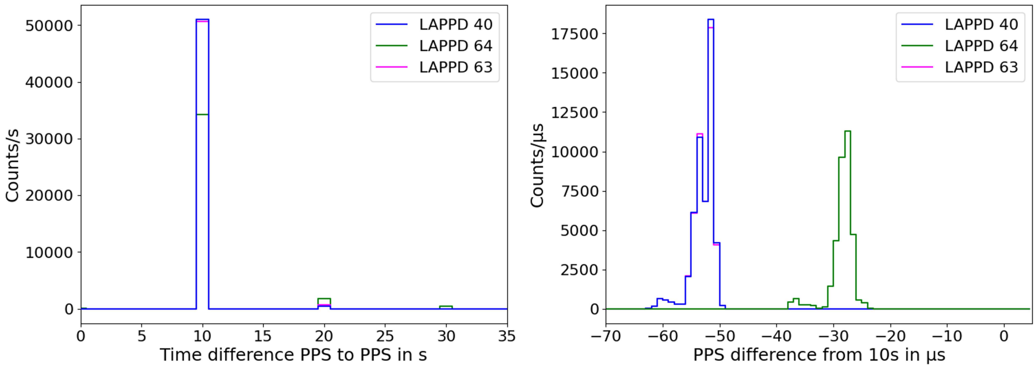

Figure 5.18: PPS consistency for LAPPD40/63/64 for the three LAPPD runtime of 8 months. The left hand side shows the time difference between consecutive PPS timestamps for a PPS setting of 10 s. The right hand side shows a 1 μs binning of the differences from the 10 s bins. An offset of 52.8 μs can be seen for LAPPD40/63 and 28.4 μs for LAPPD64.

LAPPDs connected to different ACCs behave differently in terms of their clock offset and drift. An improvement done to the clock distribution of the ACCs improved the clock drift by a factor of 2, as seen for LAPPD40.

With the result that LAPPDs connected to different ACCs behave differently it is also worthwhile to check if, in this case LAPPD64, can see events correlated to the BNB. This can be seen in figure 5.19. Similar to figure 5.17 on the left hand side the width of the "on-beam" time is 1.625 μs. As both LAPPDs show the same behaviour during a beam spill and the beam spill occurs in the same time frame it can be concluded that separate ACCs behave the same and the difference in clock offset and drift does not affect the LAPPD beam data.

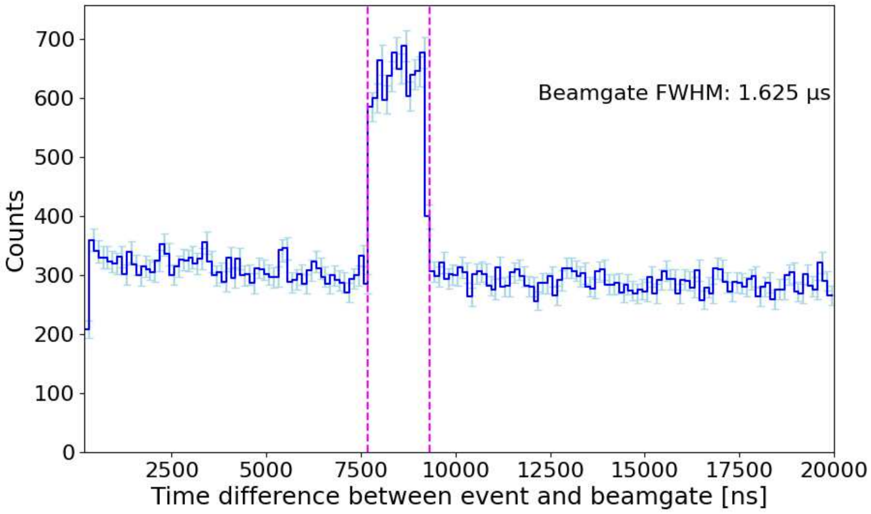

b

Figure 5.19: Time difference between BNB trigger timestamp and LAPPD64 event timestamp. An excess of events per 125 ns between 7.5 μs and 9 μs with a FWHM of 1.625 μs is clearly visible and corresponds to a BNB spill.

Next in this chapter some statistics for the three LAPPD runs are shown. This also acts as the introduction to several cuts that have to be applied to find neutrino events and it serves as an overview to the ratio between PPS frames and LAPPD data frames. An important piece of information to understand for these is the position of the LAPPDs in the ANNIE tank. As depending on the position their event rate might differ it has to be taken into account for the statistics. LAPPD40 is positioned central along the axis of the BNB looking towards the beam. LAPPD63 and 64 are positioned to left hand side of LAPPD40 and are looking towards the beam at an angle of 45°. While LAPPD63 is positioned at a higher position in the tank compared to LAPPD40, LAPPD64 is positioned at a lower position. To see how the distribution between data frames and PPS frames is allocated figure 5.20 shows the amount of data frames and PPS frames taken over a series of runs. While the amount of data frames varies significantly, as expected for a self triggering system, the amount of PPS frames is the same for all LAPPDs connected to the same ACC. This means that the PPS system is working as intended and no particular PPS frames are lost but overall LAPPD40 sees less light than LAPPD63 and 64. Once PPS frames are separated from the data frames the amount of leftover data frames can be seen in figure 5.21 as blue bars. As discussed in chapter 5.4.4 one of the first steps is to separate "on-beam" data from "off-beam" data as the "on-beam" data is the relevant data for neutrino events. The applied cut for "on-beam" and "off-beam" data can be seen in figure 5.21 as magenta hash. As shown most of the events are "off-beam" events and can be cut as indicated in figure 5.19. Considering the ratio between "off-beam" and "on-beam" time, about 7.5 % of events should be left after the Beamgate cut if a uniform distribution of events is assumed. Higher values indicate the presence of beam induced neutrino events. For LAPPD40 and LAPPD63 the amount of events left is around the expected ratio with 8.74 % and 8.50 % respectively which could indicate a bad signal to background ratio with the excess of events during the "on-beam" time being significantly lower than expected. LAPPD64 on the other hand has about twice the expected amount of leftover events with 15.51 % which makes senses considering the significantly higher overall data rate. The leftover events which now are only events that happened during a beam spill of the BNB are shown in figure 5.22 as blue bars. As also discussed in chapter 5.4.4 the strip multiplicity can be determined for events. As the result shows an increase in events with higher

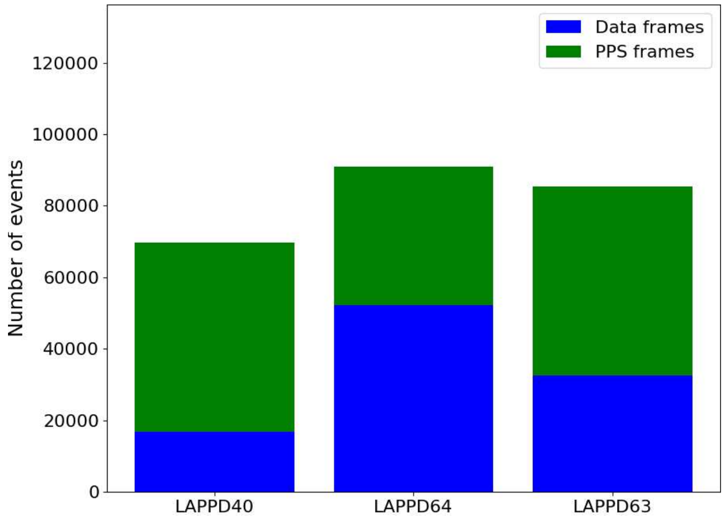

Figure 5.20: Statistics for the amount of data frames and PPS frames taken over a series of runs. The blue bar shows the amount of data frames while the green bars shows the amount of PPS frames. LAPPD40 and 63 show the same amount of PPS frames and a higher fraction of PPS compared to data frames while LAPPD64 shows the opposite.

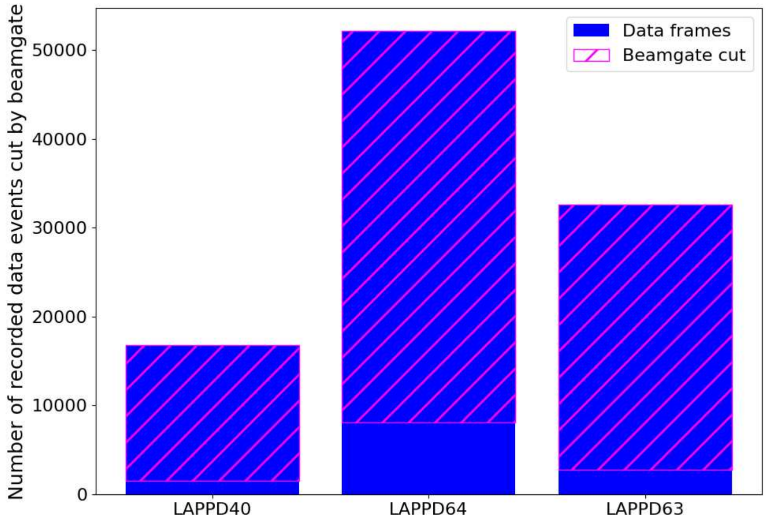

Figure 5.21: Applied Beamgate cut: The total number of events is represented by the blue bars. The events cut by the Beamgate are shown as magenta hashes over these bars, indicating the 'off-beam' events. The unmarked part of the blue bars corresponds to the 'on-beam' events. As the "on-beam" data is the relevant data for neutrino events most of the data can be cut.

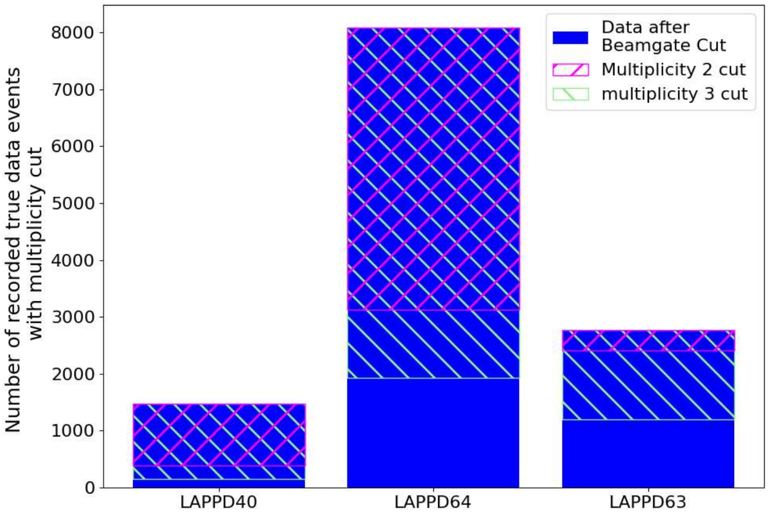

Figure 5.22: Applied multiplicity cuts on the data after the Beamgate cut: The total number of events is represented by the blue bars and indicate a multiplicity of 1. The events cut with a multiplicity of 2 are shown as magenta hashes and the events cut with a multiplicity of 3 are shown as green hashes over the blue bars.

multiplicities during a beam spill the next step could be a multiplicity cut to remove events that contain to little information. For this different multiplicity cuts, for multiplicities of 2 and 3, have been applied to all events that are leftover after the Beamgate cut. Figure 5.22 shows all events leftover after the Beamgate cut as blue bars and the multiplicity cut of 2 as magenta hash and 3 as green hash. All of these values, including all events and the split between PPS and data, and the values after the Beamgate and multiplicity cuts can be seen summarized in table 5.6.

Table 5.6: Table for the amount of events, PPS and data, both combined and separate, after the Beamgate cut and the multiplicity cuts. Multiplicities of 2 and 3 are shown while the uncut data corresponds to a multiplicity of 1.

	LAPPD40	LAPPD64	LAPPD63
All Data	69640	90842	85174
PPS	52859	38729	52859
Data	16781	52113	32585
After Beamgate	1467	8081	2771
After multiplicity 2	392	3124	2414
After multiplicity 3	158	1929	1193

The last part of this chapter will show some event displays for LAPPD40 and LAPPD63. In figure 5.23 an exemplary event display is shown for LAPPD40 oriented as it is in the ANNIE tank. The event displays use data after the Beamgate cut but without a multiplicity cut. The event display shows normalized integrated charge for each strip of the LAPPD at the reconstructed position in physical dimensions. The reconstruction of events was done as described in chapter 3.3.2. LAPPD40 sits central to the BNB axis and what can be seen is a distribution that is well distributed over the entire LAPPD surface which is expected for a central detector. Figure 5.24 shows a similar event display for LAPPD63. What can be seen is that events are mostly concentrated on the right hand side. In particular, a cluster in the top right corner and a cluster in the bottom right corner are visible. The very strong concentration of charge on the end of a single strip line could be an indication for a faulty ACDC board or a defective strip line.

It can be concluded that the deployed LAPPDs are working as intended and are capable of detecting the light produced by neutrino interactions induced by the BNB and that the data is consistent between the LAPPDs. The chapter also displays the capabilities of LAPPDs as their own 2D detector system with event displays showing the data of the beam runtime.

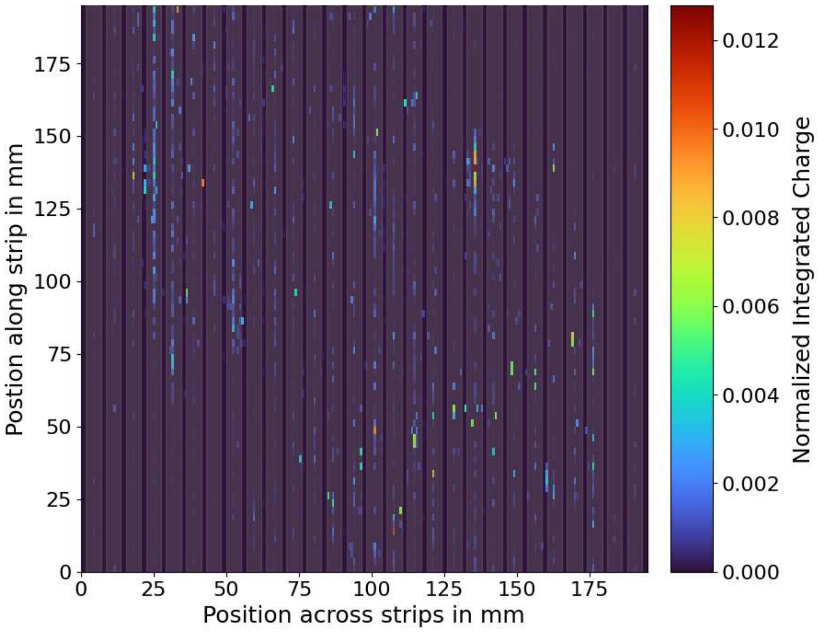

Figure 5.23: Integrated charge distribution for all events after the Beamgate cut and no multiplicity cut for LAPPD40. The charge is normalized and displayed as the reconstructed position in physical dimensions of the LAPPD.

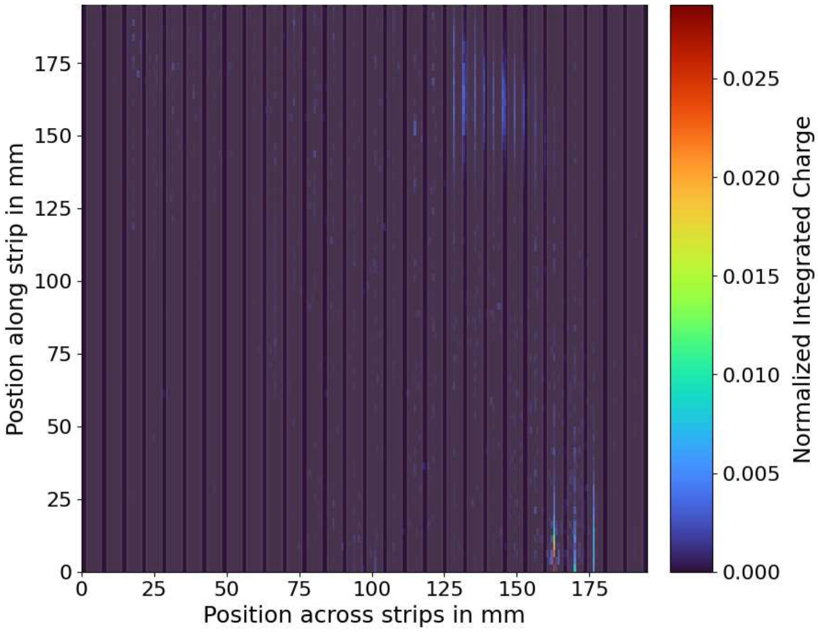

Figure 5.24: Integrated charge distribution for all events after the Beamgate cut and no multiplicity cut for LAPPD63. The charge is normalized and displayed as the reconstructed position in physical dimensions of the LAPPD.

6 The SiPM with light collector design

"Do what I do. Hold tight and pretend it's a plan!"
- Dr Who, 11th Doctor

The original SiPM with Light Collector (SiLC) design was developed as part of multiple master theses [20, 68]. The basic idea revolves around the combination of SiPM with light collectors (LC) to increase the light collection efficiency by increasing the effective photosensitive area. The idea behind such a design is to be able to build large scale arrays of detectors without needing several hundred/thousand detectors. More specifically the goal is to get large scale detectors with a high granularity for improved spatial resolution but also have a very good time resolution. Since for example a $20 \times 20\,\mathrm{cm}$ surface, comparable to an LAPPD from chapter 5, requires about 4400 SiPM if $9\,\mathrm{mm}^2$ SiPM are used a simple approach using only SiPM is not feasible. To avoid the large amount of SiPM that would be necessary the idea is to use less devices but outfit them with light collectors that significantly increase the active photosensitive area of the detectors.

In the original design the light collection was intended to be done by an Active Light Collector (ALC), which is basically a scintillator or WLS based on plastics. For this thesis the approach has been extended to also include Passive Light Collectors (PLC).

This chapter will describe the development and realization of this idea. First the concept design and the general idea as well as simulations for the optimal geometry will be explained. This is followed by a comprehensive description of its components, namely the SiPM, their electronics and the light collectors. Finally the test setup will be described and the results of multiple calibration measurements will be shown.

6.1 Conceptual design

The base design of SiLCs can always be seen as a combination of a fast timing SiPM as photosensor and a light collector. This light collector can be either a passive light collector or an active light collector depending on the materials. A passive light collector is made from PMMA or PS which only absorbs far UV to UV light. An active light collector uses materials like PMMA or PS as well but with added WLS. Chapter 3.1 explains the applications of these materials in further detail. Figure 6.1 shows the concept design for the light collector developed for this approach. Its shape was first determined to be a combination of a cut-off conic part connecting to the SiPM and a parabolic top part to increase internal total reflection [20]. From there on the optimisation of the different geometrical shapes has been further investigated and optimised in an additional master thesis focused on the simulation of this concept design [68]. The result of these simulations is the design used for the approach outlined in this thesis. The

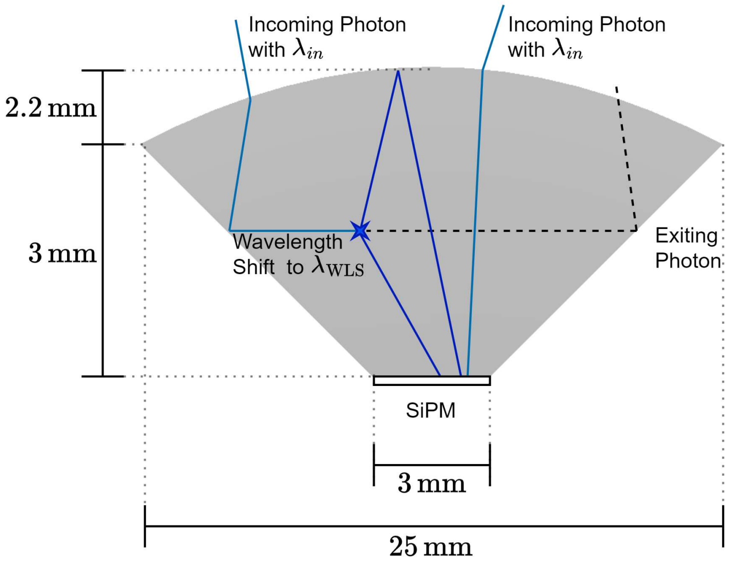

Figure 6.1: Schematic depiction of a SiLC module with its optimised geometrical properties. The module consists of a SiPM coupled to a light collector, which in this case represents both passive and active light collectors. Shown are two primary types of photon paths, shown as blue lines: one where an incoming photon directly reaches the SiPM, and another where the photon is absorbed by the wavelength-shifting material. In the latter case, the photon is re-emitted at a longer wavelength and in a random direction. Two possible outcomes for re-emitted photons that are successfully detected are shown as dark blue lines: a direct path to the SiPM, and an indirect path where the photon is reflected off the parabolic top surface of the light collector towards the SiPM. Additionally, a third path is shown as a dashed black line, representing a photon that is emitted at an angle $\theta_{in} < \theta_{crit}$. In this case, the angle of incidence is below the critical angle for total internal reflection, allowing the photon to escape the light collector rather than being directed toward the SiPM.

parameters that resulted in the highest light collection can be seen in table 6.1 and will be introduced in chapter 6.2. Both the principle for passive as well as active light collectors can be seen in figure 6.1. On the right hand side an incoming photon can be seen which refracts at the light collector surface towards the SiPM. On the left hand side a potential path for an incoming photon in an active light collector is shown. Along its path the photon will at one point be absorbed and re-emitted with a new, higher wavelength. Due to the emission being isotropic the newly emitted photon can again travel and be reflected in the light collector to reach the SiPM as shown with the two dark blue lines. The first line represent a direction towards the SiPM while the second line represents a direction where the photon is reflected off the parabolic top surface of the light collector towards the SiPM. The dashed black line represents a photon that reaches the parabolic top surface at an angle $\theta_{in} < \theta_{crit}$. In this case, the angle of incidence is below the critical angle for total internal reflection, allowing the photon to escape the light collector.

6.2 Simulations

As introduced in chapter 6.1, an important aspect of the entire SiLC design is the light collector. Two separate theses have been involved in the simulation of the light collectors shape [20] and size [68]. Independent of whether they are ALC or PLC the base design has to be optimised to work as intended. Therefore simulations for the optimised design have been made for both types of light collectors. A step before the simulations can start is to determine the actual composition of the light collector and its WLS. In this case the chosen materials are PS as basis for both types of light collectors with additional PPO and bis-MSB as WLS for the active light collector. With this composition the active light collector is sensitive to both far UV photons, from for example Cherenkov radiation, as well as emission from other sources. An example for this is the WbLS introduced in chapter 3.1 which in some cases uses only PPO as WLS. The additional bis-MSB makes the SiLC light collectors sensitive to light emitted by the WbLS by shifting the wavelength towards the sensitive area of the SiPM which is around 420 nm.

Table 6.1: Result of the simulations for the optimal parameters for the light collector as used in this thesis [68].

Parameter [Unit]	Value
SiPM radius [mm]	1.5
Max radius [mm]	12.5
Cone height [mm]	3
Parabola height [mm]	2.2

For the size optimisation simulations [68] a light source is simulated in 20 cm distance to the upper tip of the light collector with a beam angle of $\theta = 10.2^\circ$. The light source is then incrementally moved sidewards in 5 mm steps to simulate different angles of incidence. At each position the light source emits a set number of photons (always 50000) at 310 nm in random directions facing the light collector. The simulations were performed in the Geometry and Tracking 4 (Geant4) framework [69] which allows for the simulation of photons or particles and their interactions. In this case the framework simulates the path of the photons from the light source to the light collector, the path within the light collector (including the WLS process for the ALC) and the transition to the SiPM. Once the photon reaches the SiPM it is counted as detected (while all others count as lost). The simulation uses a constant PDE of 1 for the SiPM at all wavelengths.

To reduce the amount of time necessary for the simulations to run, the radii of the light collector have been fixed. The first radius is the radius of the SiPM (1.5 mm) which is given by the chosen SiPM model introduced later on. The second radius is the maximum radius of the light collector which is limited by constraining a fully scaled array of SiLC detectors to an 8×8, 200×200 mm array. This results in a maximum radius of 12.5 mm. Figure 6.2 on the left hand side shows the results of the simulation for a PLC based on only PS as the amount of detected photons against the x-position of the light source. Figure 6.2 on the right hand side shows the results for the ALC design based on PS with PPO and bis-MSB. Both plots show the amount of detected photons against the x-position of the light source and different colours show different combinations of the two height parameters. From the simulation results it can be concluded that, both for PLC and ALC, the optimal geometry is a cone height of 3 mm and a parabola height of 2.2 mm as shown in table 6.1.

Figure 6.3 shows more in-depth simulations of the chosen geometry for both PLC on the left hand side and ALC on the right hand side. The principle is the same as before where the light

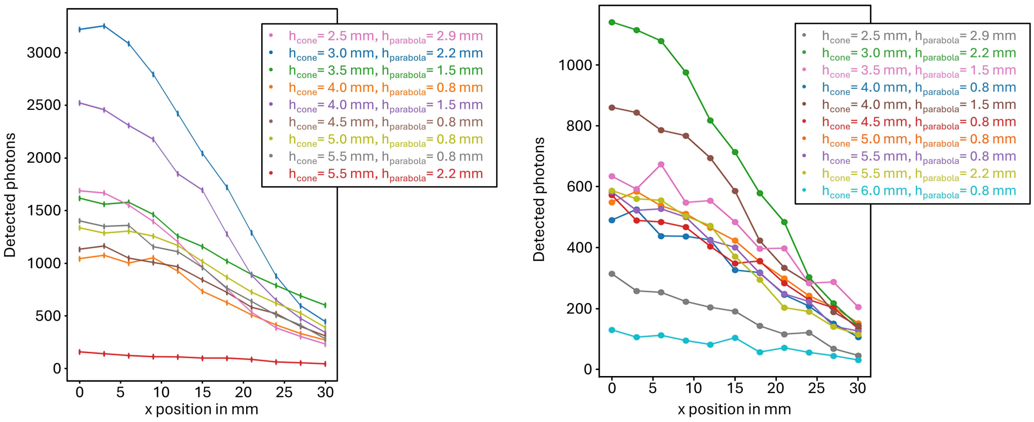

Figure 6.2: Simulation results for a passive light collector based on PS (left hand side) and an active light collector based on PS combined with PPO and bis-MSB (right hand side) which was run in the Geant4 framework. The data shows the detected photons against the x-position of the light source for 50000 initial photons at each position. The different colours represent different geometries [68].

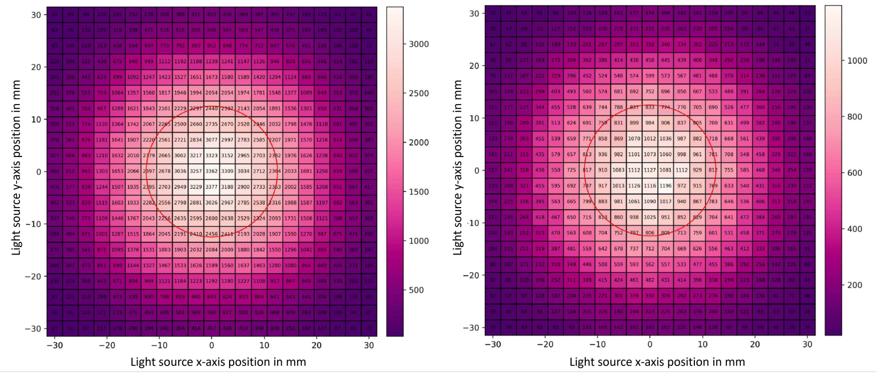

Figure 6.3: In-depth simulations for both ALC and PLC. A x,y-scan was performed for light source positions in the range of −30 mm to 30 mm in 3 mm steps. Each square represents the amount of detected photons on the SiPM at that position. The red circle shows the position and size of the light collector. [68].

source is at a distance of 20 cm and 50000 photons are emitted for each position. The difference is that a x,y-scan is performed for light source positions in the range of −30 mm to 30 mm in 3 mm steps. Each square represents the amount of detected photons on the SiPM with the light source at that position. The red circle shows the position and size of the light collector. Figure D.1 in appendix D shows the same type of plot but without a light collector. This shows that both PLC and ALC should significantly increase the amount of detected photons. Another result of the simulations is to decrease the amount of losses on the sides of the cone of the light collectors by coating them in a reflective material. Figure D.2 in appendix D show an x,y-scan simulation for a PLC with no reflective surfaces. While the amount of collected photons with a light collector is higher than for no light collector, it is a magnitude smaller than for a PLC with reflective coating. The experimental realisation of the coating will be discussed in the next chapter.

6.3 Production of the light collectors

With the simulations concluded in a optimised design the next step is the production of the light collectors themselves. For this the light collectors were first produced, by the Johannes Gutenberg University (JGU) Mainz, as 2 inch cylinders. These uncut slugs are then handed to our institute workshop in Tübingen to cut them to the desired design. They are first lathed down to match the conic and parabolic shape and afterwards they are polished on both the parabolic top and the connection surface to the SiPM. Once polished, the walls of the cone which have not been polished are painted in a reflective coating to minimize the loss on those sides.

Since the reflective coating on the sides of the light collectors conic part is important, it needs to be further discussed. The coating is doable in a multitude of ways like for example with paint or reflective foil. For this design paint has been chosen as best option with the reason being the easiness of applying paint compared to glueing a foil to the light collector. Due to the size of the light collector and the need for human application of the reflector working with such small sizes gets difficult quickly for a reflective foil. Another aspect is that the glue used on the reflective foil has to also match the refractive index of the material and also be chemically compatible. With these aspects in mind the paint has been chosen as a better option and the Eljen EJ-510 [70] reflective paint for plastic scintillators will be used.
With the paint chosen over a reflective foil the application still needs to be taken with a lot of precautions and preparations as such the application of the paint is done in a small scale clean room to prevent dust settling between paint and light collector. Once the light collector is cleaned with isopropanol it has to sit until all leftover liquid is vaporized since the paint is solvable by the isopropanol. Once the isopropanol has evaporated completely, the paint has to be applied in very thin layers and then left to dry over a period of a few hours to a day to prevent the wet paint being encased by dry paint which would lead to cracks in the layer touching the plastic impacting the reflective surface. Figure 6.4 shows this very well. In this attempt the paint was applied in one go and in a fairly thick layer. The result is that the paint cracked both on the outside as well as on the inside. Whereas the outside cracks are very visible on the right hand side the cracks are faintly visible on the left hand side as well. The cracks on the inside are marked in the figure in blue. Figure 6.5 shows an attempt that was done over a span of three days with each day a single very thin layer being applied. The result is a very homogenous reflective surface on the inside, which can be seen on the left hand side. Also from the outside on the right hand side the paint is more uniform and has no cracks. Once the light collectors are painted they can be connected to the SiPM with either index matching glue or a drop of mineral oil.

6.4 Electronics and SiPM

Since the SiPM and the goal of building an array out of SiLC modules is a crucial part of the detector design development such an array and the accompanying electronics were developed and build in a master thesis. In the scope of this thesis several Printed Circuit Board (PCB) for the array have been successfully produced [68]. Figure 6.6 shows the electronics as they are used in the experimental setup while figures E.2 and E.1 in appendix E show the circuit schematics. The electronics can be divided into two parts, the SiPM carrying PCB (Figure 6.6 on the right hand side) and the supply PCB (Figure 6.6 on the left hand side). The former one consists of SiPM shuttle boards each outfitted with a SiPM and a temperature sensor and a master PCB to slot the shuttle boards into. The master PCB also has several integrated circuits for biasing, impedance matching and signal amplification. It also has eight SMA outputs each for one SiPM

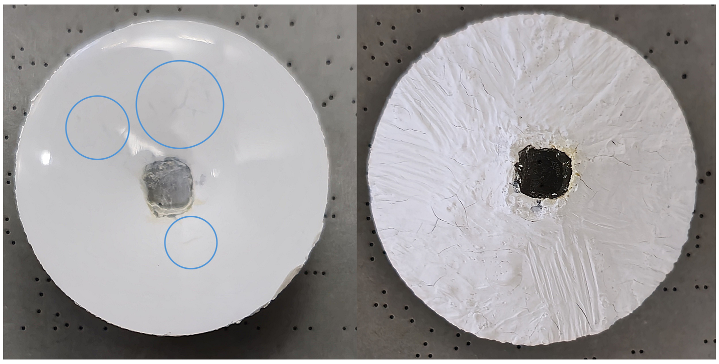

Figure 6.4: Example of a badly painted light collector with an outer diameter of 25 mm. The paint was applied one in a thick layer causing the paint to crack on the outside as well as the inside which is the contact to the plastic of the light collector. The right hand side shows a bottom view and the left hand side a top view (inside) of the light collector.

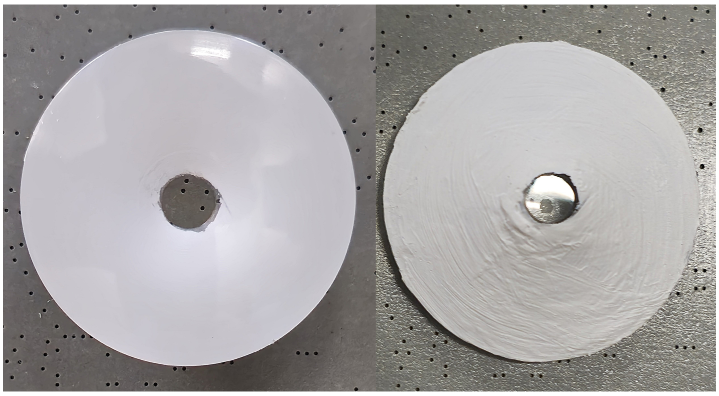

Figure 6.5: Example of a well painted light collector with an outer diameter of 25 mm. The paint was applied in a span of three days with each being a single thin layer. The inside (left hand side) and outside (right hand side) are homogeneous and no visible cracks can be seen.

signal and a ribbon cable connector for the bias voltage control as well as bias voltage and temperature readout. The supply PCB is a voltage control board in a RPi hat format. With this the control can be directly done via a Raspberry Pi without the need of external computers or power sources. It also features several jumper switches to enable or disable different features like the amplification, the boost voltage or the temperature readout. Lastly it has the counterpart ribbon cable connector to match the one on the master SiPM PCB. Connected to this voltage control board is a voltage boost board which has up to eight independent boost circuit to scale the RPis internal 5 V to the needed bias voltage between 25 V and 30 V given by the SiPM.
To control the voltages as well as monitor the returned voltages and temperatures the RPi creates its own web server on the local subnet making it accessible within the institutes network.

6.4.1 Comparison between SiPM fast output and normal output

The waveform produced by a SiPM is essential for analysis purposes and in part depends on the SiPM characteristics. This becomes especially important once a calibration is used to optimise to one parameter. The SiPM used for this thesis is an ONSEMI J-Series model and an excerpt of

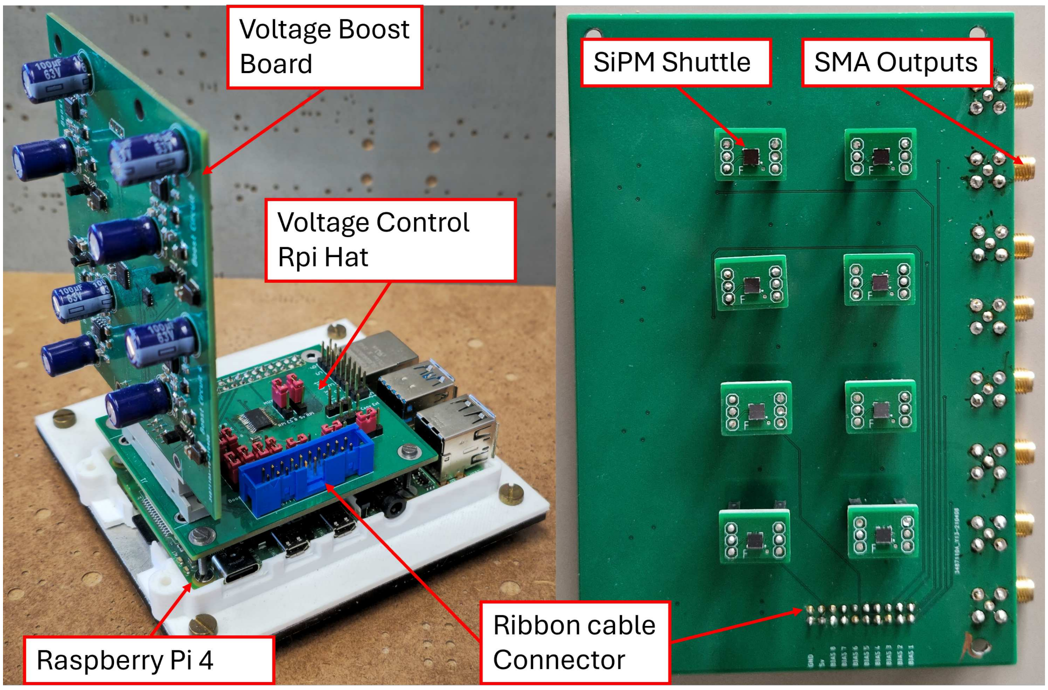

Figure 6.6: Pictures of the SiPM master PCB with SiPM shuttles on the right hand side and its control RPi equipped with a custom voltage control hat and boost board on the left hand side. All PCBs are custom designs based on a master thesis [68].

the data sheets device parameters can be seen in table 6.2. For the purposes used in this thesis the most relevant parameters are the gain for an improved signal to noise ratio and the time profile as well as the time resolution. While the gain is a bias dependent value the time profile and time resolution are mostly dominated by the recharge time of the SiPM's quenching resistor (see chapter 3.3.1). In the case of commonly available SiPM this is a device specific characteristic and cannot be influenced. For the time resolution the voltage dependence will be tested in chapter 6.6. In the case of the ONSEMI J-Series SiPM the device also offers a "fast output" which is a capacitively coupled output compared to the common cathode-anode output (see chapter 3.3.1). The main difference of this output is that it does not feature a long recharge tail but rather has a PMT like fast recovery. This offers a distinct advantage, namely, the improved ability to disambiguate multiple pulses that arrive in a very short amount of time. Where the common output has secondary pulses swallowed up in the recharge tail, the fast output clearly separates them into multiple pulses. Figure 6.7 shows this as an example pulse of an Anode Output Pulse (AOP) and a Fast Output Pulse (FOP). The blue waveform shows a s.pe. event taken by a FOP-SiPM in the setup described in 6.5. The pulse seen around 70 ns has a FWHM of (1.67 ± 0.0884) ns. The pink waveform on the other hand is an event from an AOP-SiPM. In this case only the recovery time of the pulse can be calculated properly to (27.7 ± 1.64) ns. What is immediately noticeable is that due to the long fall time during the recharge the falling flank becomes heavily impacted by noise. As marked in figure 6.7 the primary peak can be identified clearly, while secondary peaks are lost in the noise. An example of this would be the second marked peak which may or may not be another s.pe. event. This should demonstrate the capabilities and potential uses for a fast output and thus it will the primarily used form in this thesis.

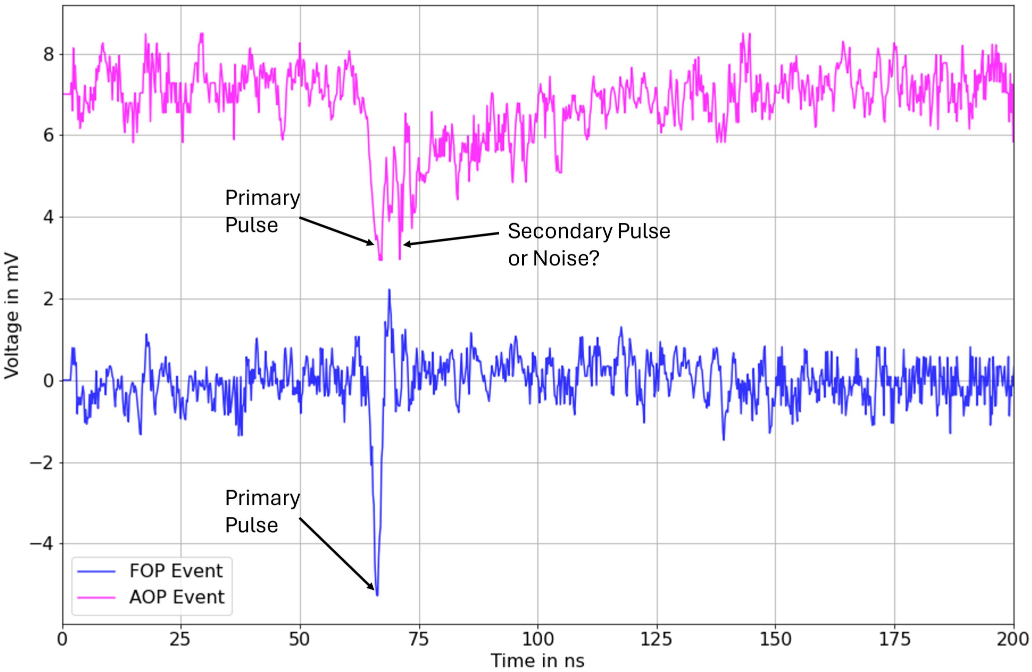

Figure 6.7: Comparative plot for an anode output pulse and a fast output pulse taken under similar circumstances and the same test setup. The anode output pulse can be seen in pink with its characteristic recharge curve of a SiPM, lasting well over 40 ns. The fast output pulse can be seen in blue and the PMT like behaviour with a pulse FWHM of around 1 ns can be clearly seen in comparison.

Table 6.2: Excerpt from the ONSEMI J-Series SiPM with all relevant parameters and ranges depending on the bias voltage [36].

Parameter	Value
Size [mm]	3×3
Fill factor [%]	0.75
Breakdown Voltage [V]	24.5
Over Voltage [V]	$1-6$
Spectral Range [nm]	$200-900$
PDE [%]	$38-50$
DCR @ 21 °C [kHz/mm^2]	$50-150$
Gain [10^6]	$2.9-6.3$
Rise Time [ps]	$90-110$
Normal Output FWHM [ns]	45
Fast Output FWHM [ns]	1.5

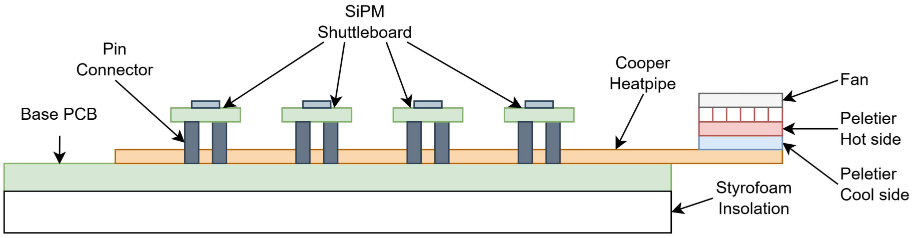

Figure 6.8: Schematic drawing of the Peletier cooling system mounted to the SiPM PCB. It consists of a Peletier thermo-electrical element which uses high currents to cool one side while heating up the other. The cooled side is mounted to copper heat pipes which in turn are mounted to the base PCB of the SiPM array directly cooling the SiPM. The hot side is pointed upwards to rise towards the intake of the air cooling system. Also shown are the SiPM shuttle boards mounted on their pin connectors.

6.4.2 Dark-Count-Rate and cooling solutions

One of the problematic downsides of using SiPMs is their very high DCR due to their solid state nature (see chapter 3.3.1). As seen in table 6.2 the DCR for the used SiPM is around 1 MHz and thus at a relevant level to be considered significant background. The type of measurements aimed for in this theses, which tries to determine scintillator emission time profiles, are highly affected by the DCR backgrounds. This is especially true for the low event rate tails. The only way to reduce this background is by cooling down the SiPMs themselves and reducing the DCR. This chapter will describe the cooling solution used and its effect on the DCR. The cooling system consists of two different, independent systems: A Peletier cooling system directly mounted to the SiPM PCB and an air cooling system explained in a later chapter about the experimental setup. The former of the two systems can be seen in figure 6.8 and is basically a Peletier element mounted to copper heat pipes which in turn are mounted to the SiPM PCB. By applying a current to the Peletier element the side connected to the heat pipes cools down while the other side heats up. To prevent the element and the SiPM next to it from getting to hot a fan is used to transport the hot air upwards towards the ceiling of the darkbox. The darkbox will be later introduced but can be seen in figure 6.11. This figure also shows the air cooling system atop the box. It is a reworked portable camping cooler supplied by an external voltage. This cooler is connected to the dark box via two separated pipes. A lower pipe outfitted with a fan to transport the cooled air into the darkbox and an upper pipe to lead the hot air back to the cooler. An additional 20 cm × 8 cm silica pack is placed inside to keep the humidity inside the cooler as low as possible.

The systems are designed to operate separately as the operation of both at the same time create issues for the temperature distribution within the test setup. Another issue stemming from this mixed cooling is an increase in condensation water close to the electronics which puts the entire experiment at risk. To see which of the two systems is more efficient in cooling the SiPM a temporary test setup has been integrated into the darkbox seen in figure 6.12. The setup is fundamentally the same as seen in the figure but instead of routing the signal to an ADC it is instead routed to a combination of a VME discriminator (V895 [71]), and a VME scaler (V819 [72]) both from CAEN. The discriminator is set to trigger on an estimated 0.5-0.6 s.pe. leading edge and the scaler collects the amount of triggers within a second to get the DCR. For this no light source or scintillator sample has been deployed.

Figure 6.9 shows the temperatures and DCR taken this way. The temperature is taken from the temperature sensors mounted on the back of the SiPM shuttle boards. This means that in case of higher temperatures they function as a heat sink and show a slightly different temperature from the actual SiPM temperature. What can be seen is three different populations one each for no cooling, Peletier cooling and air cooling. The right hand side shows the temperatures of the SiPMs and as expected the non cooled option runs the hottest. The medium option is the Peletier cooling which cools down the temperature about 5 °C compared to no cooling. The air cooling on the other hand manages to cool down the temperature by another 5 °C which brings the temperature down 10 °C compared to no cooling. This is also noticeable in the DCR which can be seen on the left hand side. No cooling results in a DCR around the expected 1 MHz while the Peletier cooling option reduces the DCR to 0.7 MHz and the air cooling to around 0.35 MHz. This combined with the easier application and de-coupled condensation issue of the air cooling system makes it the superior cooling system successfully reducing the DCR to a third. Looking closer at the chosen cooling options and the distribution shown in figure 6.9 the distribution shows two separated populations in both temperature and DCR. Figure 6.10 shows the time evolution of this data set for the DCR, the temperature as well as the bias voltage over an entire day. What can be seen is a change depending on night or day time. Since the cooler used is dependent on the outside temperature a change directly affects the system, although only marginally. This is also visible in the DCR as both temperature and DCR perfectly follow the same trend and as such show the correlation of the two and the importance of a good cooling system. This day/night cycle is addressed by covering the box in a layer of styrofoam insulation. Another consideration is the dependence of the gain on the temperature. The data sheet [36] list a breakdown voltage temperature dependence of 21.5 mV / °C which corresponds to a change in gain of $2.14 \cdot 10^4$ per °C change. This makes a 0.34% / °C difference for a gain of $6.3 \cdot 10^6$ as given by the data sheet for a maximum over voltage. Given this estimate of the gain's temperature dependence, it does not need to be considered in the following analyses.

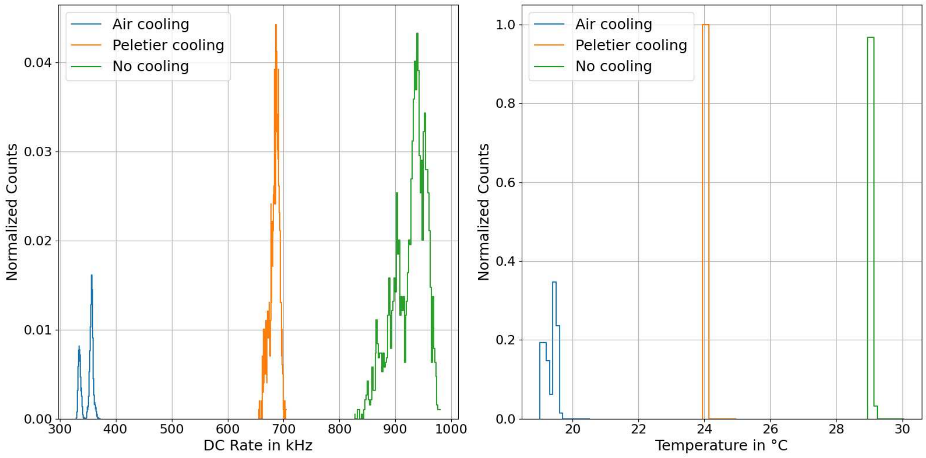

Figure 6.9: The right hand side shows the temperatures for the SiPM with no cooling, Peletier cooling and air cooling in three distinct distributions. The left hand side shows the corresponding DCR for the same cooling options. For the distribution of the DCR a value was taken every second.

6.5 Experimental test bench setup

One of the critical pieces of infrastructure for both already discussed DCR measurements as well as the upcoming calibration measurements is the used test bench developed for this reason. The requirements necessary for this test setup are to create light tight environment with RF-shielding

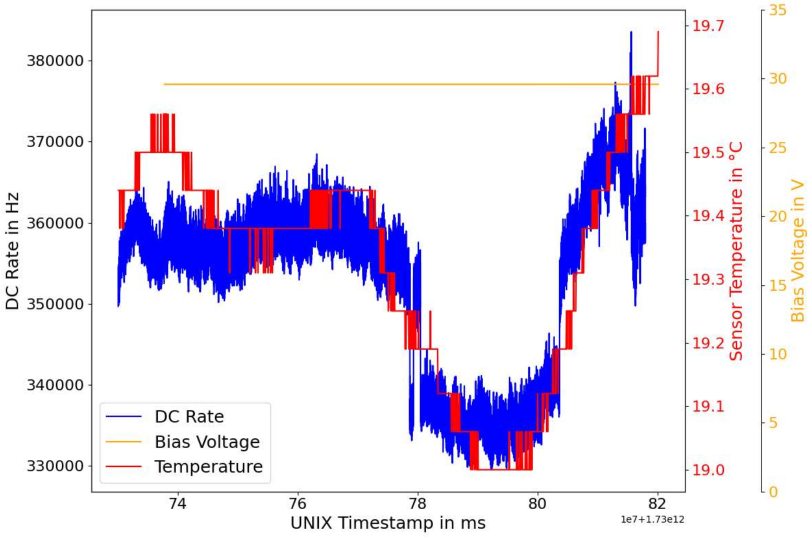

Figure 6.10: Time evolution of the air cooled dark box over the span of one day. A change in both temperature and DCR can be seen depending on the time of day with both being lower during the night.

to allow for a good distinction between signal and noise. Similarly the cooling systems in chapter 6.4.2 need to be included as well to additionally reduce dark noise. To accommodate this the basis for this setup is a solid aluminium box [73] which already provides a good protection against electromagnetic interference from outside due to it being a faraday cage. The box, henceforth called darkbox, is additionally grounded to prevent the system from being in a floating state as it could interfere with the signals leaving the box. This box can be seen in figure 6.11 as central piece in grey. On top of the box is a commercial cooler placed as described in chapter 6.4.2 with two separate pipes connecting it to the box below. Both, cooler and darkbox, are covered in a 4 cm layer of styrofoam to isolate it from the outside as much as possible. The only openings in this encasing are at the top of the cooler to allow the produced hot air to leave and at the cable duct leading outside which can be seen on the bottom right corner. Inside the darkbox a metal frame is placed to mount all necessary components to their respective positions. At the top and bottom of this frame are muon panels made from a scintillating plate and an adjacent PMT (Hamamatsu H3690 [74]) to be able to trigger on muons passing through both panels. This coincidence trigger makes up one of the two available trigger modes. In between the muon panels the SiPM array is placed towards the bottom panel. Additionally a spherical vessel can be placed above the SiPM array to characterise liquid material samples such as HPLC or scintillators. Right next to this vessel a different PMT (Philips XP2020 [75]) is placed and in case of a scintillating material this PMT can be used as trigger system as well. Additionally several temperature and humidity sensors are placed inside and outside this setup. All of this is accessed via the cable duct and the lines running through said duct are: Three HV and three signal lines for the PMTs, three lines for temperature sensors and the cooler fan and up to 16 lines for the SiPM data signals. The bias voltage accessed via the ribbon cable seen in figure 6.6 is not routed through the cable duct but individually along the darkbox edges. Once outside the darkbox the connections of the cables can be seen in figure 6.12. The PMT cables route to an HV crate for bias supply and to a VME discriminator from CAEN (V895 [71]) for the trigger signal creation. The discriminator is a leading edge type allowing for fast response times as well as low thresholds and it allows for coincidence settings between the different PMTs and the two trigger systems. The produced trigger signal as well as the SiPM signal connections are

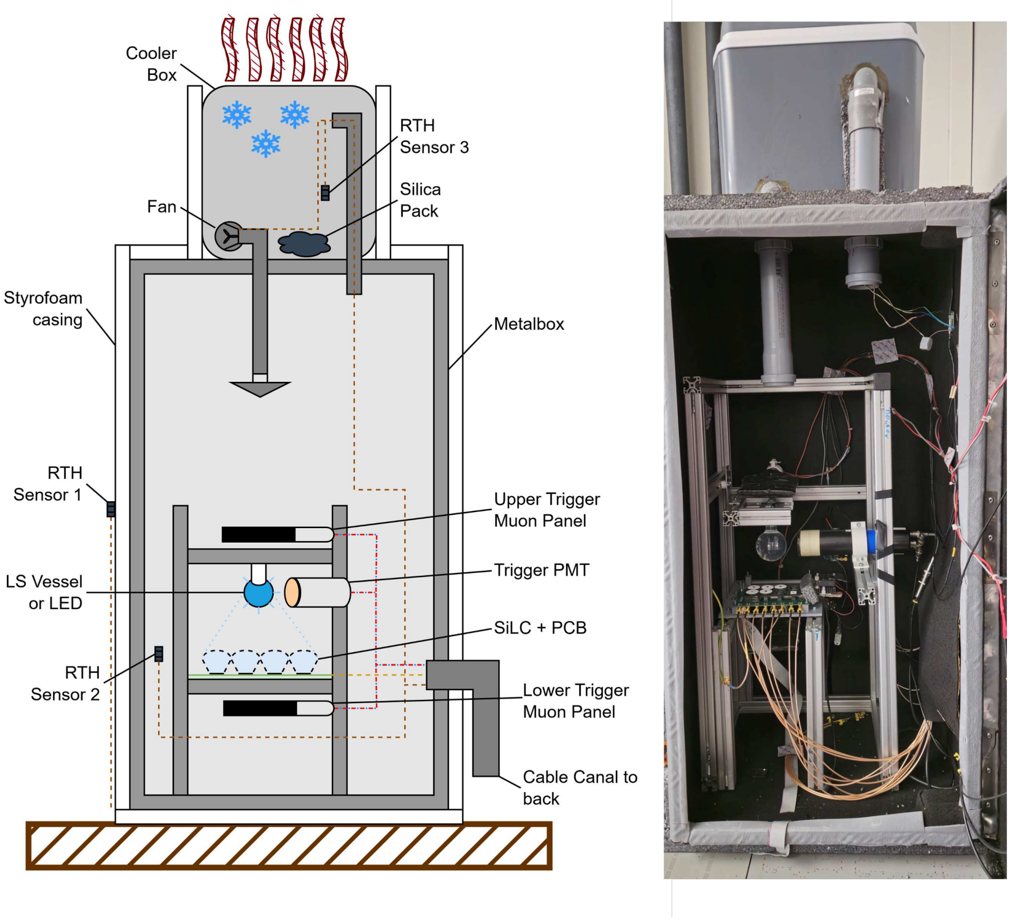

Figure 6.11: The left hand side shows a schematic drawing of the details in the darkbox used in the test bench setup. The base for the darkbox is an aluminium metal box [73] which also functions as a faraday cage. On the top of the darkbox a cooler is mounted and connected to the darkbox and both are encased in a layer of styrofoam to isolate it from the outside temperature changes. Inside the darkbox a metal frame with all necessary components can be placed. The components include a liquid scintillator vessel, two different trigger systems (a sidewards PMT next to the vessel and a muon coincidence trigger build from two muon panels) and the SiPM array. All of the connecting cables are guided outside through a cable duct in the bottom corner. The right hand side shows a photograph of the setup.

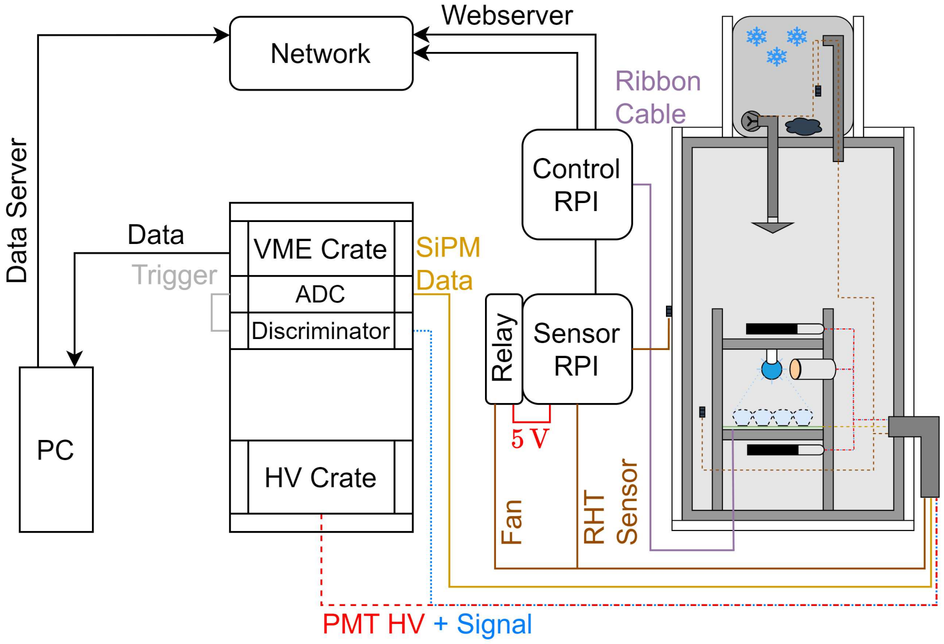

Figure 6.12: Schematic drawing of the full test bench system. On the right hand side is the darkbox described in figure 6.11, the cable duct and the exiting connections can be seen from there on. In brown the connections for the sensors and fan of the cooling systems to a RPi can seen. The purple connections shows the connection between the SiPM array and its corresponding RPi as described in 6.6. Both of these RPi open a web server accessible on the internal network to control the SiPM array as well as the cooler fan. The red and blue connections are the HV and signal cables for the PMT based trigger systems. The signals are fed into a CAEN VME discriminator (V895 [71]) which produces a trigger signal (grey) that is directly fed into a CAEN ADC [76]. Lastly the yellow connections symbolize the cables for the signal of the SiPM array which are fed into the above mentioned ADC. In the event of a trigger the data is transferred to a network storage via a central computer running a custom DAQ software.

collected at a CAEN V1742 digitizer [76]. This digitizer is capable of reading 32 channels at 5 Gs/s with 12 bit thus allowing for a fast sampling during digitizing. The digital data is then transferred to a connected computer via an optical link. The temperature sensors and fan are connected to one RPi while the ribbon cable for SiPM biasing is connected to an other RPi. The data computer is connected to a network to transfer the data to an internal server for storage. The RPis are connected to the same network creating their own web servers on the subnet making it accessible in the internal network.

6.6 SiPM calibration measurements

Before the start of the measurements for the liquid scintillator samples and the mounting of light collectors the SiPM available have to be calibrated. For this two different calibration measurements are done. The first is a 420 nm LED calibration for which an LED (VL420-5-

15 [77]) is placed in the darkbox instead of the liquid scintillator vessel and is directly pulsed via a function generator to produce s.pe.. The downside of a calibration like this is that the actual value of determined time characteristics might be smeared due to the long pulse width of the function generator which is around 16 ns plus two additional 8 ns due to the rise and fall time. This long pulse width can cause timing characteristics to be smeared but will leave the spread of the individual TTS values intact and show the dependency of the TTS on the bias voltage. For this reason a first calibration of the SiPM TTS as well as pulse height for different voltages will be used to determine a suitable bias voltage. With this voltage the secondary calibration measurement is done in which a High-Purity-Low-Conductivity (HPLC) water filled vessel in combination with the muon panel trigger system described in chapter 6.5 is used. With this the trigger condition is a muon passing through a panel above the liquid vessel and a panel below the SiPM array. A trigger caused by this process is likely to have the muon pass through the liquid vessel itself, producing Cherenkov light in the process. Since Cherenkov photons are produced near instantaneous, and in this case on a time scale far below the time resolution of the detectors, it is suitable to determine the time resolution of the sensors. As about one in ten triggered events contain a response pulse from the SiPM it can be concluded that the time resolution is determined at the s.pe. level.

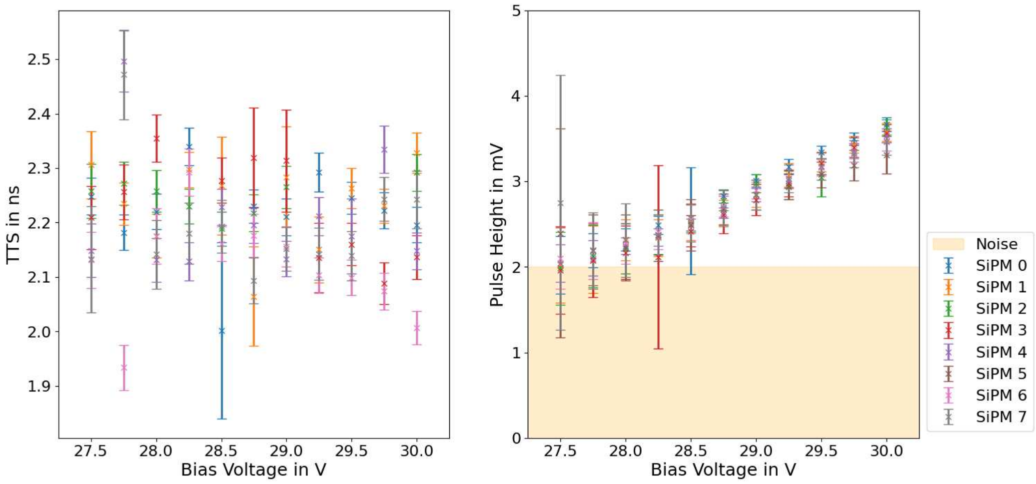

Figure 6.13: LED characterisation measurement of the available SiPM. Both TTS on the left hand side and the pulse height on the right hand side are shown in regards to the applied bias voltage.

Figure 6.13 shows the result of the primary calibration. On the left hand side the TTS is shown for all available devices and a bias voltage span from 27.5 V to 30 V in 0.5 V steps. The TTS in this case is determined from the distribution of the transit time between the systems trigger and the pulse in the recorded waveform. Fitting the distribution with a Gaussian will result in the TTS and its error from the resulting sigma of the fit. The right hand side shows a similar plot to the left hand side but with the pulse height instead. The pulse height and its error are determined by fitting the distribution of the pulse heights of waveforms that contain a pulse at the expected position with a multi Gaussian function. Additionally a band indicating the usual noise range can be seen. To determine the best bias voltage to run future measurements, two factors are important. The first is the ability to differentiate signal form the background noise which limits the available voltages to 29 V and above to get a significant difference. To prevent damages due to the SiPM running on the maximum allowed voltage of 30 V it is removed as option as well. To determine the final bias voltage the TTS can be used as second factor. For this there are two approaches, the first being to choose the bias voltage that shows the least amount of spread over all sensors which would be 29.5 V. The second approach is to choose the individually lowest TTS available and give each device its own specific bias voltage. To prevent SiPM from being mixed up during changes and the mounting of the light collectors the first approach has been chosen as more suitable. As such the choice is to run all SiPM at a voltage of 29.5 V to get the least amount of spread between the SiPMs. To show the timing capabilities of the SiPMs a calibration as described above using Cherenkov radiation and the bias voltage of 29.5 V has been done. The time difference between the recorded signal of the muon panel coincidence and the SiPM response pulse can be seen in figure 6.14 for six SiPM slots available for the test SiPM array PCB. Compared to the TTS derived from the LED calibration the TTS using Cherenkov radiation as light source results in values lower than 1 ns down to 800 ps. To get the time resolution of only the SiPM without the effect of the muon panels of the trigger system the time resolution of the muon panels ((540.5 ± 14.7) ps) has to be unfolded from the determined time resolutions. The resulting time resolutions of the SiPM can be seen summarized in table 6.3. This allows the SiPM array to perform on a level where the resolution of fast timing processes can be achieved. An example for this would be the determination of scintillation decay times.

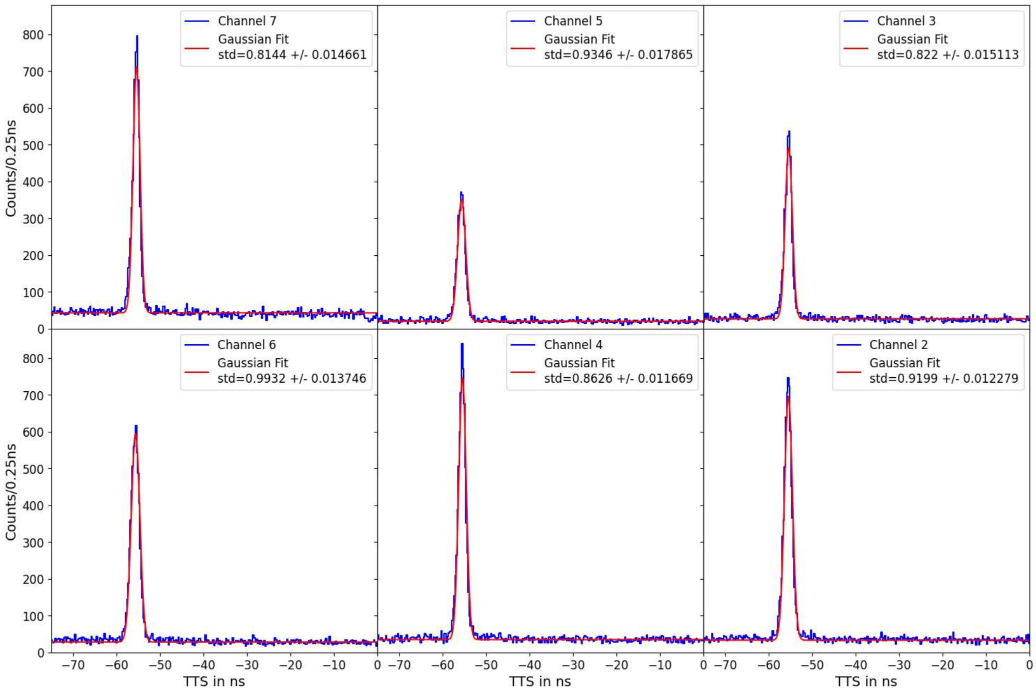

Figure 6.14: Transit time distributions for six SiPM taken from Cherenkov radiation data. The transit time was determined from the difference between trigger signal and SiPM pulse. The calibration was done for the six available SiPM slots. All channels show a sub nanosecond TTS derived from a Gaussian fit.

Table 6.3: Summary of the TTS results for the transit time distributions. The data was taken for six SiPM with Cherenkov light as source. Shown time resolutions of the SiPM without the influence of the coincident muon panels as trigger.

Channel	Value ± error [ps]
2	454.2±33.35
3	189.1±84.87
4	322.7±44.22
5	483.3±40.35
6	588.7±28.86
7	152.7±102.5

7 Performance tests of SiPM with light collector modules

"People assume that time is a strict progression of cause to effect, but actually from a non-linear, non-subjective viewpoint — it's more like a big ball of wibbly wobbly, timey wimey, stuff."

- Dr Who, 10th Doctor

The goal for the last part of this thesis is to test the SiLC modules for their capabilities in terms of the measuring different liquid samples and the effect of the light collectors on the timing and their collection ability. From the geometry determined by the simulations in chapter 6.2 the light collectors will increase the active area by a factor of roughly 70 which means an increase in events should be visible for the light collectors. For this sake a round bottom flask, with an inner diameter of 6.4 cm made from UV transparent material, was mounted as vessel as indicated in the schematic drawing of the dark box in figure 6.11. The vessel will be filled up to the neck of the flask, which corresponds to a filling height of 6.4 cm as well. The distance from the top of the SiPM array to the bottom of the vessel is 10 cm. The liquid samples that have been used are:

- An HPLC water sample to produce pure Cherenkov radiation.
- An LAB, 2.5 g/l PPO, 3 mg/l bis-MSB combination as in modern liquid scintillators made alongside a master thesis [78].
- A WbLS sample, with PPO, to produce both scintillation light and Cherenkov radiation made at the Technische Universität München.

These samples will in the scope of this chapter be used and the light will be detected by an array of SiPM without light collector, a SiLC array with passive light collectors and a SiLC array with active light collectors. The goal in the end will be to determine the time profiles and decay times of the different samples. Important to note is that the amount of used SiPM is reduced to six instead of the possible eight due to two damaged channels. For measurements with passive light collectors this is further reduced to five and for active light collectors to two as only these number of light collectors were available during these measurements. The excitation method for the samples is in all cases cosmic muons passing through the vessel. Time differences due to photon runtime differences inside the vessel are non-negligible with a maximum travel time difference of 283 ps to 320 ps depending on the sample, which has to be taken into account as well. These values have been estimated by taking the vessel size as well as the refractive index of the samples into account.

7.1 Liquid scintillator time profile model

Before the data of the measurements can be analysed the model to describe the time profiles needs to be understood. For a single component that contributes in the scintillation process it is described by an exponential decay [79] like:

$$S = \exp\left(\frac{-t}{\tau}\right) \tag{7.1}$$

where τ is the decay time. This is modified for N contributions as a sum of exponential decays:

$$S = \sum_{i}^{N} n_i \cdot \exp\left(\frac{-t}{\tau_i}\right) \quad , \tag{7.2}$$

where n_i are the normalisations factors and τ_i the decay times of the scintillator. Figure 7.1 shows this for different scintillators with one to four contributions. The additional contributions are always slower and less frequent then the one before to mimic the behaviour of real liquid scintillators. What can be seen is that for the curves with slower contributions the timescale moves from around some tens of nanoseconds for two contributions to hundreds of nanoseconds for four contributions.

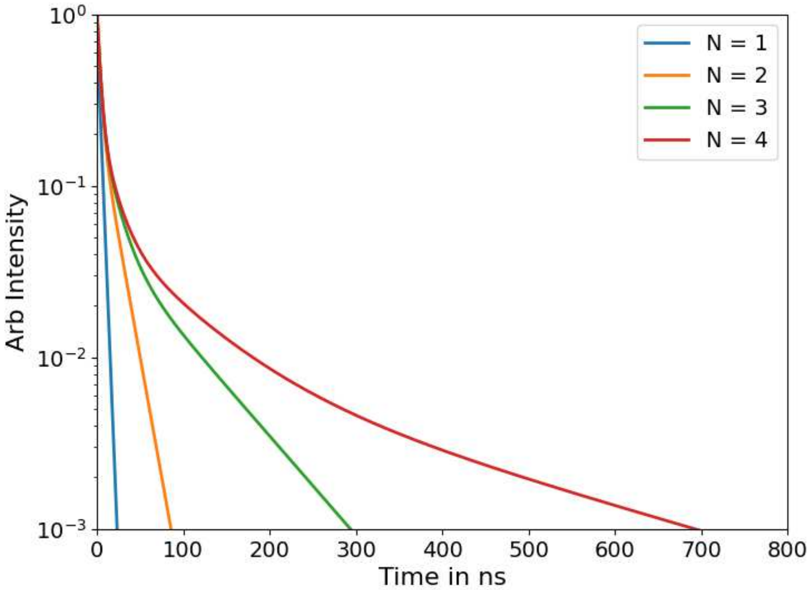

Figure 7.1: Theoretical exponential decays for the model described in equation 7.2 for one to four exponential decay contributions of the scintillator as they would appear in real liquid scintillators. The curves show the time profile without the existence of any background radiation.

To now adapt this theoretical model for real experimental conditions several modifications need to be accounted for. The first is the addition of a background as due to the nature of SiPM a high DCR is to be expected which will dominate the background. The next aspect to consider is the non-zero rise time of the scintillator excitation. With photosensors that are fast enough, which in this case with sub-ns timing is the case, the rise time is no longer negligible. As such the exponential model described in equation 7.2 needs to be adjusted with an additional exponential rise time τ_R [80]

$$\mathrm{S}(t) = \Theta(t - t_s) \sum_i^N \frac{n_i}{\tau_i - \tau_R} \left(\exp\left(\frac{-(t-t_s)}{\tau_i} \right) - \exp\left(\frac{-(t-t_s)}{\tau_R} \right) \right) + \mathrm{BG} \quad , \tag{7.3}$$

with t_s representing the start time of the scintillation process and BG the background level dominated by the dark counts of the SiPM. Additionally a Heaviside function has been added to account for $t < t_s$. With this the full exponential decay of a scintillator with multiple exponential decays can be described.

The last aspect is to account for the non-zero detector response time which is usually a device characteristic and fairly constant. It is described as a Gaussian distribution solely reliant on the time resolution of the respective detector. In the case of the used SiPM these have already been determined in the calibration done in chapter 6.6. The Gaussian response then looks like:

$$\mathrm{G}(t) = \exp\left(\frac{-t^2}{2\sigma_{\mathrm{SiPM}}^2} \right) \quad . \tag{7.4}$$

To now combine both the Gaussian detector response in equation 7.4 as well as the full scintillator decay model in equation 7.3 they are convoluted into a new model M:

$$\mathrm{M}(t) = \mathrm{G}(t) \otimes \mathrm{S}(t) \tag{7.5}$$

The function used to fit the data in the following chapters is equation 7.5, where the WbLS uses $N = 2$ for $\mathrm{S}(t)$ (equation 7.3) and the LAB+PPO+bis-MSB scintillator uses $N = 3$ for $\mathrm{S}(t)$. The time resolutions of the SiPMs σ_{SiPM} in the Gaussian contribution (equation 7.4) are the time resolutions determined in chapter 6.6 table 6.3 and are fixed for each device for all fits.

7.2 Comparison between the sample time profile for only SiPM

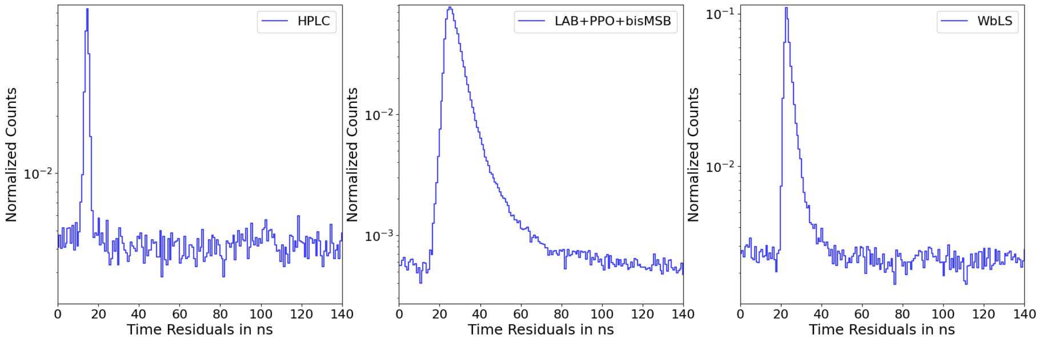

Figure 7.2: Time residual distribution of the three liquid samples for SiPM without light collectors. The left hand side shows the HPLC water sample which produces only Cherenkov light and as such shows one sharp Gaussian peak. The centre and right hand side plot show the scintillator samples for LAB+PPO+bis-MSB and WbLS, respectively. The LAB based scintillator shows a long decay time while the WbLS has a rather short decay time.

To gain an understanding of the behaviour of the different time profiles of the samples, the first measurements were taken with SiPM without light collectors. The test setup introduced in chapter 6.5 will be used for all following measurements. The HPLC water sample uses

coincident muon panels as trigger. For the scintillating samples the side PMT can be used as trigger due to the isotropic emission of the scintillation light. Since the side PMT can directly trigger on the scintillation light it does not require a coincidence of two muon panels and thus has an increased trigger rate. The side PMT also a lower time resolution of $\sim 250\,\mathrm{ps}$ [75] compared to the muon panels which improves the timing of the system overall. The result of these measurements can be seen exemplary for one SiPM in figure 7.2. To get the time profile, the time difference between the trigger signal and the 50% level of the rising flank of the pulses present in the waveforms are determined. To count, a pulse needs to have a peak exceeding 0.75 s.pe. as defined by the calibration in chapter 6.6 as 2.25 mV peak height and have a width of at least 5 samples which at 5 Gs/s corresponds to 1 ns. The time residuals are then binned in units of the time resolution of the SiPMs and the time residual distribution is normalized to 1.
On the left hand side the HPLC is shown with a distinct Gaussian peak around the 20 ns mark which matches the expected behaviour of pure Cherenkov radiation. The shift to 20 ns is due to the delay between trigger signal and pulse and is the result of cable length differences and DAQ runtime. This method is what was used to calculate the TTS during the calibration in chapter 6.6. The centre plot shows the time profile of the liquid scintillator based on LAB+PPO+bis-MSB, which exhibits a noticeably longer exponential decay. Additionally, after a certain decay time, the tail of the distribution asymptotically approaches the background level, which is primarily influenced by the DCR of the SiPM. Lastly on the right hand side the WbLS sample is shown. Compared with the LAB based sample the WbLS has three distinct differences, the first being a shorter decay time tail. The second difference is the rise time of the scintillator which is faster compared to the LAB based scintillator. The reason is that for the WbLS the rise time is dominated by the high contribution of Cherenkov light relative to the low scintillator light yield, whereas in the LAB based scintillator, the high scintillator light yield makes the Cherenkov contribution negligible. Third, there is a difference in background level between the LAB sample, which has a better signal to background ratio, compared to the other two samples. For the HPLC measurement this can be explained with the trigger system being the coincident muon panels. Due to the makeup of the muon panels a passing muon does not necessarily pass the vessel as well and due to the high DCR of SiPMs a large fraction of triggers will have dark pulses in them instead of being empty which gives a uniform background level. From the DCR determined in chapter 6.4.2 and the ADC of 200 ns it is expected that each waveform contains, on average, 0.07 dark counts. In the case of the WbLS it is a similar reasoning. Due to the low light yield of WbLS in general and the trigger system being the side PMT that triggers on the scintillation light only a fraction of triggers actually produce photons that will hit the SiPMs. This results in a worse signal to background ratio. While the LAB based scintillator measurement also shows this uniform background level it is significantly lower due to the lower fraction of waveforms without photon pulses induced by the scintillator.

7.3 Scintillator time profiles using SiPMs with and without PLC

To test if the light collectors have an impact on the decay times of the available liquid scintillator samples, the decay times will be determined by fitting the model described in equation 7.5 to the distribution of the time residuals. In this chapter this is done for SiPM without light collectors and SiPM with PLC. SiPM with ALCs will be discussed in a later chapter by themselves.
The first sample that was measured and analysed was the LAB+PPO+bis-MSB scintillator. Figure 7.3 shows the time residual distribution of the scintillator recorded by SiPMs without light collectors and figure 7.4 shows the distribution for SiPMs with PLCs. As only five PLCs are available the distributions for only five SiPMs are shown in figure 7.4. The time residuals have been binned in terms of the device time resolution and the distribution has been normalized

to 1. The data is shown as blue bars with the magenta dashed line as the overall fit. The orange, green and grey dashed lines are the different contributions of the three exponential decays. The plot shows the distributions of the SiPMs as they are physically placed on the main board. What can be seen as well is that the lower two channels have an irregularity around the 100 ns mark which seems to a systematic issue with the SiPM master PCB. Changing a SiPM shuttle board or switching the position does not change the appearance of the irregularity on the lower channels and has thus to be taken into account for future measurements. The fit results for the decay times τ_i, the reduced normalisation factors n_i and the rise time τ_R together with their standard deviation as error are listed in table 7.1 and 7.2 respectively. What can be taken from the tables and figures is that the two faster components τ_0, τ_1 are fairly consistent, similar to the rise time τ_R of the scintillator. Compared to them the third component τ_2 is very inconsistent and the errors become unrealistically large. This can be tracked down to two reasons, the first reason lies in the long tail of the distribution. After a certain time it falls below the background signal mostly induced by dark counts and after roughly 100 ns the waveform ends which cuts the necessary informations needed for the third component short. The second reason are the irregularities explained before. Combining the fit results of all channels gives decay times of:

$$\tau_0 = (3.89 \pm 0.18)\ \text{ns}, \quad \tau_1 = (10.12 \pm 0.44)\ \text{ns}, \quad \tau_2 = (127.4 \pm 77.06)\ \text{ns} \quad , \tag{7.6}$$

for SiPMs without light guides and

$$\tau_0 = (3.83 \pm 0.27)\ \text{ns}, \quad \tau_1 = (10.07 \pm 0.4)\ \text{ns}, \quad \tau_2 = (98.1 \pm 49.81)\ \text{ns} \quad , \tag{7.7}$$

for the SiPMs with PLCs. This clearly shows the issues for the third component with a large decay time. Within error bars the values are comparable and no noticeable effect of the passive light collectors on the timing can be seen. A fit of the LAB based sample with equation 7.5 and $N = 2$ for $\mathrm{S}(t)$ (equation 7.3) did not yield successful fit results confirming the approach above.

The second sample that was measured and analysed is the WbLS. Similar to the LAB based sample the WbLS time residuals have been determined and binned in terms of the device time resolution and afterwards normalized to 1. The data is then fitted again with the model described in equation 7.5 but with two exponential decays instead of three. The results of this can be seen in figure 7.5 for SiPM without light collectors and in figure 7.6 for SiPM with PLCs. Similar to before the results for the decay times τ_i, the reduced normalisation factors n_i and the rise time τ_R can be seen in table 7.3 and 7.4 respectively. Again combining the results for the different channels gives

$$\tau_0 = (1.75 \pm 0.11)\ \text{ns}, \quad \tau_1 = (7.39 \pm 1.04)\ \text{ns} \quad , \tag{7.8}$$

for SiPMs without light guides and

$$\tau_0 = (1.81 \pm 0.19)\ \text{ns}, \quad \tau_1 = (5.51 \pm 0.87)\ \text{ns} \quad , \tag{7.9}$$

for SiPMs with PLCs. Both the fast and the slow component could be well determined and within the error bars the values are again comparable. Similar to the LAB based sample no effect of the passive light collectors on the timing can be seen.

7.4 Scintillator time profiles using SiPMs with ALC

Lastly the SiLC modules using ALCs are used to measure the scintillator samples. As only two ALCs are available the two central SiPM were outfitted with the ALCs and the results are shown for these channels. The time residuals have been determined and binned in terms of the time resolution of the SiPMs and afterwards normalized to 1. The data is then fitted with the model described in equation 7.5 similar to before. The results can be seen in figure 7.7 for the LAB based scintillator and in 7.8 for the WbLS. The results for the decay times and normalisation factors as well as the results for the rise time τ_R are shown in table 7.5 and 7.6 Combined this results in

$$\tau_0 = (3.77 \pm 0.16)\ \text{ns}, \quad \tau_1 = (10.41 \pm 1.39)\ \text{ns}, \quad \tau_2 = (100.8 \pm 62.93)\ \text{ns} \quad , \tag{7.10}$$

for the LAB-PPO-bis-MSB scintillator and

$$\tau_0 = (2.36 \pm 0.09)\ \text{ns}, \quad \tau_1 = (5.5 \pm 0.62)\ \text{ns} \quad , \tag{7.11}$$

for the WbLS. What can be taken from these results compared to the results of the measurements without light collector and with PLCs is an increase in the short decay time of the WbLS. The decay time of the LAB based sample is comparable within error bars. The reason for the longer decay time is the additional absorption and re-emission of the light produced by the WbLS. The PPO emission spectrum matches the absorption spectrum of the bis-MSB of the ALCs. For the emission from the LAB based scintillator the ALC acts passive as no more absorption and re-emission is possible.

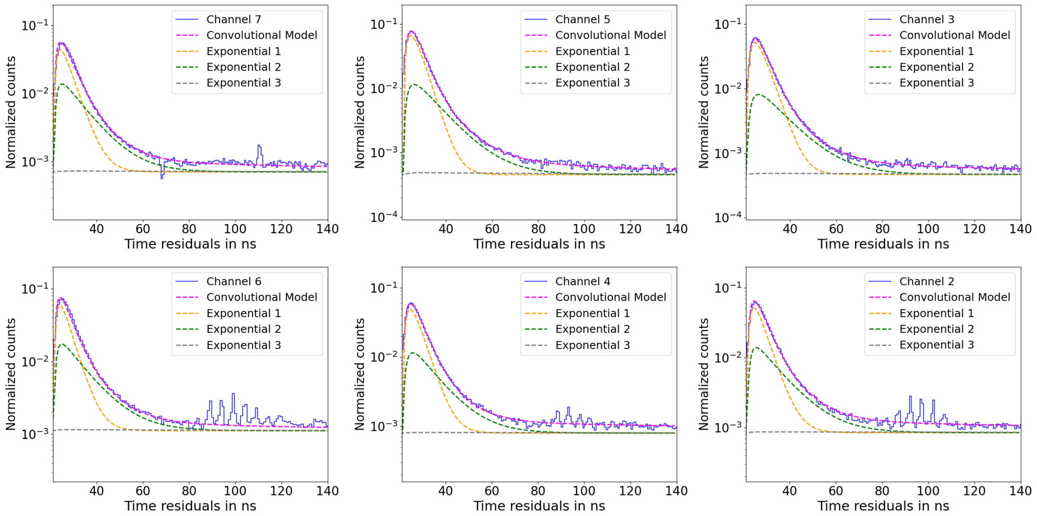

Figure 7.3: Distribution of time residuals for the LAB+PPO+bis-MSB scintillator and SiPMs without light collectors. Shown are all six available channels as they are physically placed on the main board. The distribution has been normalized to 1 and binned in regards to the time resolution of the SiPM. Blue bars shows the time residual data while the magenta dashed line shows the full fitted model described in equation 7.5 for $N = 3$ for $\mathrm{S}(t)$ (equation 7.3) as well as Gaussian detector response. The orange, green and grey dashed lines show the three exponential decay functions as described in equation 7.3 separately.

Table 7.1: Fit results for the LAB+PPO+bis-MSB scintillator time profile and SiPM with no light collectors to determine the decay times. The distribution was fitted with the model described in equation 7.5 for $N = 3$ for $\mathrm{S}(t)$ (equation 7.3). The results of the normalization factors and the decay times are shown for each of the six channel together with their standard deviation as error.

	τ_0 [ns]	τ_1 [ns]	τ_2 [ns]	τ_R [ns]
Channel 2	4.18±1.47	10.37±5.97	168.79±404.92	1.49±0.35
Channel 3	3.69±1.65	10.79±6.15	114.41±244.56	2.44±0.9
Channel 4	3.87±1.94	9.65±6.59	174.57±389.06	1.96±0.7
Channel 5	3.47±1.99	10.36±6.59	85.14±191.25	2.17±1.15
Channel 6	3.97±1.65	10.06±6.97	94.48±282.64	1.31±0.34
Channel 7	4.15±1.67	9.48±5.66	127.12±259.86	1.5±0.31

	n_0	n_1	n_2
Channel 2	0.2285±0.1144	0.1121±0.1041	0.0024±0.002
Channel 3	0.2544±0.0644	0.076±0.0562	0.0015±0.0017
Channel 4	0.316±0.1695	0.1305±0.1583	0.0027±0.0019
Channel 5	0.3666±0.113	0.1244±0.0981	0.0023±0.004
Channel 6	0.5236±0.3216	0.284±0.283	0.0048±0.0105
Channel 7	0.3742±0.2492	0.2041±0.233	0.0034±0.0032

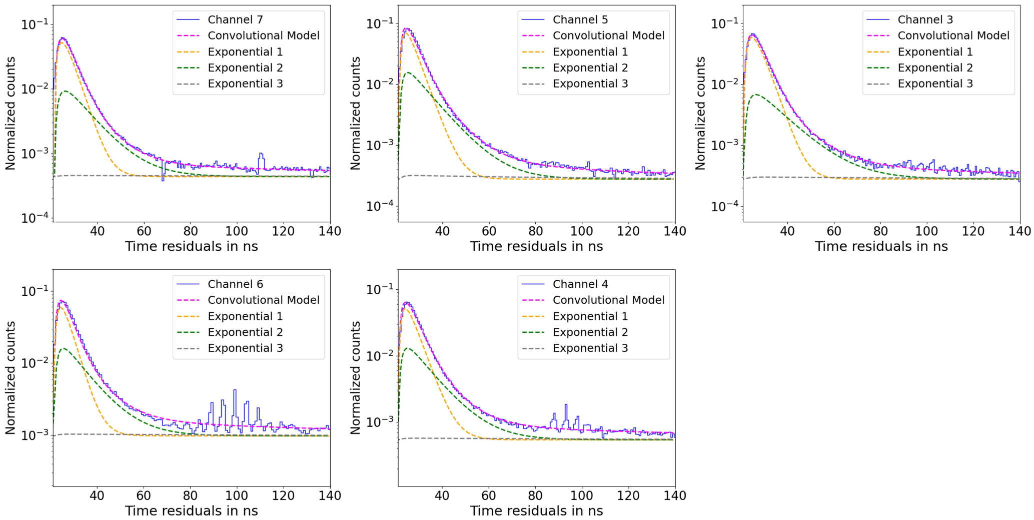

Figure 7.4: Distribution of time residuals for the LAB+PPO+bis-MSB scintillator and SiPMs with passive light collectors. Shown are five channels which were outfitted with passive light collectors. They are physically placed as on the main board. The distribution has been normalized to 1 and binned in regards to the time resolution of the SiPM. Blue bars shows the time residual data while the magenta dashed line shows the full fitted model described in equation 7.5 for $N = 3$ for $\mathrm{S}(t)$ (equation 7.3) as well as Gaussian detector response. The orange, green and grey dashed lines show the three exponential decay functions as described in equation 7.3 separately.

Table 7.2: Fit results for the LAB+PPO+bis-MSB scintillator time profile and SiPM with passive light collectors to determine the decay times. The distribution was fitted with the model described in equation 7.5 for $N = 3$ for $\mathrm{S}(t)$ (equation 7.3). The results of the normalization factors and the decay times are shown for each of the six channel together with their standard deviation as error.

	τ_0 [ns]	τ_1 [ns]	τ_2 [ns]	τ_R [ns]
Channel 3	3.65±1.43	11.56±6.88	94.27±231.86	2.46±0.86
Channel 4	4.29±1.70	9.79±6.87	107.35±185.53	1.69±0.36
Channel 5	4±1.35	9.52±5.78	68.38±125.83	1.53±0.33
Channel 6	3.65±1.98	9.74±6.66	102.98±155.42	1.8±0.65
Channel 7	3.58±1.98	9.72±6.49	117.47±263.13	2.22±1.01

	n_0	n_1	n_2
Channel 3	0.2886±0.0530	0.0678±0.0434	0.0013±0.0025
Channel 4	0.3399±0.2141	0.1481±0.1996	0.0031±0.0027
Channel 5	0.3704±0.1782	0.15±0.1634	0.0022±0.004
Channel 6	0.5501±0.3066	0.2739±0.2746	0.0079±0.006
Channel 7	0.4731±0.1777	0.1544±0.1633	0.0026±0.0028

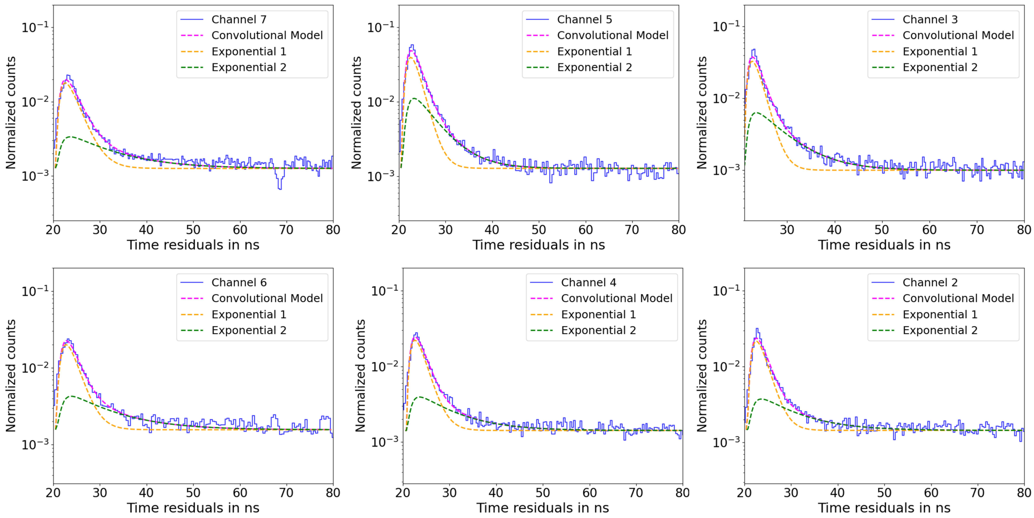

Figure 7.5: Distribution of time residuals for the WbLS and SiPMs without light collectors. Shown are all six available channels as they are physically placed on the main board. The distribution has been normalized to 1 and binned in regards to the time resolution of the SiPM. Blue bars shows the time residual data while the magenta dashed line shows the full fitted model described in equation 7.5 for $N = 2$ for $\mathrm{S}(t)$ (equation 7.3) as well as Gaussian detector response. The orange and green dashed lines show the two exponential decay functions as described in equation 7.3 separately.

Table 7.3: Fit results for the WbLS time profile and SiPM with no light collectors to determine the decay times. The distribution was fitted with the model described in equation 7.5 for $N = 2$ for $\mathrm{S}(t)$ (equation 7.3). The results of the normalization factors and the decay times are shown for each of the six channel together with their standard deviation as error.

	τ_0 [ns]	τ_1 [ns]	τ_R [ns]
Channel 2	1.62±0.60	7.79±2.66	1.05±0.40
Channel 3	1.47±0.56	5.99±1.35	0.96±0.37
Channel 4	1.73±0.55	7.56±2.51	0.98±0.36
Channel 5	1.49±0.77	4.53±1.14	0.97±0.46
Channel 6	1.94±0.84	9.11±3.99	1.00±0.53
Channel 7	2.24±0.58	9.34±3.52	1.07±0.31

	n_0	n_1
Channel 2	0.0342±0.0035	0.0109±0.0031
Channel 3	0.0511±0.0056	0.0212±0.0052
Channel 4	0.0363±0.0041	0.0119±0.0037
Channel 5	0.0531±0.0111	0.0267±0.0108
Channel 6	0.0318±0.0053	0.0133±0.0046
Channel 7	0.0299±0.0040	0.0103±0.0036

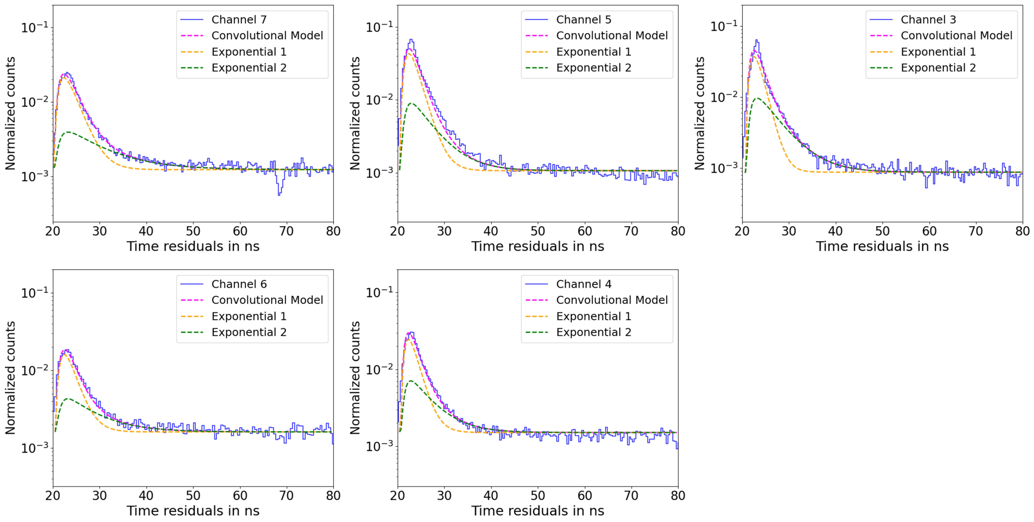

Figure 7.6: Distribution of time residuals for the WbLS and SiPMs with passive light collectors. Shown are five channels which were outfitted with passive light collectors. They are physically placed as on the main board. The distribution has been normalized to 1 and binned in regards to the time resolution of the SiPM. Blue bars shows the time residual data while the magenta dashed line shows the full fitted model described in equation 7.5 for $N = 2$ for $\mathrm{S}(t)$ (equation 7.3) as well as Gaussian detector response. The orange and green dashed lines show the two exponential decay functions as described in equation 7.3 separately.

Table 7.4: Fit results for the WbLS time profile and SiPM with passive light collectors to determine the decay times. The distribution was fitted with the model described in equation 7.5 for $N = 2$ for $\mathrm{S}(t)$ (equation 7.3). The results of the normalization factors and the decay times are shown for each of the six channel together with their standard deviation as error.

	τ_0 [ns]	τ_1 [ns]	τ_R [ns]
Channel 3	1.36±0.82	4.50±1.16	0.92±0.52
Channel 4	1.70±0.84	4.53±2.42	0.73±0.28
Channel 5	1.79±0.65	4.34±2.06	0.78±0.25
Channel 6	1.98±0.99	6.37±3.86	0.84±0.50
Channel 7	2.23±0.45	7.82±2.32	1.10±0.21

	n_0	n_1
Channel 3	0.0548±0.0105	0.0276±0.0103
Channel 4	0.0357±0.0176	0.0165±0.0172
Channel 5	0.059±0.0225	0.0196±0.0223
Channel 6	0.0239±0.0086	0.0098±0.0084
Channel 7	0.0359±0.0046	0.0115±0.0042

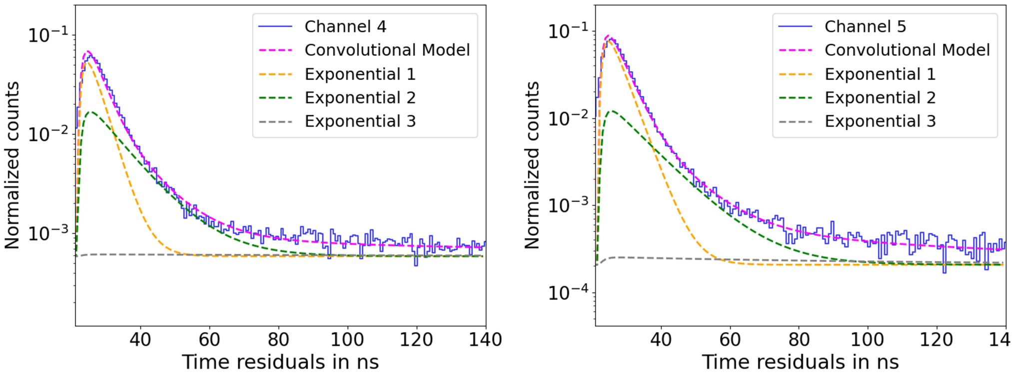

Figure 7.7: Distribution of time residuals for the LAB+PPO+bis-MSB scintillator and SiPMs with active light collectors. Shown are two channels which were outfitted with active light collectors. The distribution has been normalized to 1 and binned in regards to the time resolution of the SiPM. Blue bars shows the time residual data while the magenta dashed line shows the full fitted model described in equation 7.5 for $N = 3$ for $S(t)$ (equation 7.3) as well as Gaussian detector response. The orange, green and grey dashed lines show the three exponential decay functions as described in equation 7.3 separately.

Table 7.5: Fit results for the LAB+PPO+bis-MSB scintillator time profile and SiPM with active light collectors to determine the decay times. The distribution was fitted with the model described in equation 7.5 for $N = 3$ for $S(t)$ (equation 7.3). The results of the normalization factors and the decay times are shown for each of the six channel together with their standard deviation as error.

	τ_0 [ns]	τ_1 [ns]	τ_2 [ns]	τ_R [ns]
Channel 4	3.56±1.38	10.02±4.18	118.3±299.11	1.47±0.41
Channel 5	3.97±1.07	10.79±6.96	83.21±173.25	1.35±0.33

	n_0	n_1	n_2
Channel 4	0.2967±0.1194	0.1900±0.1049	0.0026±0.004
Channel 5	0.3915±0.1256	0.1248±0.1084	0.0028±0.0049

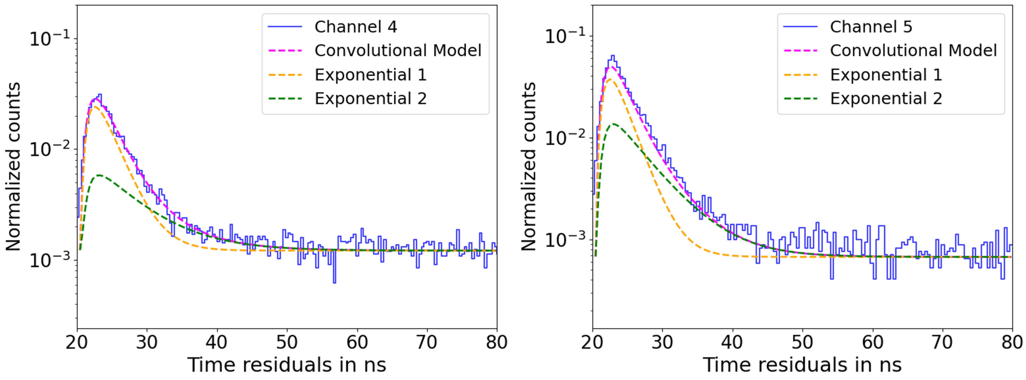

Figure 7.8: Distribution of time residuals for the WbLS and SiPMs with active light collectors. Shown are two channels which were outfitted with active light collectors. The distribution has been normalized to 1 and binned in regards to the time resolution of the SiPM. Blue bars shows the time residual data while the magenta dashed line shows the full fitted model described in equation 7.5 for $N = 2$ for $S(t)$ (equation 7.3) as well as Gaussian detector response. The orange and green dashed lines show the two exponential decay functions as described in equation 7.3 separately.

Table 7.6: Fit results for the WbLS time profile and SiPM with active light collectors to determine the decay times. The distribution was fitted with the model described in equation 7.5 for $N = 2$ for $S(t)$ (equation 7.3). The results of the normalization factors and the decay times are shown for each of the six channel together with their standard deviation as error.

	τ_0 [ns]	τ_1 [ns]	τ_R [ns]
Channel 4	2.53±0.81	6.14±3.11	0.97±0.24
Channel 5	2.18±0.99	4.85±1.88	0.81±0.28

	n_0	n_1
Channel 4	0.0532±0.022	0.0198±0.0215
Channel 5	0.0595±0.0367	0.0356±0.0363

7.5 Effect of active and passive light collectors on the light collection efficiency of SiLC modules

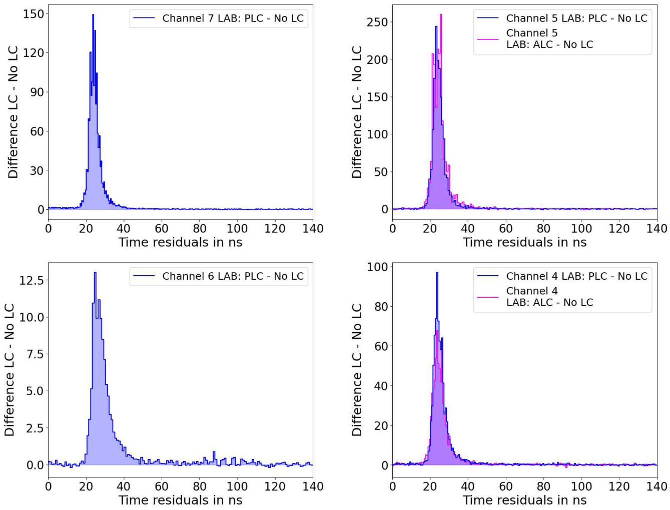

Figure 7.9: Differences calculated from the LAB-PPO-bis-MSB time residual distributions in figure 7.3, 7.4, 7.7. For this the distributions were normalized to their background level. The five differences between no light collectors and PLCs are shown as well as the two differences between no light collectors and ALCs. A positive value represents the SiPM with light collector having seen more light while negative value represents the SiPM without light collector having seen more light.

To conclude this chapter it is worthwhile to take a look at the differences in time profiles between the measurements with no light collectors and the measurements with either PLCs or ALCs. For each SiPM the difference is calculated between the time residual distribution of the SiPM with a light collector and the SiPM with no light collector, as LC - no LC. The time residual distributions for each SiPM use the same amount of events and are binned in the same way. Afterwards they are normalized to their respective backgrounds to account for the different background levels, which make it difficult to give results on an absolute scale.

Figure 7.9 shows these differences for the LAB-PPO-bis-MSB scintillator and SiPM equipped with both PLCs and ALCs. Positive values represent a higher relative value, above the background, for SiPM with light collectors compared to SiPM without light collectors, while negative values represent a higher relative value for SiPM without light collectors compared to SiPM with light collectors. Thus a positive value can be interpreted as an increase in detected photons, for the respective time bins, with the use of a light collector. What can be overall seen is that both light collector types show a lot of large positive values between 20 ns and 40 ns. As this coincides with the region of interest for the LAB based scintillators emission time profile, it indicates an increase in the amount of detected photos as predicted by the simulations in chapter 6.2. Outside of this time frame is mostly dominated by statistical fluctuation around zero with the only exception being channel 6 which replicates the irregularity shown in figure 7.3 and 7.4 as they are the strongest in this channel. The two central channels, channel 4 and 5, show the differences in the time profiles for SiPM with ALCs and compared to the differences for SiPM with PLCs show no notable difference as expected for this scintillator composition. Since the WLS in the ALC and the secondary WLS in the liquid scintillator are bis-MSB a re-absorption of the photons, emitted by liquid scintillator, by the ALC is not possible.

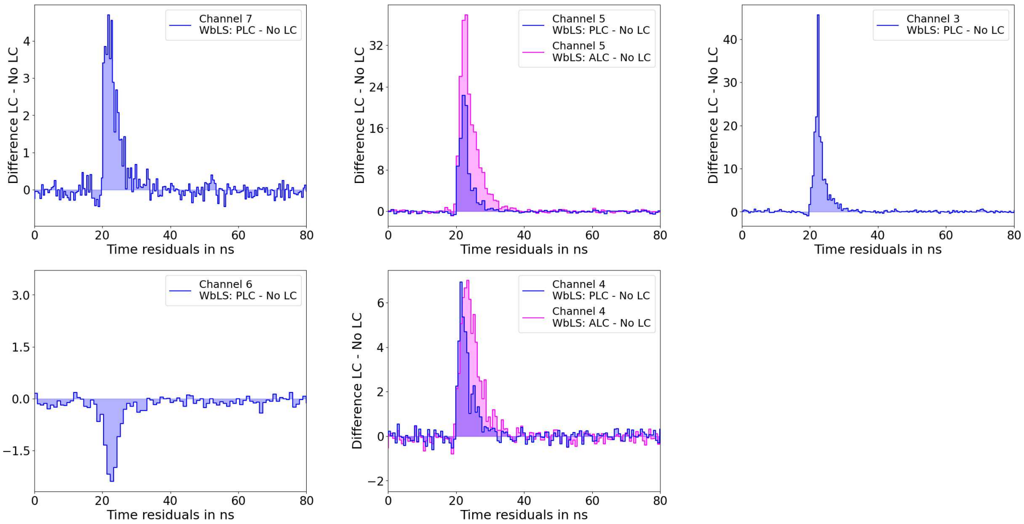

Figure 7.10: Differences calculated from the WbLS time residual distributions in figure 7.5, 7.6, 7.8. For this the distributions were normalized to their background level. The five differences between no light collectors and PLCs are shown as well as the two differences between no light collectors and ALCs. A positive value represents the SiPM with light collector having seen more light while negative value represents the SiPM without light collector having seen more light.

Figure 7.10 shows the differences for the WbLS and SiPM equipped with both PLCs and ALCs. Similar to before a lot of positive values can be seen between 20 ns and 40 ns for all channels except channel 6 where the values are negative instead. The overall lower light yield of the WbLS, which is visible in all channels, compared to the high light yield LAB based scintillator, and the position of the SiPM on the furthest edge of the array could explain this behaviour. Considering the low difference value of channel 6 of the LAB based scintillator compared with the other channels of the same plot a geometrical issue is not negligible. What is also visible is that the ALC adds one more decay time τ due to the abortion and re-emission from the bis-MSB in the ALC. This can also be seen in the results for the determination of the decay times in table 7.3 and 7.4 for no light collectors and passive light collectors and the results for the active light collectors in table 7.6. The fast decay time increases from 1.75 ns and 1.81 ns to 2.36 ns, with no overlap between the respective uncertainty ranges.

Excluding channel 6, which shows a particular behaviour where either a very low positive difference or a negative difference is seen, all other channels show positive difference values indicating an increase in the amount of detected photons. For both, the LAB based scintillator and the WbLS an overall good result is shown and the light collection capabilities of the SiLC modules can be confirmed.

8 | Summary and Outlook

"Everything's got to end sometime. Otherwise, nothing would ever get started."
- Dr Who, 11th Doctor

The improvements and advancements in detector technologies play a vital role in neutrino physics, be it new state of the art detector technologies or a new application for already existing ones. This thesis focused on both aspects by actively pushing the deployment and commissioning of a new technology as well as the development and testing of a new detector design made for high spatial and time resolution.

The Accelerator Neutrino Neutron Interaction Experiment is a water Cherenkov detector using the Booster-Neutrino-Beam to make studies about the final state neutron multiplicity as well as the neutrino cross-section in water. It was designed in a way to make the most out of the incoming neutrino beam and take data for high statistics. But the design was also done in a way where future deployments of R&D technologies are easily doable. One of these technologies are the Large Area Picosecond Photodetectors, a new ultra fast type of photosensor that offers good time resolution as well as spatial resolution. By equipping ANNIE with only five of these detectors the reconstruction capabilities can be improved by a lot. The scope of this thesis goes along the preparation, deployment and commissioning of the first three LAPPDs. Alongside the preparation, which characterised the LAPPDs before deployment, software interfaces were developed to allow for data taking and slow control. With these the custom electronics used by ANNIE, the ACDC boards which house the digitization chips and the ANNIE Central Card which collects data from multiple ACDC boards, could be utilized with the specifications intended for deployment. With a successful characterisation the software interfaces were then adapted to a deployment ready state in which they were successfully integrated into the main ANNIE software environment running for the entire detector. With the software ready, the first ever LAPPD was deployed into a large scale experiment and produced proof that it can see the interactions induced by the neutrino beam. Shortly after, a second and third LAPPD were deployed and a multi-LAPPD readout system was integrated into the software. All three LAPPDs were successfully commissioned and using beam neutrino induced event data, collected from all three LAPPDs, the analysis provided clear multi-LAPPD evidence of the beam's presence.

With the software interfaces ready for multi-LAPPD handling, future deployments of more LAPPDs can start without any hindrances as the developed software interface is easily scalable. Looking to the future and more deployments an aspect that in the end will need attention is the stability of the data system. Currently the data transfer from the ACC happens via an USB connection and a rather old USB chip. To increase the stability of the data transfer a switch to an alternatively available Ethernet interface would be necessary. The ACC is already equipped with an Ethernet interfacing chip which would allow for said switch. In the scope of this thesis an alternative software version using the improved Ethernet interface has already been developed and tested alongside a matching firmware developed by the University of Warwick. Both firmware as well as software have already been tested in a simple bench setup and are ready to be transitioned to match the software interface currently running the LAPPDs in ANNIE. To keep the interference of the change as minimal as possible the change in firmware only impacts the electronics running on the surface and as such can be done without removing the LAPPDs deployed.

During the second part of this thesis the focus shifted from the deployment of existing new detector technologies to the development of a new detector design based on already existing sensors. In this case the combination of SiPMs and scintillators were the main focus. To account for the small size of the SiPMs which in an array of larger size would be a negative aspect, due to the required amount, the approach tries to use the scintillators as light collectors for a significant increase in the photosensitive area. During the development this approach was extended to include passive light collectors made from basic plastic next to active light collectors made from scintillator compositions. The SiPMs were chosen to be ultra fast sensors with a time resolution <1 ns and a new type of output which allows for PMT like pulses without the characteristic recharge tail and the scintillator was designed to be able to match the sensitive wavelength of the SiPM and absorb the light emitted by the most common types of sources present in neutrino physics which would be either Cherenkov light or the light produced by other scintillators. The different components were developed and produced and in the end a specialized test bench was designed to characterise the developed components. Starting with a characterisation of the SiPMs themselves, a new and untested type of sensor, to precision measurements determining the time resolution of the devices which were determined to be in the range of 0.1 ns to 0.6 ns. Afterwards a series of test measurements were done to show the capabilities of the detector design with liquid scintillator samples. For this three sources were chosen, HPLC water for pure Cherenkov radiation, a high light yield liquid scintillator with multiple components based on LAB, PPO and bis-MSB and a new type of liquid scintillator called Water-based-Liquid-Scintillator which has a low light yield and as such serves as a source of Cherenkov radiation as well as scintillation light. To see if the detector design was capable of working with the different sources the decay times of the scintillators were determined and yielded acceptable results that are comparable over the different measurements. Lastly the differences of the time residual distributions were determined showing an increase in the region of interest for the scintillators, indicating an increase in the light collection due to both PLCs and ALCs.

This thesis was capable of showing the basic capabilities of the new detector design and yielded acceptable results but accompanied by a series of caveats. Overall a lot of improvements have to be made in order to make the design viable for actual experimental use. The SiPM by themselves offer a satisfying performance and can offer the attempted sub-nanosecond time resolution as shown during the calibration of the SiPMs. Mainly an improved design of the shuttle boards with an onboard cooling system would be beneficial to decrease the DCR as much as possible. While the current solution works, it cools the devices by roughly 10 to 20 degrees but is dependent on the outside temperature and the cooling system mounted to the darkbox. To make the SiLC array a deployable detector an onboard cooling solution might be necessary. The data acquisition could also be updated to take data with a longer time window. This could be achieved by using a different ADC which has a longer recording time. A change like this would need to be thoroughly tested to make sure the sampling rate is still enough to sample a pulse with enough precision. By lengthening the recorded time window, it will be easier to determine slow decay times of scintillators with more precision. A different aspect that also needs to improve is the design of the light collectors. While they have been designed in a way that yields the intended results the design is fairly basic, similar to the simulations done to determine the shape and size used. A simulation much more detailed and refined to determine the best possible design needs to be set up and improved alongside the production of the scintillators themselves. Lastly an aspect missing from this thesis is the demonstration of the spatial capabilities of an array made of the new detector design. This would include the design of a full eight by eight array of SiPM equipped with light collectors. With this dedicated measurements for the spatial resolution could be done in order to test the array.

Appendix A | CanBus frame structure

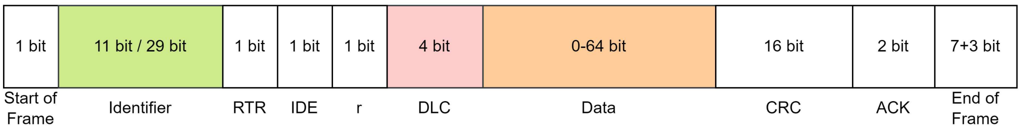

Figure A.1: Illustration of a complete CanBus frame. The green marked bits represent the frame identifier also used to prioritise messages. The red marked bits are the data length code (DLC) bits and the orange marked bits correspond to the data [81].

Table A.1: Important CanBus frame bit descriptions [81].

Name	Length (bits)	Description
Start-of-frame	1	Start of frame transmission
Identifier	11	Unique identifier also used for message priority
(...)		
Data length code (DLC)	4	Number of bytes of data
Data field	0-64	Data to transmit
(...)		
End-of-frame	1	End of frame transmission

Appendix B LAPPD relevant data frames

The LAPPD event data frame

Table B.1: The LAPPD event data frame structure.

Word	Entry (16 bit word)
0	0x1234
1	0xA5EC
2	0xF005 - PSEC chip 0 data startword
3-1538	Channel 0 to Channel 5 data
1539-1552	Metadata info words (see later for more)
1553	0xFACE - PSEC chip 0 data endword
1554	0xF005 - PSEC chip 1 data startword
1555-3090	Channel 0 to Channel 5 data
3091-3104	Metadata info words (see later for more)
3105	0xFACE - PSEC chip 1 data endword
3106	0xF005 - PSEC chip 2 data startword
3107-4642	Channel 0 to Channel 5 data
4643-4656	Metadata info words (see later for more)
4657	0xFACE - PSEC chip 2 data endword
4658	0xF005 - PSEC chip 3 data startword
4659-6194	Channel 0 to Channel 5 data
6195-6208	Metadata info words (see later for more)
6209	0xFACE - PSEC chip 3 data endword
6210	0xF005 - PSEC chip 4 data startword
6211-7746	Channel 0 to Channel 5 data
7747-7760	Metadata info words (see later for more)
7761	0xFACE - PSEC chip 4 data endword
7762-7767	PSEC chip 0, Channel 0-5 Self trigger rate
7768-7773	PSEC chip 1, Channel 0-5 Self trigger rate
7774-7779	PSEC chip 2, Channel 0-5 Self trigger rate
7780-7785	PSEC chip 3, Channel 0-5 Self trigger rate
7786-7791	PSEC chip 4, Channel 0-5 Self trigger rate
7792	Combined trigger rate
7793	0xA5EC
7794	0x4321

The PPS frame

Table B.2: The PPS frame structure.

Word	Entry (16 bit word)
0	0x1234
1	0xEEEE
2	PPS timestamp bit[63:48]
3	PPS timestamp bit[47:32]
4	PPS timestamp bit[31:16]
5	PPS timestamp bit[15:0]
6	PPS serialnumber bit[31:16]
7	PPS serialnumber bit[15:0]
8	PPS count bit[31:16]
9	PPS count bit[15:0]
10-13	0x0000
14	0xEEEE
15	0x4321

The extracted metadata from the LAPPD event data frame

Table B.3: The extracted metadata from the LAPPD event data frame structure part 1

Word	What it is	Relevant bits	Data frame position
0	Board ID, refers to the port on the ACC	16	-
1	PSEC ID for PSEC chip 0 (0xDCB0)	16	-
2	Wilkinson feedback count (current)	16	1540
3	Wilkinson feedback target count setting	16	1541
4	Vbias (pedestal) value setting	16	1542
5	Self trigger threshold value setting	16	1543
6	PROVDD parameter setting	16	1544
7	Trigger info 0, Beamgate timestamp[63:48]	16	1545
8	Trigger info 1, Selftrigger mask PSEC 0	16	1546
9	Trigger info 2, Selftrigger threshold PSEC 0	16	1547
10	PSEC0 timestamp [15:0]	16	1548
.	Clockcycle bit	3	
11	PSEC0 event count [15:0]	16	1549
12	VCDL count [15:0]	16	1550
13	VCDL count [31:16]	16	1551
14	DLLVDD parameter setting	16	1552
15	PSEC0-ch0 Self trig rate counts	16	7762
16	PSEC0-ch1 Self trig rate counts	16	7763
17	PSEC0-ch2 Self trig rate counts	16	7764
18	PSEC0-ch3 Self trig rate counts	16	7765
19	PSEC0-ch4 Self trig rate counts	16	7766
20	PSEC0-ch5 Self trig rate counts	16	7767
21	PSEC ID for PSEC chip 1 (0xDCB1)	16	-
22	Wilkinson feedback count (current)	16	3092
23	Wilkinson feedback target count setting	16	3093
24	Vbias (pedestal) value setting	16	3094
25	Self trigger threshold value setting	16	3095
26	PROVDD parameter setting	16	3096
27	Trigger info 0, Beamgate timestamp[47:32]	16	3097
28	Trigger info 1, Selftrigger mask PSEC 1	16	3098
29	Trigger info 2, Selftrigger threshold PSEC 1	16	3099
30	PSEC1 timestamp [31:16]	16	3100
31	PSEC1 event count [31:16]	16	3101
32	VCDL count [15:0]	16	3102
33	VCDL count [31:16]	16	3103
34	DLLVDD parameter setting	16	3104
35	PSEC1-ch0 Self trig rate counts	16	7768
36	PSEC1-ch1 Self trig rate counts	16	7769
37	PSEC1-ch2 Self trig rate counts	16	7770
38	PSEC1-ch3 Self trig rate counts	16	7771
39	PSEC1-ch4 Self trig rate counts	16	7772

Table B.4: The extracted metadata from the LAPPD event data frame structure part 2

Word	What it is	Relevant bits	Data frame position
40	PSEC1-ch5 Self trig rate counts	16	7773
41	PSEC ID for PSEC chip 2 (0xDCB2)	16	-
42	Wilkinson feedback count (current)	16	4644
43	Wilkinson feedback target count setting	16	4645
44	Vbias (pedestal) value setting	16	4646
45	Self trigger threshold value setting	16	4647
46	PROVDD parameter setting	16	4648
47	Trigger info 0, Beamgate timestamp[31:16]	16	4649
48	Trigger info 1, Selftrigger mask PSEC 2	16	4650
49	Trigger info 2, Selftrigger threshold PSEC 2	16	4651
50	PSEC2 timestamp [47:32]	16	4652
51	0	0	-
52	VCDL count [15:0]	16	4654
53	VCDL count [31:16]	16	4655
54	DLLVDD parameter setting	16	4656
55	PSEC2-ch0 Self trig rate counts	16	7774
56	PSEC2-ch1 Self trig rate counts	16	7775
57	PSEC2-ch2 Self trig rate counts	16	7776
58	PSEC2-ch3 Self trig rate counts	16	7777
59	PSEC2-ch4 Self trig rate counts	16	7778
60	PSEC2-ch5 Self trig rate counts	16	7779
61	PSEC ID for PSEC chip 3 (0xDCB3)	16	-
62	Wilkinson feedback count (current)	16	6196
63	Wilkinson feedback target count setting	16	6197
64	Vbias (pedestal) value setting	16	6198
65	Self trigger threshold value setting	16	6199
66	PROVDD parameter setting	16	6200
67	Trigger info 0, Beamgate timestamp[15:0]	16	6201
68	Trigger info 1, Selftrigger mask PSEC 3	16	6202
69	Trigger info 2, Selftrigger threshold PSEC 3	16	6203
70	PSEC3 timestamp [63:48]	16	6204
71	0	0	-
72	VCDL count [15:0]	16	6026
73	VCDL count [31:16]	16	6207
74	DLLVDD parameter setting	16	6208
75	PSEC3-ch0 Self trig rate counts	16	7780
76	PSEC3-ch1 Self trig rate counts	16	7781
77	PSEC3-ch2 Self trig rate counts	16	7782
78	PSEC3-ch3 Self trig rate counts	16	7783
79	PSEC3-ch4 Self trig rate counts	16	7784

Table B.5: The extracted metadata from the LAPPD event data frame structure part 3

Word	What it is	Relevant bits	Data frame position
80	PSEC3-ch5 Self trig rate counts	16	7785
81	PSEC ID for PSEC chip 4 (0xDCB4)	16	-
82	Wilkinson feedback count (current)	16	7748
83	Wilkinson feedback target count setting	16	7749
84	Vbias (pedestal) value setting	16	7750
85	Self trigger threshold value setting	16	7751
86	PROVDD parameter setting	16	7752
87	Trigger info 0	see below	7753
.	Trigger setup mode	[15:12]	
.	SMA invert setting	[11]	
.	Selftrigger sign	[10]	
.	Selftrigger coincidence minimum	[9:0]	
88	Trigger info 1, Selftrigger mask PSEC 4	16	7754
89	Trigger info 2, Selftrigger threshold PSEC 4	16	7755
90	0	0	-
91	0	0	-
92	VCDL count [15:0]	16	7758
93	VCDL count [31:16]	16	7759
94	DLLVDD parameter setting	16	7760
95	PSEC4-ch0 Self trig rate counts	16	7786
96	PSEC4-ch1 Self trig rate counts	16	7787
97	PSEC4-ch2 Self trig rate counts	16	7788
98	PSEC4-ch3 Self trig rate counts	16	7789
99	PSEC4-ch4 Self trig rate counts	16	7790
100	PSEC4-ch5 Self trig rate counts	16	7791
101	Combined trigger rate count	16	7792
102	Endword 0xeeee	0	-

Appendix C Waveforms before pedestal correction

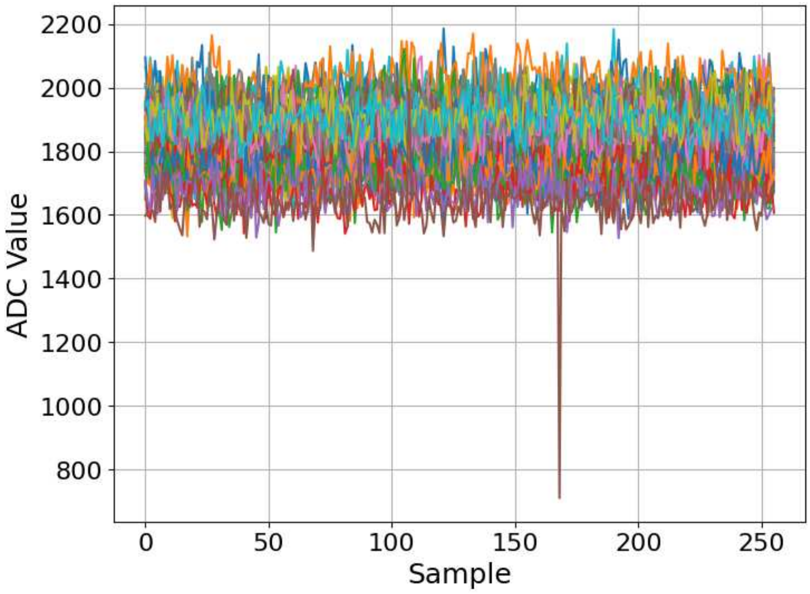

Figure C.1: LAPPD waveforms before pedestal correction described in chapter 5.4.2. Shown are all 56 channels with each waveform having 256 samples digitized at a sampling rate of 10 Gs/s correspond to 25.6 ns.

Appendix D | Additional SiLC simulations

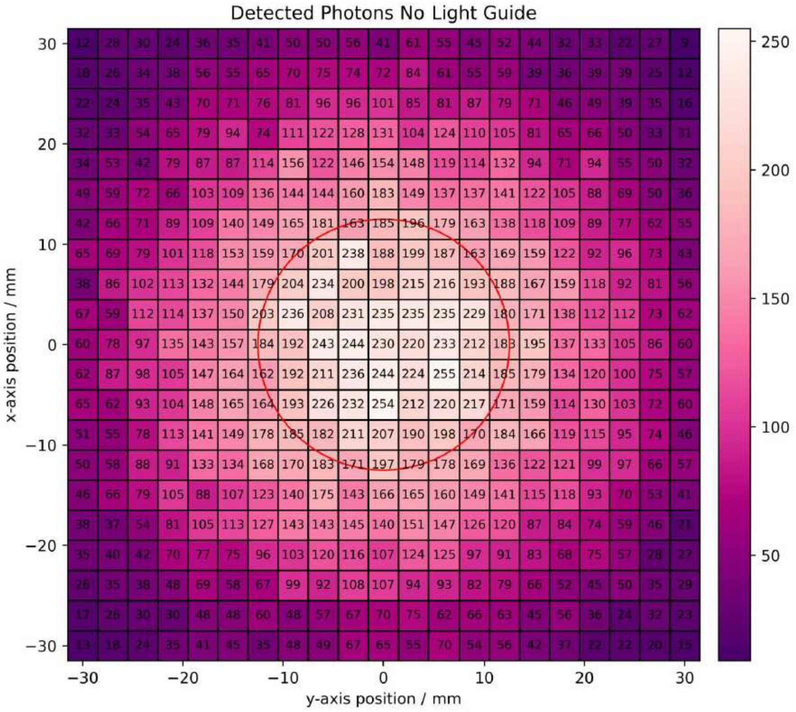

12	28	30	24	36	35	41	50	50	56	41	61	55	45	52	44	32	33	22	27	9
18	26	34	38	56	55	65	70	75	74	72	84	61	55	59	39	36	39	39	25	12
22	24	35	43	70	71	76	81	96	96	101	85	81	87	79	71	46	49	39	35	16
32	33	54	65	79	94	74	111	122	128	131	104	124	110	105	81	65	66	50	33	31
34	53	42	79	87	87	114	156	122	146	154	148	119	114	132	94	71	94	55	50	32
49	59	72	66	103	109	136	144	144	160	183	149	137	137	141	122	105	88	69	50	36
42	66	71	89	109	140	149	165	181	163	185	196	179	163	138	118	109	89	77	62	55
65	69	79	101	118	153	159	170	201	238	188	199	187	163	169	159	122	92	96	73	43
38	86	102	113	132	144	179	204	234	200	198	215	216	193	188	167	159	118	92	81	56
67	59	112	114	137	150	203	236	208	231	235	235	235	229	180	171	138	112	112	73	62
60	78	97	135	143	157	184	192	243	244	230	220	233	212	183	195	137	133	105	86	60
62	87	98	105	147	164	162	192	211	236	244	224	255	214	185	179	134	120	100	75	57
65	62	93	104	148	165	164	193	226	232	254	212	220	217	171	159	114	130	103	72	60
51	55	78	113	141	149	178	185	182	211	207	190	198	170	184	166	119	115	95	74	46
50	58	88	91	133	134	168	170	183	171	197	179	178	169	136	122	121	99	97	66	57
46	66	79	105	88	107	123	140	175	143	166	165	160	149	141	115	118	93	70	53	41
38	37	54	81	105	113	127	143	143	145	140	151	147	126	120	87	84	74	59	46	21
35	40	42	70	77	75	96	103	120	116	107	124	125	97	91	83	68	75	57	28	27
26	35	38	48	69	58	67	99	92	108	107	94	93	82	79	66	52	45	50	35	29
17	26	30	30	48	48	60	48	57	67	70	75	62	66	63	45	56	36	24	32	23
13	18	24	35	41	45	35	48	49	67	65	55	70	54	56	42	37	22	22	20	15

Figure D.1: In-depth simulations for no light collector connected to the SiPM. A x,y-scan was performed for light source positions in the range of −30 mm to 30 mm in 3 mm steps. Each square represents the amount of detected photons on the SiPM at that position [68].

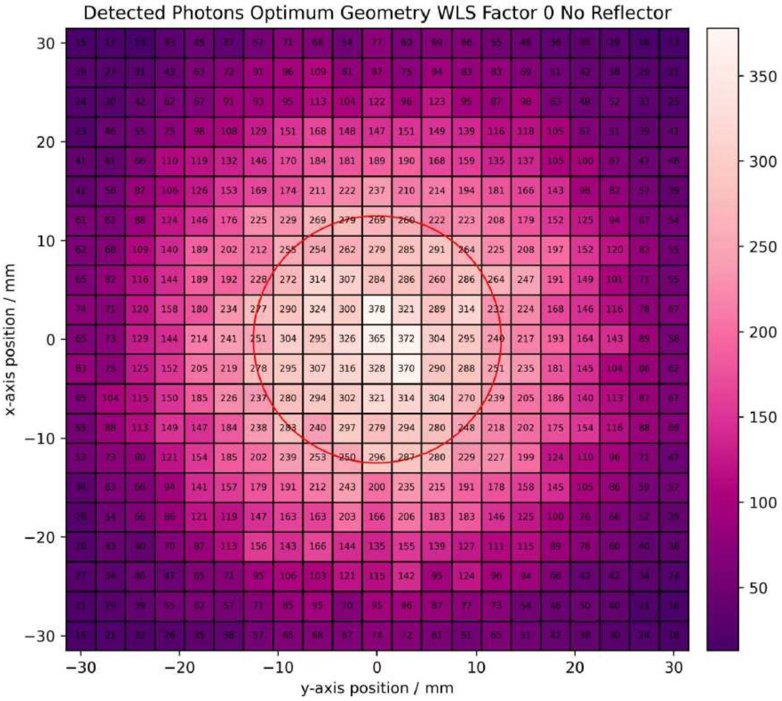

Figure D.2: In-depth simulations for a PLC connected to the SiPM but without reflective surfaces on the walls of the PLC cone part. A x,y-scan was performed for light source positions in the range of $-30\,\mathrm{mm}$ to $30\,\mathrm{mm}$ in $3\,\mathrm{mm}$ steps. Each square represents the amount of detected photons on the SiPM at that position [68].

Appendix E

Bias and readout circuits for SiPM

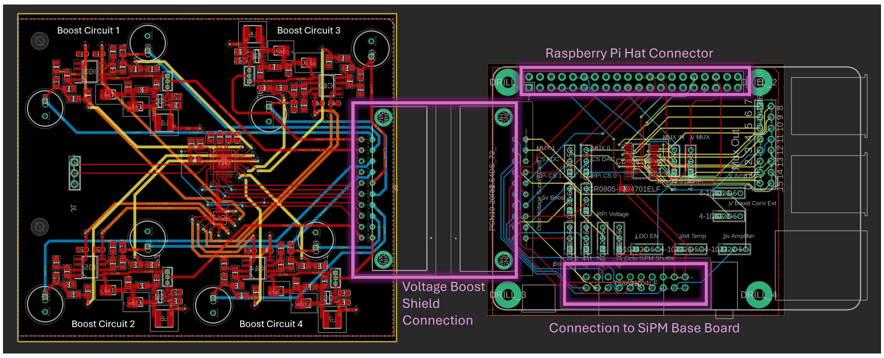

Figure E.1: PCB of the voltage control RPi hat and voltage boost extension. Highlighted are the connections to the other boards and the RPi. Developed by [68].

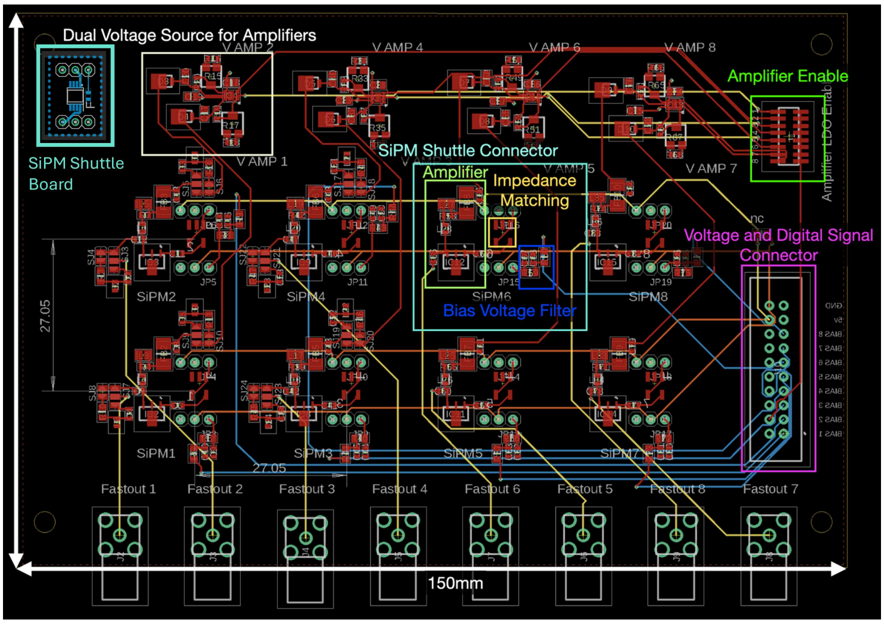

Figure E.2: PCB design for the SiPM master PCB and the SiPM shuttle boards. Highlighted are the connections to the voltage control board as well as all special aspects of the master PCB including the amplifier, the impedance matching and the bias filter. Developed by [68].

Bibliography

[1] W. Pauli: Offener Brief an die Gruppe der Radioaktiven bei der Gauvereins-Tagung zu Tübingen, 1930, `https://cds.cern.ch/record/83282/files/meitner_0393.pdf`.

[2] F. Reines, C. L. Cowan *et al.*: Detection of the Free Antineutrino, *Phys. Rev.*, volume 117, Jan 1960, 159, URL `https://link.aps.org/doi/10.1103/PhysRev.117.159`.

[3] M. G. Aartsen, R. Abbasi *et al.*: First Observation of PeV-Energy Neutrinos with IceCube, *Physical Review Letters*, volume 111, no. 2, Juli 2013, URL `http://dx.doi.org/10.1103/PhysRevLett.111.021103`.

[4] C. Spiering: Towards high-energy neutrino astronomy: A historical review, *The European Physical Journal H*, volume 37, no. 3, Juli 2012, 515–565, URL `http://dx.doi.org/10.1140/epjh/e2012-30014-2`.

[5] J. Alvey, M. Escudero *et al.*: Cosmic neutrino background detection in large-neutrino-mass cosmologies, *Phys. Rev. D*, volume 105, Mar 2022, 063501, URL `https://link.aps.org/doi/10.1103/PhysRevD.105.063501`.

[6] M. Redchuk: Solar neutrino analysis with the Borexino detector, *Journal of Physics: Conference Series*, volume 1056, 07 2018, 012050, URL `https://dx.doi.org/10.1088/1742-6596/1056/1/012050`.

[7] G. Bellini, A. Ianni *et al.*: Geo-neutrinos, *Progress in Particle and Nuclear Physics*, volume 73, 2013, 1, URL `https://www.sciencedirect.com/science/article/pii/S0146641013000732`.

[8] S. Navas *et al.*: Review of particle physics, *Phys. Rev. D*, volume 110, no. 3, 2024, URL `https://link.aps.org/doi/10.1103/PhysRevD.110.030001`.

[9] The IceCube Collaboration: The IceCube Collaboration: contributions to the 30th International Cosmic Ray Conference (ICRC 2007), 2007, URL `https://arxiv.org/abs/0711.0353`.

[10] F. Nakanishi, S. Izumiyama *et al.*: Supernova Burst and Diffuse Supernova Neutrino Background Simulator for Water Cherenkov Detectors, *The Astrophysical Journal*, volume 965, no. 1, apr 2024, 91, URL `https://dx.doi.org/10.3847/1538-4357/ad344e`.

[11] K. Abe, C. Bronner *et al.*: Diffuse supernova neutrino background search at Super-Kamiokande, *Phys. Rev. D*, volume 104, Dec 2021, URL `https://link.aps.org/doi/10.1103/PhysRevD.104.122002`.

[12] R. Aloisio, D. Boncioli *et al.*: Cosmogenic neutrinos and ultra-high energy cosmic ray models, *Journal of Cosmology and Astroparticle Physics*, volume 2015, no. 10, oct 2015, 006, URL `https://dx.doi.org/10.1088/1475-7516/2015/10/006`.

[13] Z. Chen: Latest results from Daya Bay using the full dataset, 2023, URL `https://arxiv.org/abs/2309.05989`.

[14] J. A. Formaggio and G. P. Zeller: From ev to Eev: Neutrino cross sections across energy scales, *Rev. Mod. Phys.*, volume 84, Sep 2012, 1307, URL `https://link.aps.org/doi/10.1103/RevModPhys.84.1307`.

[15] I. Anghel, J. F. Beacom *et al.*: Letter of Intent: The Accelerator Neutrino Neutron Interaction Experiment (ANNIE), 2015, URL `https://arxiv.org/abs/1504.01480`.

[16] D. S. Ayres *et al.*: The NOvA Technical Design Report, 10 2007, URL `https://www.osti.gov/biblio/935497`.

[17] B. Abi, R. Acciarri *et al.*: Deep Underground Neutrino Experiment (DUNE), Far Detector Technical Design Report, Volume I: Introduction to Dune, 2020, URL `https://arxiv.org/abs/2002.02967`.

[18] Hyper-Kamiokande Proto-Collaboration, K. Abe *et al.*: Hyper-Kamiokande Design Report, 2018, URL `https://arxiv.org/abs/1805.04163`.

[19] Stephen Dolan: Neutrino Interactions, *International Neutrino Summer School* 2021 *(INSS)*, `https://indico.cern.ch/event/1011452/contributions/4448411/attachments/2291131/3895428/sDolanNuXSec_part2.pdf`.

[20] M. Breisch: Investigation of SiPM based light detectors for the next generation of neutrino experiments, Master's thesis, Eberhard Karls Universität Tübingen, 2019.

[21] W. Demtröder: *Atome, Moleküle und Festkörper*, volume 3 of *Experimentalphysik* (Springer, Berlin), 2005.

[22] J. Daintith: *A Dictionary of Chemistry*, Oxford Paperback Reference (OUP Oxford), 2008, URL `https://books.google.de/books?id=T6PuAAAAMAAJ`.

[23] H. H. Jaffe and A. L. Miller: The fates of electronic excitation energy, *Journal of Chemical Education*, volume 43, no. 9, 1966, 469.

[24] G. Baryshnikov, B. Minaev *et al.*: Theory and Calculation of the Phosphorescence Phenomenon, *Chemical Reviews*, volume 117, no. 9, 2017, 6500, URL `https://doi.org/10.1021/acs.chemrev.7b00060`, pMID: 28388041.

[25] AAT Bioquest Inc.: Spectrum [PPO], 2024, `https://www.aatbio.com/fluorescence-excitation-emission-spectrum-graph-viewer/ppo`.

[26] AAT Bioquest Inc.: Spectrum [Bis-MSB], 2024, `https://www.aatbio.com/fluorescence-excitation-emission-spectrum-graph-viewer/bis_msb`.

[27] T. Li, C. Zhou *et al.*: UV absorption spectra of polystyrene, *Polymer Bulletin*, volume 25, 1991, URL `https://doi.org/10.1007/BF00310794`.

[28] L. F. Nassier and M. H. Shinen: Study of the optical properties of poly-(methylmethacrylate) (PMMA) by using spin coating method, *Materials Today: Proceedings*, volume 60, 2022, 1660, URL `https://www.sciencedirect.com/science/article/pii/S2214785321079414`.

[29] S. H. So, K. K. Joo *et al.*: Development of a Liquid Scintillator Using Water for a Next Generation Neutrino Experiment, *Advances in High Energy Physics*, volume 2014, no. 1, 2014, 327184, URL `https://onlinelibrary.wiley.com/doi/abs/10.1155/2014/327184`.

[30] M. Yeh, S. Hans *et al.*: A new water-based liquid scintillator and potential applications, *Nuclear Instruments and Methods in Physics Research Section A: Accelerators, Spectrometers, Detectors and Associated Equipment*, volume 660, no. 1, 2011, URL `https://www.sciencedirect.com/science/article/pii/S0168900211016615`.

[31] F. Amat, P. Bizouard *et al.*: Measuring the Attenuation Length of Water in the CHIPS-M Water Cherenkov Detector, *Nuclear Instruments and Methods in Physics Research Section A: Accelerators, Spectrometers, Detectors and Associated Equipment*, volume 844, 10 2016, URL `https://doi.org/10.1016/j.nima.2016.11.032`.

[32] G. Yu, J. Zhang *et al.*: Analysis of Light Attenuation Length Measurement of a High Quality Linear Alkylbenzene for the JUNO Experiment, 2023, URL `https://arxiv.org/abs/2308.01949`.

[33] T. Adam, F. An *et al.*: JUNO Conceptual Design Report, 2015, URL `https://arxiv.org/abs/1508.07166`.

[34] Hamamatsu Photonics: *Photomultiplier Tube Handbook*, URL `https://www.hamamatsu.com/content/dam/hamamatsu-photonics/sites/documents/99_SALES_LIBRARY/etd/PMT_handbook_v4E.pdf`, visited 03.01.2025.

[35] Introduction to the Silicon Photomultiplier, visited 09.01.2024, `https://www.onsemi.com/download/application-notes/pdf/and9770-d.pdf`.

[36] Silicon Photomultipliers (SiPM), High PDE and Timing Resolution Sensors in a TSV Package, visited 09.01.2024, `https://www.onsemi.com/download/data-sheet/pdf/microj-series-d.pdf`.

[37] Incom: LAPPD, visited 07.02.2024, `https://incomusa.com/wp-content/uploads/LAPPD-Product-Sheet-08-19.pdf`.

[38] Incom: Measurement & Test Report LAPPD 64, visited 07.02.2024, ANNIE internal document: `https://annie-docdb.fnal.gov/cgi-bin/sso/ShowDocument?docid=4302`.

[39] G. R. Jocher, M. J. Wetstein *et al.*: Multiple-photon disambiguation on stripline-anode Micro-Channel Plates, *Nuclear Instruments and Methods in Physics Research Section A: Accelerators, Spectrometers, Detectors and Associated Equipment*, volume 822, 2016, 25, URL `https://www.sciencedirect.com/science/article/pii/S0168900216301127`.

[40] R. Acciarri, C. Adams *et al.*: Design and construction of the MicroBooNE detector, *Journal of Instrumentation*, volume 12, no. 02, February 2017, P02017–P02017, URL `http://dx.doi.org/10.1088/1748-0221/12/02/P02017`.

[41] MicroBooNE collaboration, P. Abratenko *et al.*: Inclusive cross section measurements in final states with and without protons for charged-current ν_μ-Ar scattering in MicroBooNE, 2024, URL `https://arxiv.org/abs/2402.19216`.

[42] Y. Fukuda *et al.*: The Super-Kamiokande detector, *Nucl. Instrum. Meth. A*, volume 501, 2003, URL `https://doi.org/10.1016/S0168-9002(03)00425-X`.

[43] L. Marti-Magro: SuperK-Gd: The Gd future of Super-Kamiokande., *PoS*, volume ICRC2019, 2020, URL `https://doi.org/10.22323/1.358.0957`.

[44] A. R. Back, J. F. Beacom *et al.*: Accelerator Neutrino Neutron Interaction Experiment (ANNIE): Preliminary Results and Physics Phase Proposal, 2017, URL `https://arxiv.org/abs/1707.08222`.

[45] M. Convery *et al.*: Fermilab Accelerator Complex: Status and Improvement Plans, `https://lss.fnal.gov/archive/test-tm/2000/fermilab-tm-2693-ad.pdf`.

[46] M. Convery: Fermilab's Accelerator Complex: Current Status, Upgrades and Outlook, *PoS, 10.22323/1.282.0047*, volume ICHEP2016, 2017, URL `https://doi.org/10.22323/1.282.0047`.

[47] D. G. Beechy and R. J. Ducar: Time and data distribution systems at the Fermilab accelerator, *Nuclear Instruments and Methods in Physics Research Section A: Accelerators, Spectrometers, Detectors and Associated Equipment*, volume 247, no. 1, 1986, 231, URL `https://www.sciencedirect.com/science/article/pii/0168900286905693`.

[48] FermiLab: TCLK Event Definitions 31-Aug-2021, `https://www-bd.fnal.gov/controls/hardware_vogel/tclk.htm`.

[49] A. A. Aguilar-Arevalo, C. E. Anderson *et al.*: Neutrino flux prediction at MiniBooNE, *Phys. Rev. D*, volume 79, Apr 2009, URL `https://link.aps.org/doi/10.1103/PhysRevD.79.072002`.

[50] M. R. Anderson, S. Andringa *et al.*: Measurement of neutron-proton capture in the SNO+ water phase, *Physical Review C*, volume 102, no. 1, Juli 2020, URL `http://dx.doi.org/10.1103/PhysRevC.102.014002`.

[51] G. H. Lee, Y. Chang *et al.*: *Ultrasmall Lanthanide Oxide Nanoparticles for Biomedical Imaging and Therapy* (Woodhead Publishing), 2014, URL `https://www.sciencedirect.com/science/article/pii/B9780081000663500140`.

[52] V. Fischer, J. He *et al.*: Development of an ion exchange resin for gadolinium-loaded water, *Journal of Instrumentation*, volume 15, no. 07, Juli 2020, P07004–P07004, URL `http://dx.doi.org/10.1088/1748-0221/15/07/P07004`.

[53] M. Ascencio-Sosa, Z. Bagdasarian *et al.*: Deployment of Water-based Liquid Scintillator in the Accelerator Neutrino Neutron Interaction Experiment, *Journal of Instrumentation*, volume 19, no. 05, may 2024, P05070, URL `https://dx.doi.org/10.1088/1748-0221/19/05/P05070`.

[54] T. Kaptanoglu, E. J. Callaghan *et al.*: Cherenkov and scintillation separation in water-based liquid scintillator using an LAPPD, *The European Physical Journal C*, volume 82, no. 169, February 2022, URL `https://doi.org/10.1140/epjc/s10052-022-10087-5`.

[55] B. Richards: ToolDAQ Framework v2.1.1, November 2018, URL `https://doi.org/10.5281/zenodo.1482767`.

[56] Boost Software Library, `https://www.boost.org/users/history/version_1_66_0.html`.

[57] ZeroMQ Software Library, `https://zeromq.org/`.

[58] B. Richards: Software Summary, visited 07.02.2024, ANNIE internal document: `https://annie-docdb.fnal.gov/cgi-bin/sso/ShowDocument?docid=4289`.

[59] E. Drakopoulou: ANNIE Phase II Reconstruction Techniques, 2018, URL `https://arxiv.org/abs/1803.10624`.

[60] E. Oberla, J.-F. Genat *et al.*: A 15GSa/s, 1.5GHz bandwidth waveform digitizing ASIC, *Nuclear Instruments and Methods in Physics Research Section A: Accelerators, Spectrometers, Detectors and Associated Equipment*, volume 735, 2014, 452, URL `https://www.sciencedirect.com/science/article/pii/S016890021301276X`.

[61] Yocto Project Maxi Thermistor, visited 06.12.2022, `https://www.yoctopuce.com/EN/products/usb-environmental-sensors/yocto-maxithermistor`.

[62] PILAS DX Picosecond pulsed diode lasers, visited 06.07.2022, `https://www.nktphotonics.com/lasers-fibers/product/pilas-picosecond-pulsed-diode-lasers/pilas.html`.

[63] E. Angelico: Development of Large-Area MCP-PMT Photo-Detectors for a Precision Time-of-Flight System at the Fermilab Test Beam Facility, 06 2020.

[64] I2C Communication with the Honeywell HumidIcon Digital Humidity/Temperature Sensors, visited 17.07.2020, `https://prod-edam.honeywell.com/content/dam/honeywell-edam/sps/siot/en-us/products/sensors/humidity-with-temperature-sensors/common/documents/sps-siot-i2c-comms-humidicon-tn-009061-2-en-ciid-142171.pdf`.

[65] A. Collaboration: Internal ANNIE Communication.

[66] L. U. A. Rivera: OtS Ethernet Interface, User Manual, visited 05.06.2023, ANNIE internal document.

[67] A. Back, J. Beacom *et al.*: Measurement of beam-correlated background neutrons from the Fermilab Booster Neutrino Beam in ANNIE Phase-I, *Journal of Instrumentation*, volume 15, no. 03, March 2020, URL `https://dx.doi.org/10.1088/1748-0221/15/03/P03011`.

[68] F. Kohler: Simulation, Design and Testing of SiPM Arrays with Light Guides, Master's thesis, Eberhard Karls Universität Tübingen, 2022.

[69] S. Agostinelli, J. Allison *et al.*: Geant4—A simulation toolkit, *Nuclear Instruments and Methods in Physics Research Section A: Accelerators, Spectrometers, Detectors and Associated Equipment*, volume 506, no. 3, 2003, 250, URL `https://www.sciencedirect.com/science/article/pii/S0168900203013688`.

[70] Eljen EJ-510 Reflective Paint, visited 11.09.2021, `https://eljentechnology.com/products/accessories/ej-510`.

[71] CAEN-V895 Manual, visited 09.05.2024, `https://www.caen.it/?downloadfile=9026`.

[72] CAEN-V830 manual, visited 09.05.2024, `https://www.caen.it/?downloadfile=9202`.

[73] Alubox Riffelblech alukiste 250 Liter, visited 11.09.2021, `https://www.alubox.eu/Strong/`.

[74] Hamamatsu: Photomultiplier Tubes, 1998, `https://docs.ampnuts.ru/others_docs/Hamamatsu/Hamamatsu-PMT.pdf`.

[75] Philips: XP2020 - 12 stage photomultiplier tube, 1989, `https://wwwusers.ts.infn.it/~rui/univ/Acquisizione_Dati/Manuals/Philips%20XP2020.pdf`.

[76] CAEN-V1742 manual, visited 09.05.2024, `https://www.caen.it/?downloadfile=6020`.

[77] VL420-5-15 Technical Report UV LED, visited 20.06.2018, `https://www.roithner-laser.com/datasheets/led_div/vl420-5-15.pdf`.

[78] G. Grünauer: Further development of the CELLPALS method for measuring the attenuation length and the group velocity in very transparent liquids, Master's thesis, Eberhard Karls Universität Tübingen, 2022.

[79] P. Sjölin: The scintillation decay of some commercial organic scintillators, *Nuclear Instruments and Methods*, volume 37, 1965, 45, URL `https://www.sciencedirect.com/science/article/pii/0029554X65903356`.

[80] L. Martinazzoli, N. Kratochwil *et al.*: Scintillation properties and timing performance of state-of-the-art Gd3Al2Ga3o12 single crystals, *Nuclear Instruments and Methods in Physics Research Section A: Accelerators, Spectrometers, Detectors and Associated Equipment*, volume 1000, 2021, 165231, URL `https://www.sciencedirect.com/science/article/pii/S0168900221002151`.

[81] S. Corrigan: Introduction to the Controller Area Network (CAN), Technical Report SLOA101B, Texas Instruments, August 2002, URL `https://www.ti.com/lit/an/sloa101b/sloa101b.pdf`, revised May 2016.

Acronyms

1p-1h 1-particle 1-hole. 8

2p-2h 2-particle 2-hole. 8, 28

ACC ANNIE Central Card. 36, 49, 50, 52, 53, 57, 59–61, 95, 125

ACDC ACquisition and Digitization with PseC4. 34–36, 42, 49, 50, 52, 53, 55–57, 59, 63, 95, 125, 127

ADC Analog-Digital-Converter. 34, 39, 40, 43, 55, 73, 77, 84, 96, 126, 129

AGN Active Galactic Nuclei. 6

ALC Active Light Collector. 65, 67, 68, 84, 86, 93, 94, 96, 128, 131

ANNIE Accelerator Neutrino Neutron Interaction Experiment. 1, 3, 7, 8, 23–31, 33, 42, 44, 47, 50, 52, 53, 55, 57, 61, 63, 95, 96, 123–125

AOP Anode Output Pulse. 71

APD Avalanche Photodiode. 15, 16, 19, 20, 124

ASIC Application-Specific-Integrated-Circuit. 34, 49, 52

B.O.B. Break-Out-Box. 36, 125

bis-MSB 1,4-Bis(2-methylstyryl)benzol. 13, 14, 67, 68, 81, 83, 84, 86–88, 91, 93, 94, 96, 123, 128, 130, 131, 133, 134

BNB Booster-Neutrino-Beam. 1, 23–26, 28, 49, 52, 55, 58–61, 63, 95, 124, 127, 133

CanBus Controller Area Network Bus. 34–37, 42–44, 99, 125, 131, 134

CC charged current. 6–8, 23, 25, 28, 125

CC-DIS Charged Current Deep Inelastic Scattering. 7, 8, 123

CC-RES Charged Current Resonance. 7–9, 28, 123

CCQE Charge Current Quasi Elastic. 7–9, 28, 123

CE collection efficiency. 18, 20

CMB Cosmic Microwave Background. 3, 5

CTC Central Trigger Card. 57

DAC Digital-Analog-Converter. 43

DAQ Data Acquisition. 30, 31, 34, 36, 37, 42, 49–54, 57, 77, 84, 125, 126, 129

DCR Dark-Count-Rate. 17, 72–75, 82, 84, 96, 129

DSNB Diffuse Supernova Neutrino Background. 5

DUNE Deep Underground Neutrino Experiment. 7, 123

FACC Front Anti-Coincidence Counter. 25, 26, 124

Fermilab Fermi National Accelerator Laboratory. 1, 23, 24, 54, 59, 124

FMV Front Muon Veto. 25, 28, 125

FOP Fast Output Pulse. 71

FPGA Field-Programmable-Gate-Array. 34, 49

FSI final state interaction. 8, 9, 123

Geant4 Geometry and Tracking 4. 67, 68, 128

GPS Global Positioning System. 49, 52

HPLC High-Purity-Low-Conductivity. 1, 75, 78, 81, 83, 84, 96, 130

HV high voltage. 34, 36, 37, 42–44, 46–48, 54, 55, 75, 77, 126, 127, 129

Hyper-K Hyper Kamiokande. 7, 123

I2C Inter-Integrated Circuit. 43

IBD Inverse Beta Decay. 5, 6

IC internal conversion. 12, 13

Iowa State Iowa State University. 37, 54, 59

ISC inter-system crossing. 12, 13

JGU Johannes Gutenberg University. 69

JUNO Jiangmen Underground Neutrino Observatory. 14

LAB Linear Alkyl Benzene. 1, 14, 15, 81, 83–88, 91, 93, 94, 96, 130, 131, 133, 134

LAPPD Large Area Picosecond Photodetector. 1, 2, 19–21, 25–27, 30, 31, 33–37, 39–42, 44, 46–50, 52–55, 57–61, 63–65, 95, 96, 101, 107, 124–128, 131, 133, 134

LC light collector. ii, 65–94, 128, 130, 131, 133, 134

LED Light Emitting Diode. 27, 77–79, 129

LV low voltage. 34, 36, 37, 42, 43, 47, 48, 54, 55, 126, 127

LVHV Low-Voltage-High-Voltage. 34, 35, 37, 42–44, 46, 48, 49, 55, 125, 126

MCP Micro-Channel-Plate. 16, 17, 20, 21, 124

MRD Muon Range Detector. 25, 26, 28, 30, 31, 58, 124, 125

NC neutral current. 6, 23

NIM Nuclear Instrumentation Modul. 36

NOvA NuMI Off-axis ν_e Appearance. 7, 123

ONSEMI ONSEMI J-Series. 70–72, 133

PCB Printed Circuit Board. 69–71, 73, 79, 85, 111, 129, 131, 132

PD Photodiode. 15, 16, 124

PDE photo detection efficiency. 18, 20, 67, 72

PLC Passive Light Collector. 65, 67, 68, 84–86, 93, 94, 96, 110, 128, 131

PMMA Polymethylmethacrylat. 14, 65

PMT Photomultiplier tube. 16–18, 20, 25, 26, 28, 30, 31, 33, 58, 71, 72, 75–77, 84, 96, 124, 125, 129

POT proton-on-target. 23

PPO 2,5-Diphenyloxazole. 13, 14, 67, 68, 81, 83, 84, 86–88, 91, 93, 96, 123, 128, 130, 131, 133, 134

PPS Pulse per Second. 49, 50, 52, 54, 57–63, 102, 127, 133, 134

PS Polystyrol. 14, 15, 65, 67, 68, 128

QE quantum efficiency. 18, 20, 21, 37

R&D Research and Development. 1, 26, 33, 95

RF radio frequency. 74

RPi Raspberry Pi. 30, 34, 36, 37, 42–44, 48–50, 52, 53, 70, 71, 77, 111, 125, 129, 131

s.pe. single photoelectron. 38, 39, 41, 71, 73, 78, 84, 126

SANDI Scintillator for ANNIE Neutrino Detection Improvement. 25–27, 124

SC Slow Control. 34, 36, 42–50, 54, 126, 133

SCA Switched Capacitor Array. 56

SiLC SiPM with Light Collector. 65–67, 69, 81, 86, 94, 96, 128

SiPM Silicon Photomultiplier. 1, 13, 19, 20, 65–94, 96, 97, 109–111, 121, 124, 128–134

SMA SubMiniature version A. 34, 69

SPI Serial Peripheral Interface. 43

TB Triggerboard. 34, 35, 37, 42, 43, 49, 125

TCKL Tevatron Clock. 24

TDC time-to-digital converter. 30

TTS transit-time-spread. 17, 18, 38–40, 78–80, 84, 126, 129, 130, 133

TUM Technische Universität München. 81

UART Universal Asynchronous Receiver Transmitter. 49

UC Davis University of California Davis. 37, 42, 54, 59

USB Universal Serial Bus. 36, 37, 42, 44, 50, 52, 53, 95, 125

UWH Underwater Housing. 34, 36, 37, 40, 42, 43, 46–49, 54, 55, 125, 127, 133

VCDL Voltage Controlled Delay Line. 56

VME Versa Module Eurocard. 30, 31, 73, 75, 77, 125, 129

VR vibrational relaxation. 12, 13

WbLS Water-based-Liquid-Scintillator. 1, 14, 15, 25, 27, 67, 81, 83–86, 89, 90, 92, 94, 96, 123, 130, 131, 133, 134

WLS Wavelength Shifter. 13–15, 65, 67, 93

YOCTO Yoctopuce Maxi Thermistor. 36, 37, 42–44, 125

ZMQ ZeroMQ. 30

List of Figures

List of Tables

Danksagung/Acknowledgements

An dieser Stelle möchte ich all den Menschen danken, die mich auf meinem Weg zur Fertigstellung dieser Dissertation begleitet und unterstützt haben.

Mein besonderer Dank gilt Prof. Dr. Tobias Lachenmaier für die Möglichkeit diese Arbeit machen zu dürfen, seine kompetente fachliche Betreuung, die anregenden Diskussionen und das mir entgegengebrachte Vertrauen. Über die Jahre konnte ich viel von seiner wissenschaftlichen Erfahrung lernen.

Ebenso geht mein Dank and die gesamte Arbeitsgruppe, sowohl privat während dem Mittagessen im Glaskasten, Weihnachtsfeiern und anderen Veranstaltungen, oder im Rahmen von wissenschaftlichen Diskussionen. Besonders gilt mein Dank dabei meinem Zweitbetreuer Prof. Dr. Josef Jochum und Gaby Behring, ohne welche diese Arbeit nicht möglich gewesen wäre. Auch gilt mein Dank Dr. Günter Lang und Gabriele Enßlin-Richter für die Hilfe bei Organisatorischen Problemen.

Ein besonderer Dank gebührt meinen Bürokollegen, Dr. Tobias Heinz und Dr. Tobias Sterr (welche ich jetzt hier schon Dr. nennen muss), so wie Dr. Katja Wurster. Auch den anderen "Gentlemen", Gina Grünauer, Jessica Eck, Katharina Kilgus, Lukas Wolz, Colin Heckmeyer sowie Dr. Ann-Kathrin Schütz und Dr. Lukas Rauscher gilt mein Dank. Der Ausgleich im privaten wäre ohne euch nicht möglich gewesen. Seien es unsere Ausflüge, spontanes Grillen oder das gelegentlich abendliche zocken, ohne diese wäre die Zeit sehr trostlos geworden.

A big thanks also goes to the ANNIE collaboration which gave me the opportunity to work on this exciting project. A special thanks goes to Prof. Matthew Wetstein, Prof. Amanda Weinstein, Dr. Benjamin Richards as well as Dr. Marvin Ascensio-Sosa, Dr. Julie He, Dr. Paul Hackspacher. Be it interesting discussions, late night deployment sessions, software discussions or on-site support their input was always highly valued.

Ein weiterer Dank geht noch an Prof. Dr. Michael Wurm für seine Bereitschaft mich zu prüfen und seine Unterstützung sowohl in Sachen ANNIE als auch der Entstehung der SiLC-Module, an Dr. Hans Steiger und Patrick Deucher für die Bereitstellung von flüssig/Plastik Szintillatoren und zu guter Letzt Norbert Stockmaier und seine Werkstatt Crew, welche mir immer spontan bei der Bearbeitung der Szintillatoren zur Seite standen.

Zuletzt möchte ich mich noch bei meiner Familie bedanken, ohne welche ich nicht einmal in der Lage gewesen wäre bis zu Promotion zu kommen. Für die ganze Hilfe, Rat und Tat, Unterstützung und Aufmunterungen von ganzem Herzen Danke.